Copyright Undertaking

This thesis is protected by copyright, with all rights reserved.

By reading and using the thesis, the reader understands and agrees to the following terms:

1. The reader will abide by the rules and legal ordinances governing copyright regarding the use of the thesis.
2. The reader will use the thesis for the purpose of research or private study only and not for distribution or further reproduction or any other purpose.
3. The reader agrees to indemnify and hold the University harmless from and against any loss, damage, cost, liability or expenses arising from copyright infringement or unauthorized usage.

If you have reasons to believe that any materials in this thesis are deemed not suitable to be distributed in this form, or a copyright owner having difficulty with the material being included in our database, please contact lbsys@polyu.edu.hk providing details. The Library will look into your claim and consider taking remedial action upon receipt of the written requests.

Pao Yue-kong Library, The Hong Kong Polytechnic University, Hung Hom, Kowloon, Hong Kong

http://www.lib.polyu.edu.hk

MECHANICAL PROPERTIES OF DUAL ION BEAM DEPOSITED SILICON NITRIDE FILMS

TSANG MEI-PO MABLE

M. PHIL.

THE HONG KONG POLYTECHNIC UNIVERSITY

2001

Pao Yue-Kong Library
PolyU • Hong Kong

Abstract

Amorphous silicon nitride (SiN_x) films with nitrogen-to-silicon ratio (x) varying from 0 – 1.36 were fabricated by dual ion beam deposition (DIBD) on Si substrates. The composition, structure and many physical properties (i.e. mechanical, etching, optical and electrical properties) of the films were characterized.

The hardness and elastic modulus of the hydrogen-free DIBD SiN_x films were found to vary from 12.2 – 21.5 GPa and 191 – 256 GPa respectively with increasing x. The friction coefficient dropped from 0.58 to 0.38. Owing to peening effect, all the films had compressive stress, which rose from 0.53 to 1.41 GPa with x. These data revealed that DIBD SiN_x could be used for surface protective coatings.

The etching rate of the $SiN_{1.36}$ film in buffered hydrofluoric acid (BHF) was above 7 nm min^{-1}. For KOH at 80 °C, the etching rate of all the samples was negligibly small. A model was established to fit the optical absorption spectra and temperature dependence of electrical conductivity of the films with high density of mid-gap states. Results indicated that the optical band gap of DIBD SiN_x films rose from 1.8 to 4.2 eV when x increased. Hopping of charge carriers dominated the transport properties of the films.

Nanoindentation tests were done on microbridges made of CVD silicon nitride films. The load-unload curves of CVD microbridges were fitted numerically, and the elastic modulus, residual stress and bending strength of the films were derived. This experiment demonstrated the validity of this methodology.

Acknowledgements

I would like to acknowledge Dr. C. W. Ong, my chief supervisor, for his invaluable advice and his close supervision in my study period. I also gratefully acknowledge for his suggestions editing content and organization of this thesis.

I am especially indebted to Dr. K. F. Chan and Dr. N. Chong for the fruitful discussions with them and their enlightening suggestions on my research work.

I would like to thank Dr. P. K. Lim of the Hong Kong Baptist University for his assist in performing the XPS analysis, and Mr. W. W. Hung for his assist in carrying out part of XPS analysis.

Moreover, I would like to thank Mr. C. W. Lip and Ms. S. W. Ng of the Department of Electronic and Information Engineering of the Microelectronics Laboratory for their assist in operating the reactive ion etch machine.

Thanks are also due to Mr. K. H. Ho of the machine shop of the Department of Applied Physics for machining parts for our set-up. Mr. M. N. Yeung of Materials Research Center for his assist in operating the scanning electron microscope, and also thanks to the staff of our department for technical support.

Finally, I would like to extent my special thanks to Ms. W. M. Fung, Mr. K.W. Tang, Mr. S. F. Wong, Mr. Y. L. Ip, Mr. Y. K. Ho and Ms. F. S. Tang for their assistant in experimental and technical supports.

This study was financially supported by the Center for Smart Materials of The Hong Kong Polytechnic University and the internal grants from The Hong Kong Polytechnic University under Code Nos. G-V 845.

Acronyms

BHF	Buffered hydrofluoric acid
CVD	Chemical vapor deposition
DIBD	Dual ion beam deposition
DOS	Density of electron state
FTIR	Fourier transform infrared
HF	Hydrofluoric acid
IBD	Ion beam deposition
KOH	Potassium hydroxide
LPCVD	Low pressure chemical vapor deposition
MEMS	Microelectromechanical system
PECVD	Plasma-enhanced chemical vapor deposition
RF	Radio frequency
RMS	Reactive magnetron sputtering
SEM	Scanning electron microscope
XPS	X-ray photoelectron spectroscopy
XRD	X-ray diffraction

Table of contents

Abstract i

Acknowledgments ii

Acronyms iv

Table of contents v

List of figures viii

List of tables xi

Chapter 1 Introduction 1-1

1.1 General background 1-1

1.2 Scope of this study 1-6

Chapter 2 Sample preparation 2-1

2.1 Dual ion beam deposition system 2-1

2.2 Deposition processes and conditions 2-4

2.3 Micromachining 2-5

2.3.1 General description of isotropic and anisotropic etching techniques 2-5

2.3.2 Isotropic etching 2-6

2.3.3 Anisotropic etching 2-7

Chapter 3 Sample characterization 3-1

3.1 Composition and structural analyses 3-1

3.1.1 Thickness measurements 3-1

3.1.2 X-ray photoelectron spectroscopy 3-3

3.1.3 Fourier transform infrared absorption spectroscopy 3-4

3.1.4 X-ray diffraction 3-6

3.2 Mechanical properties 3-8

3.2.1 Hardness and elastic modulus measurements 3-8

3.2.3 Tribological tests 3-13

3.2.4 Stress analyses 3-13

3.3 Optical absorption 3-16

3.4 Electrical conductivity measurements 3-18

Chapter 4 Composition and structure 4-1

4.1 Thickness and coating rate 4-1

4.2 Composition determined by X-ray photoelectron spectroscopy 4-5

4.3 Chemical structure analyzed by X-ray photoelectron spectroscopy 4-11

4.4 Fourier transform infrared absorption 4-18

4.5 X-ray diffraction analyses 4-21

Chapter 5 Mechanical properties 5-1

5.1 Nanoindentation experiments 5-1

5.2 Friction coefficient measurement 5-4

5.3 Stress measurement 5-7

Chapter 6 Etching properties 6-1

6.1 Wet etch 6-1

6.2 Dry etch 6-4

Chapter 7 Optical and electrical properties 7-1

7.1 Analysis of optical absorption and determination of DOS 7-1

7.2 Analysis of electrical conductivity and transport mechanisms 7-10

Chapter 8 Conclusions 8-1

Appendix Test on silicon nitride microbridges A-1

References R-1

List of publications P-1

List of figures

Page

Fig. 1.1 The crystalline structure of Si_3N_4. 1-2

Fig. 2.1(a) Schematic diagram of the pumping system of the dual ion beam deposition (DIBD) system. 2-2

Fig. 2.1(b) Schematic diagram of the setting inside the chamber of the DIBD system. 2-2

Fig. 3.1 The principle of film thickness measurement by using an α-step surface profile. 3-2

Fig. 3.2 The basic configuration of an FTIR spectrometer. 3-5

Fig. 3.3 Schematic presentation of the principle of X-ray diffraction. Path difference between the two incident rays = AB + BC. 3-7

Fig. 3.4 A typical pattern of load-unload curve of a nanoindentation. 3-12

Fig. 3.6 The principle of the measurement of the radius of curvature of a film-on-substrate configuration. 3-16

Fig. 3.7 The set-up for electrical conductivity measurement. 3-20

Fig. 4.1 Coating rate of DIBD SiN_x films on 525 μm thick Si, 75 μm thick Si and fused quartz substrates. 4-3

Fig. 4.2 Relative content of Si, N, O and C as a function of assist N_2^+ beam current. 4-7

Fig. 4.3 N-to-Si ratio (x) as a function of assist N_2^+ beam current. 4-9

Fig. 4.4 C 1s photoelectron spectra of DIBD SiN_x films with different value of x, recorded after surface cleaning. 4-14

Fig. 4.5 Si 2p photoelectron spectra of DIBD SiN_x films with different value of x, recorded after surface cleaning. 4-15

Fig. 4.6 N 1s photoelectron spectra of DIBD SiN_x films with different value of x, recorded after surface cleaning. 4-17

Fig. 4.7 IR absorption spectra of the DIBD SiN_x films showing the formation of Si-N bonds (850 cm^{-1}). No hydrogen and oxygen related bonds are detected. 4-20

Fig. 4.8 XRD spectra of the DIBD SiN_x films with $x = 1.34$ and $x = 0$. 4-23

Fig. 5.1 Hardness (H) and elastic modulus (E_m) of DIBD SiN_x films as functions of x. 5-2

Fig. 5.2 Experimental data of friction coefficient (μ) with various x values against scratching distance. 5-5

Fig. 5.3 Friction coefficient (μ) of DIBD SiN_x films as functions of x. 5-6

Fig. 5.4 Internal stress (σ_s) of DIBD SiN_x films with various N-to-Si ratios (x). Inset: SEM micrograph of the hangover of a $SiN_{1.34}$ sample on Si substrate. 5-8

Fig. 5.5 Comparison of internal stresses measured in silicon nitride films prepared by different techniques. 5-11

Fig. 6.1 Etching rate of the DIBD SiN_x films in BHF and KOH solutions as a function of x. 6-3

Fig. 7.1 Optical absorption spectra of DIBD SiN_x films with various x. Fitting curves derived from the theory described in the text are shown. 7-2

Fig. 7.2 DOS model used for analyzing the optical absorption spectra of the SiN_x films. 7-4

Fig. 7.3 Temperature dependence of electrical conductivity (σ_c) of the DIBD SiN_x films with various x. Fitting curves derived from the theory described in the text are shown. 7-11

Fig. 7.4 Plots of theoretically derived drift mobility of charge carriers at E_f against the reciprocal of temperature. 7-18

Fig. 7.5 Plots of theoretically derived drift mobility of charge carriers at 300K against energy from the Fermi level ($E - E_f$). 7-19

Fig. A.1 Flow chart for microbridge fabrication. A-3

Fig. A.2 Load-displacement test on a microbridge sample. A-5

Fig. A.3 Micrograph of LPCVD silicon nitride microbridges for samples of S1 and S2 (100X). A-7

Fig. A.4 The load-unload curve of the LPCVD silicon nitride microbridge S1 before fracture occurs. Thickness $t_b = 0.4$ μm, width $b_w = 20$ μm and length $l_b = 480$ μm. A-8

Fig. A.5 Load-displacement curve of microbridge S2 recorded until fracture occurs. Thickness $t_b = 0.4$ μm, width $b_w = 20$ μm and length $l_b = 460$ μm. A-9

Fig. A.6 Simply supported ends boundary conditions. A-10

Fig. A.7 Comparison of experimental and theoretical load-displacement curves of microbridge. Square points: experimental data, solid line: theoretical solution. A-12

Fig. A.8 Theoretical analysis of load-displacement curve of sample S2. Square points: experimental data, solid line: theoretical solution. A-15

List of tables

		Page
Table 2.1	A summary of the preparation conditions of the DIBD SiN_x films.	2-4
Table 3.1	*d* spacings of some major lattice planes of Si and Si_3N_4 in XRD experiment.	3-6
Table 3.2	The setting of maximum loads assigned in the six nanoindentation experiments.	3-10
Table 4.1	Thickness, coating rate and substrate temperature of the DIBD SiN_x film samples deposited on different substrates and at different assist N_2^+ ion beam currents.	4-2
Table 4.2	N-to-Si ratio (x) of DIBD SiN_x films deposited at different assist N_2^+ ion beam currents.	4-10
Table 4.3	Summary of XPS data obtained after surface cleaning.	4-12
Table 5.1	The hardness (H) and elastic modulus (E_m) of DIBD SiN_x films with various N-to-Si ratio (x) values.	5-3
Table 7.1	Nine possible electron transitions associated with absorption of photons, and the corresponding integration limits in Eq. (7.1.5).	7-6
Table 7.2	Summary of the values of A, E_{opt}, ε_o and E_o assigned to the DOS functions for getting good fits to the optical absorption spectra of SiN_x films with various N contents. I_a is the assist N_2^+ ion beam current used for bombarding the substrate.	7-9
Table 7.3	Summary of the values of E_a, $1/\rho(E_f)$ and δ in Eq. (7.2.4) for good fits to the optical absorption spectra of SiN_x films with various N contents. The calculated hopping distances R at Fermi level E_f and E_v (or E_c) are given.	7-15
Table A.1	Etchants for removing Si wafer, Si_3N_4, SiO_2, Au and Cr layers.	A-4
Table A.2	Dimensions of the LPCVD silicon nitride microbridge samples.	A-6

Chapter 1
Introduction

1.1 General background

Silicon nitride is well known to be a material possessing a number of distinctive properties. First, silicon nitride in crystalline form has a stoichiometric composition of Si_3N_4 and is crystallized with hexagonal atomic planes with a structure as shown in Fig. 1.1 [Pierson 1996]. The atomic plane is a basic unit for constructing different polymorphs such as α-Si_3N_4 and β-Si_3N_4. In this atomic plane, a and a′ have lengths of 0.275 and 0.179 nm, respectively. It consists of hexagonal rings, each containing four silicon and four nitrogen atoms. α-Si_3N_4 and β-Si_3N_4 are built according to different stacking order of lattice planes. In the α form, the AB stacking is followed by its mirror image to give an arrangement of ABBA/ABBA/... etc.. The β form has an ABAB stacking order. All these structures are formed by strong covalent bonds. -

Besides the α and β structures, silicon nitride can also exist in amorphous form. The N-to-Si ratio can be varied in a rather broad range according to the fabrication conditions. The chemical bonds in silicon nitride are so strong, such that the melting point is extremely high (refractory). Due to the same reason, the hardness of silicon nitride is high too, typically in the order of 20 GPa. As a consequence, it is supposed to be a useful hard coating material [Ron *et al.* 1983]. Moreover, silicon nitride has been found to have internal stress, the magnitude of which is highly

dependent on the fabrication techniques and conditions employed. The internal stress of silicon nitride in thin film form can be varied from being compressive to tensile or vice versa according to the preparation conditions [Kanicki 1988 and Blaauw 1983].

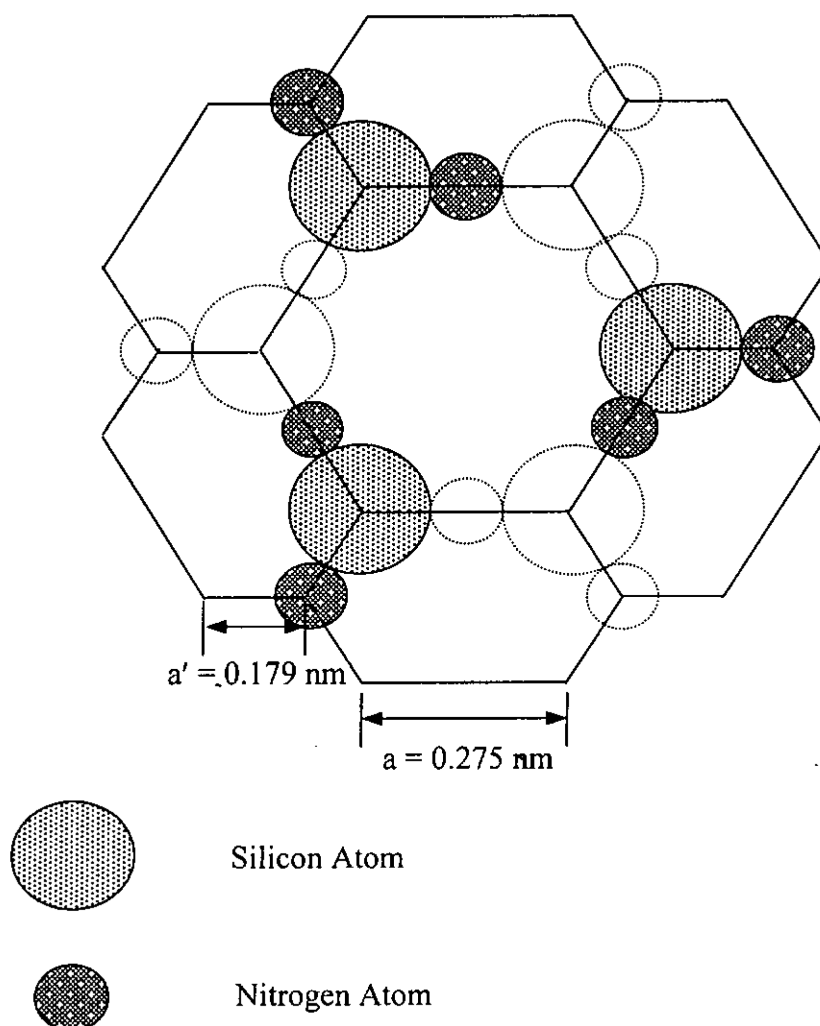

Fig. 1.1 The crystalline structure of Si_3N_4.

Silicon nitride also has an excellent chemical inertness, such that it can resist attacks of alkalis and acids. Because of the excellent mechanical and chemical properties, silicon nitride is recently being proposed to be an important material in the applications of microelectromechanical devices (MEMS) and sensors [Reynes and Bruyere 1992]. In addition, silicon nitride films deposited by CVD techniques have a large optical band gap (5 eV) [Gupta *et al.* 1988] and a very high dielectric strength (5.5) [Elshabini-Riad and Barlow 1997]. They have already been widely used in microelectonic devices, very large scale integrated circuits, thin film transistors, and solar cells [Belyi 1988]. In recent years, silicon nitride has been used in bulk micromachining as its mechanical strength allows fabrication of large membranes. It is also used as mask for selective oxidation, gate dielectrics and insulator. It is a good insulator and barrier against alkali metal contamination, and is applied as a good passivation material for finished devices and also for surface encapsulation during ion implantation [Yang 1988].

The studies on the properties of silicon nitride have already had a long and rich history. Silicon nitride is not a natural material, but can be synthesized by a variety of methods. Conventionally, silicon nitride films in industrial applications are obtained mainly by chemical vapor deposition (CVD) [Balland *et al.* 1993], plasma-enhanced chemical vapor deposition (PECVD) [Savall *et al.* 1995 and Gupta *et al.* 1991] and low-pressure chemical vapor deposition (LPCVD) [Arnoldbik *et al.* 1993]. Silicon nitride fabricated by physical vapor deposition techniques, such as reactive ion beam deposition (IBD) [Erler *et al.* 1980] and dual ion beam deposition (DIBD)

[Weissmantel 1976] etc., are restricted to be under research investigations, but seldom to be applied for production.

Today, high quality stoichiometric silicon nitride (Si_3N_4) films are fabricated by thermal CVD at high temperatures exceeding 700°C. However, one drawback of CVD techniques is that they involve very often the use of toxic and explosive reactant gases, which are hazardous and inhibit the technique from being widely used, especially in educational institutions.

Moreover, silicon nitride film could contain high internal stress depending on the fabrication conditions. Under the influence of strong internal stress, SiN_x film could peel off from the substrate or develop detrimental cracks. This hinders SiN_x to be useful in a number of applications.

Silicon nitride films deposited at temperature below 450 °C by PECVD often result in considerably high hydrogen content (10-30 at.%). The high hydrogen inclusion could lead to rapid oxidation in air, or fast etching rate by some chemicals [Parsons *et al.* 1991 and Ray *et al.* 1994]. For example, the increase in hydrogen content could raise the etching rate of plasma enhanced CVD silicon nitride in buffered hydrofluoric (BHF) by two orders of magnitude [Jansen *et al.* 1992].

Therefore, studies on developing other physical vapor deposition (PVD) methods for fabricating silicon nitride are needed. Physical vapor deposition, such as magnetron sputtering and ion beam deposition are particularly interesting because

they are clean and safe. The former has widely been used in industries for fabricating dielectrics or metallization, while the latter is an extremely versatile research tool for synthesizing new materials [Erler *et al.* 1980]. With these methods, hydrogen-free silicon nitride can be fabricated. The problems associated with inclusion of hydrogen could be eliminated. It is also an important topic to investigate how the internal stress in PVD silicon nitride films could be controlled by varying the deposition conditions.

1.2 Scope of this study

The purposes of this study are to fabricate silicon nitride by dual ion beam deposition (DIBD) method and to investigate the properties of the film samples. First, for a DIBD process, an ion gun is used to sputter Si, while the other ion gun is used to inject nitrogen into the deposits. DIBD is powerful in controlling the incorporation level of N, such that the changes of the properties of the films as functions of the N-to-Si ratio can be revealed. In practice, the assist N_2^+ ion beam current was adjusted from zero to 45 mA, such that the current density of the N_2^+ ion beam bombarding the substrate is increased.

Second, the composition and structure of the DIBD SiN_x films were characterized by X-ray photoelectron spectroscopy (XPS), Fourier transform infrared absorption (FTIR) and X-ray diffraction (XRD). They were then correlated with the assist nitrogen ion beam current.

For investigations on the mechanical properties, hardness and elastic modulus of the films were evaluated by nanoindentation techniques. Friction coefficient and internal stress of the films were also determined. Hardness of thin films has already been extensively adopted as an important indicator for the quality of the material and processing in industries. Elastic modulus and internal stress are important. They should be explored and correlated with the variation in crystallinity of the films. Moreover, internal stress is an important parameter that prescribes the mechanical failure, such as cracking of thin films [Tsukamoto 1987].

The chemical resistance of the film samples against buffered hydrofluoric (BHF) and potassium hydroxide (KOH) was also investigated. The results are useful for evaluating the applicability of SiN_x in MEMS applications. They can also help designing appropriate microfabrication processes via chemical etching.

The optical absorption spectra of the films were examined by UV-VIS-NIR double beam spectrophotometry. The temperature dependence of electrical conductivity of the SiN_x samples was measured. Data of optical absorption were deconvoluted to build up models of density of state (DOS), which were then used to explain the results of electrical conductivity measurements and to reveal the transport properties of the films.

Finally, a series of microbridges of LPCVD silicon nitride with different dimensions were fabricated by conventional photolithography technique for nanoindentation experiment. This is a recently developed method for evaluating the internal stress, elastic modulus and bending strength of thin film materials by analyzing the load-displacement behaviour. However, since the DIBD silicon nitride film samples were found to have compressive stress and so were not suitable to be used in this experiment, therefore, LPCVD silicon nitride was used instead. By numerical fitting to the data, the elastic modulus and internal stress of the films were extracted. Our results have illustrated the effectiveness and usefulness of such a technique. Its application to mechanical property characterization of thin films is fully justified.

Chapter 2
Sample preparation

Hydrogen free silicon nitride (SiN_x) films were prepared by dual ion beam deposition (DIBD). The deposition system and its operation are described in first two sections of this chapter. The deposition method and conditions for preparing SiN_x thin films are given. The last section is an introduction of micromachining techniques.

2.1 Dual ion beam deposition system

A schematic diagram of the dual-ion-beam deposition system used for preparing SiN_x film is illustrated in Fig. 2.1(a) and Fig. 2.1(b). The vacuum chamber is connected to a turbomolecular pump (KYKY FB1500, 1500 ls^{-1}) and is backed by an Edwards M2E40 oil rotary pump (10 ls^{-1}). The pressure in the chamber is detected by a capacitive pressure transducer (MKS 122A Baratron gauge) in the pressure range higher than 1 mTorr, and by a cold cathode pressure gauge (HPS 941) in the range below 1 mTorr.

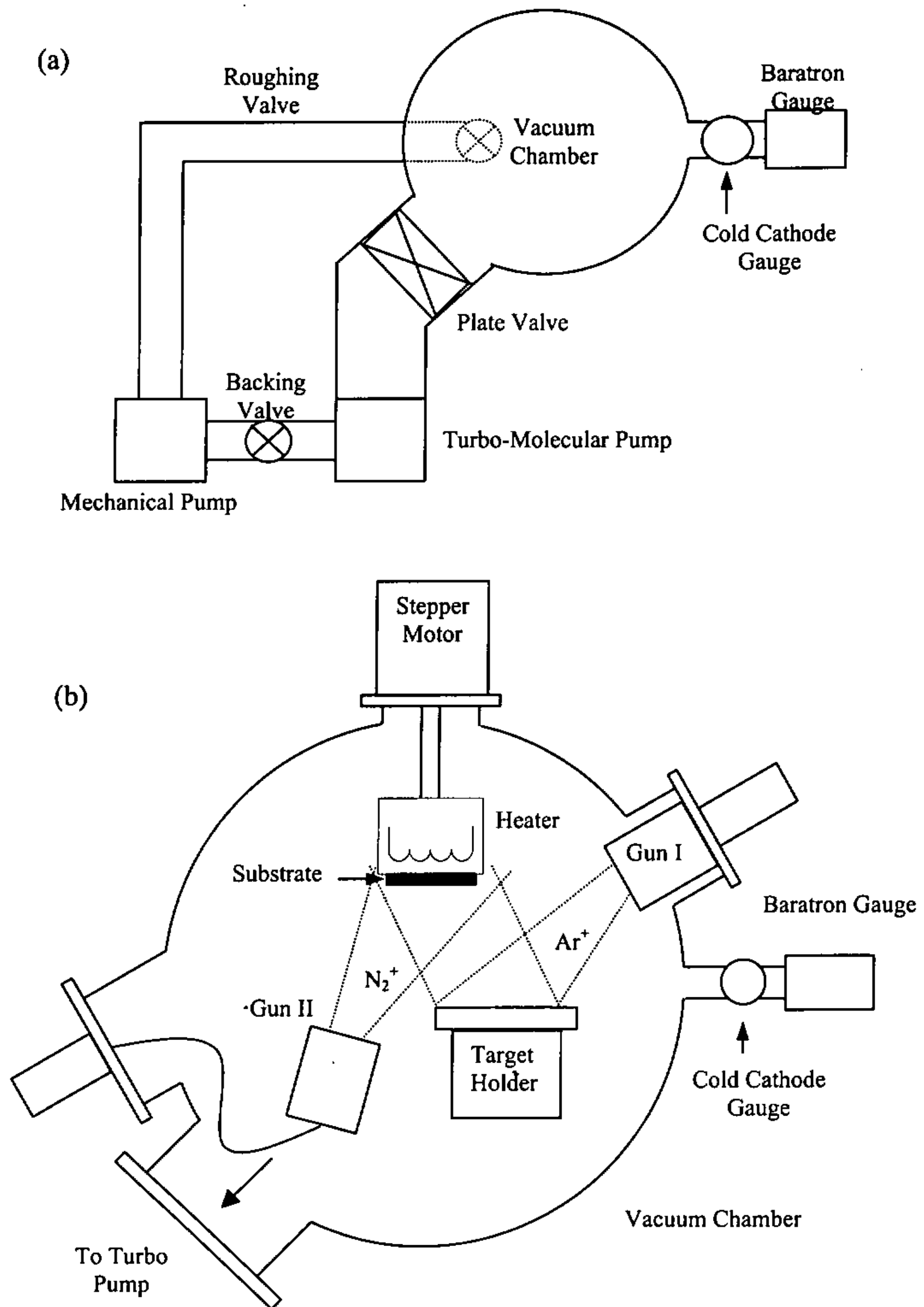

Fig. 2.1 (a) Schematic diagram of the pumping system of the dual ion beam deposition (DIBD) system. (b) Schematic diagram of the setting inside the chamber of the DIBD system.

The system consists of two 3-cm Kaufman-type ion guns (Ion Tech, Inc., model 3-1500-1000). The first one (Gun I) is a sputter ion gun used for generating an argon ion (Ar^+) beam to sputter a silicon target. The target is a 4-inch diameter, 3 mm thick, 99.999 % purity, bonded on a 3 mm thick copper back plate in order to prevent the target from cracking. The incident angle of the sputtering ion beam is 45° to the target normal. The target holder was water cooled to prevent from overheating the target during sputtering.

The other ion gun (Gun II) is used for providing ion assist. During deposition, the gun is turned on to generate a nitrogen ion (N_2^+) beam to bombard the substrate surface. The incident angle is 16° to the normal of the substrate. The N_2^+ beam current can be varied to control the N content in the deposited film. Once the chamber was pumped down to lower than 4 x 10^{-6} Torr, Ar and N_2 gases were admitted into Gun I and Gun II, respectively. The flow rates of the gases were controlled by using two mass flow controllers (MKS, Model 1259).

The substrate holder was rotated at a speed of 2.7 revolutions per minute by a step motor during deposition to ensure the film uniformity. Three different kinds of substrates were used. One was fused quartz plate and the other two were thick and thin (100) Si wafers with thicknesses of 525 and 75 μm respectively. Samples on fused quartz were specifically used for optical absorption and electrical conductivity measurements, and those on thin Si substrates were specifically used for the measurements of internal stresses.

2.2 Deposition processes and conditions

The vacuum chamber was first pumped down to a base pressure of 3×10^{-6} Torr by a turbo-molecular pump. During deposition, high purity argon gas was admitted into Gun I with a flow rate of 45.5 standard cubic centimeters per minute (sccm). An Ar^+ ion beam was generated and directed to sputter the Si target. The beam energy and current were set at 1200 eV and 70 mA, respectively (Table 2.1).

Simultaneously, high purity N_2 gas was admitted into Gun II with a flow rate of 33.5 sccm to generate an assist N_2^+ ion beam. The N_2^+ beam was directed to bombard the substrate and inject nitrogen atoms into the deposits. The beam energy of the N_2^+ assist beam was fixed at 250 eV, while the beam current was varied in the range of 0 – 45 mA to control the N content in the deposits. The ambient pressure during deposition was around 4×10^{-5} Torr. Substrate heating was not used, but the substrate temperature rose naturally to 39.8 – 84.3°C owing to the ion bombardment by the assist beam. Each deposition run lasted for 30 min. The deposition rate and other experimental data are mentioned in Chapter 4.

	Ion beam current (mA)	Ion beam voltage (eV)	Gas flow rate (sccm)
Sputter gun (Gun I)	70	1200	Ar: 45.5
Assist gun (Gun II)	0 – 45	250	N_2: 33.5

Table 2.1 A summary of the preparation conditions of the DIBD SiN_x films.

2.3 Micromachining

2.3.1 General description of isotropic and anisotropic etching techniques

Micromachining technology has been widely used in the fabrication of microsensor and actuators. Two classes of methods are widely used in micromachining technology to create free-standing microstructures such as microbridges, cantilevers and membranes [Steiner and Lang 1995]. They are isotropic etching and anisotropic etching.

For isotropic etching, etchant has no preferential etching direction associated with the crystallinity of the material to be machined. For instance, chemical solution such as hydrofluoric acid (HF) is an isotropic etchant for SiO_2 and Si_3N_4. Dry etchants like O_2 plasma and CHF_3 plasma remove photoresist isotropically as well as Si_3N_4, and are therefore isotropic etchants of the processes involved.

On the contrary, anisotropic etch has a unidirectional etch rate. For example, potassium hydroxide (KOH) is an anisotropic etchant to etch silicon. In the process of fabricating semiconductor devices, anisotropic etching is a more important technique to define patterns up to deep sub-micro scale, clear boundary of etched edges can be achieved and precisely defined. For fine-line patterning within a few micrometers and closely spaced structures, one-direction etching technique is necessary to control the pattern dimensions precisely and obtain a perpendicular side

wall. Reactive ion etch (RIE) is a typical anisotropic etching method. Ionized inert gases such as argon mixed with chemically active plasma such as CF_4 and CHF_3 assisted by a strong electric field can produce microstructures of high aspect-ratio, e.g. the ratio of deep to width of a side wall. Strong electric field perpendicular to material surface results in energetic ion bombardment on the surface, which increases the etch rate and anisotropy in the field direction. As a result, a vertical edge is acquired.

2.3.2 Isotropic etching

The etching rate of the DIBD SiN_x films against buffered hydrofluoric (BHF) acid (40% NH_4F : 25% HF : H_2O = 2:1:1) was used as etchants was measured. (See Chapter 5) This etchant is commonly used in Si-based MEMS fabrication. In particular, BHF is widely used to remove SiO_2 sacrificial layer when Si_3N_4 is used to serve as a protective material, but leaving crystalline Si intact. The data obtained help to evaluate the machinability of DIBD silicon nitride by wet etching processes. Moreover, oxygen plasma was used to clean the sample surface and remove residual photo resist, as organic contamination can be erased by oxygen plasma easily.

2.3.3 Anisotropic etching

Single crystalline Si was etched anisotropically in potassium hydroxide (43 wt.%, KOH) at 80°C. KOH shows a high etching selectivity between Si and SiN_x. It etches Si with a much faster rate compared to that of SiN_x. Reactive ion etch (RIE) system was used to remove nitride films. The samples were placed horizontally on the bottom of the reactive chamber. The chamber was first pumped down to a base pressure of 2×10^{-5} Torr. CHF_3 gas was admitted into the chamber with a flow rate of 5 sccm to reach a pressure 32 mTorr. The power of radio frequency (RF) radiation (13.56 MHz) was set to P_f = 140 W with a vertically biased field. The reflected power P_r was kept below 37 W. Well-defined microbridges with highly uniform thickness were produced by this technique. It was found that both DIBD and LPCVD nitride films have similar etch rate of about 25 nm min^{-1} in a plasma of CHF_3 gas.

Chapter 3
Sample characterization

The techniques and equipment used for examining the composition and structure of DIBD SiN_x thin films are described. The methods used for investigating the mechanical, optical and electrical properties are also mentioned in this chapter.

3.1 Compositional and structural analyses

The film thickness was measured by an α-step surface profiler. X-ray photoelectron spectroscopy (XPS) was used to determine the elemental composition and to analyze the chemical structure of the SiN_x films. Fourier transform infrared (FTIR) absorption spectroscopy was employed to explore the chemical bonds between the atoms, and an X-ray diffraction (XRD) was used to investigate the crystallinity of the films.

3.1.1 Thickness measurements

Film thickness is an important parameter for all the measurements involved. It is also used to determine the deposition rate as well as the etch rate. An α-Step surface profiler (KLA-Tencor P-10), with a vertical resolution of 1 nm, was used to measure the film thickness. This instrument has a stylus with the tip head expanding an angle of 60°. The stylus lowers vertically and slowly meanwhile, the normal load is kept extremely low. Once it touches the sample surface, the stiffness rises suddenly. During a scan, the stylus climbs up the step from the substrate surface to

film surface (Fig. 3.1). An electrical signal is then produced, which is proportional to the film thickness t_f.

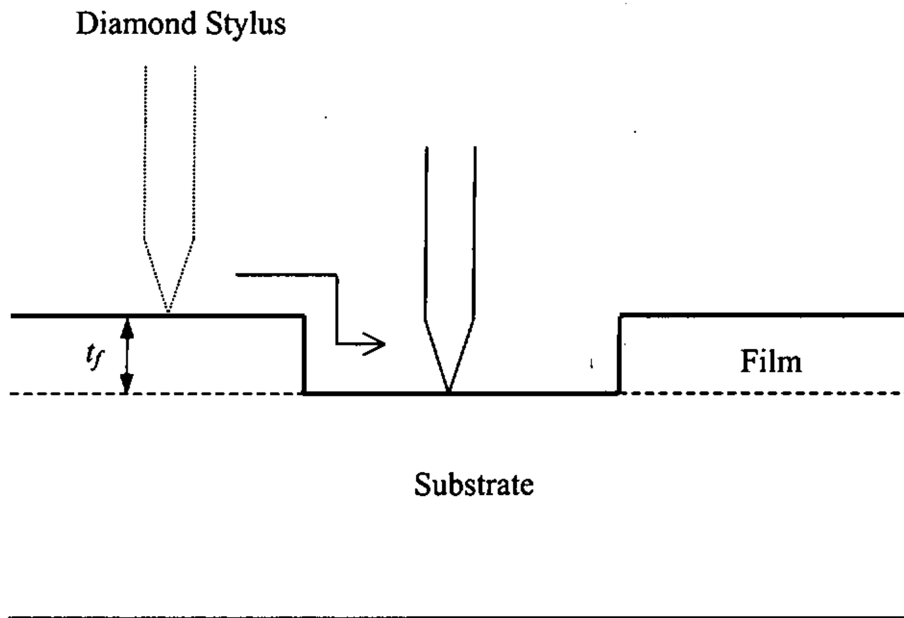

Fig. 3.1 The principle of film thickness measurement by using an α-step surface profiler.

3.1.2 X-ray photoelectron spectroscopy

The XPS is a chemically sensitive technique, which provides information on the composition and the chemical structure of a solid. X-ray is generated by bombarding an Al anode with 10 keV electrons. X-ray photons with energy $h\nu =$ 1486.7 eV hit the core electrons of the atoms in the sample. As the energy is high enough to knock out the core electrons, the electrons would escape with a kinetic energy of $E_K = h\nu - E_B$, where E_B is the binding energy. E_K is measured by an electron energy analyzer, such that E_B is determined. The characteristic values of E_B provide information on the types of elements contained in the samples. Since XPS technique can only collect information from a very shallow depth of a sample (a few atomic layers), the signal may carry some messages coming from the surface contaminants, which do not reflect the true structure of the sample under investigation. Therefore measurements were made before and after surface cleaning by an Ar^+ ion beam (4 keV, 20 mA for 3 min). The clean process helps in removing the surface contaminants.

The relative content of a certain element i, denoted as F_i, can be calculated from the integrated areas of the spectra after removal of the Shirley background according to the following formula [Shirley 1972]:

$$F_i = \frac{A_i / f_i}{\sum_j (A_j / f_j)} \times 100 \text{ at.\%}, \qquad (3.1.1)$$

where A_j and f_j are the area of the spectrum and sensitivity factor of the jth kind of element. In particular, the sensitivity factors of Si, N, O and C were assumed to be

0.27, 0.42, 0.66 and 0.25, respectively. In order to eliminate the charge-up effect on the surface of an insulating specimen, just as silicon nitride films to be observed, the peak position of the O 1s photoelectron spectra was assigned to be 532.5 eV associated with the Si-O bonding and was used as a reference for correcting the shift of other spectral lines owing to the charge up effect.

3.1.3 Fourier transform infrared absorption spectroscopy

Fourier transform infrared absorption (FTIR) covering the wavenumber range of 400 – 4000 cm^{-1} (wavelength from 25000 to 2500 nm) was performed by a Nicolet's Magna-TR™ System Model 750 FTIR spectrometer. Infrared absorption occurs when the frequency of the incident radiation matches with the natural frequency of a vibrational mode associated with one kind of chemical bonds.

An FTIR spectrum has a Michelson interferometer. The basic instrumental configuration is shown in Fig. 3.2. The incident beam is split into two beams having about the same intensity. One beam is reflected by a stationary mirror and the other is reflected by a movable mirror. Constructive and destructive interference are produced when the movable mirror moves back and front. Concurrently, the detector measures the intensity of the IR beam transmitting through the film sample. The absorption of IR radiation at different wavelengths is derived from the data via Fourier transform operation.

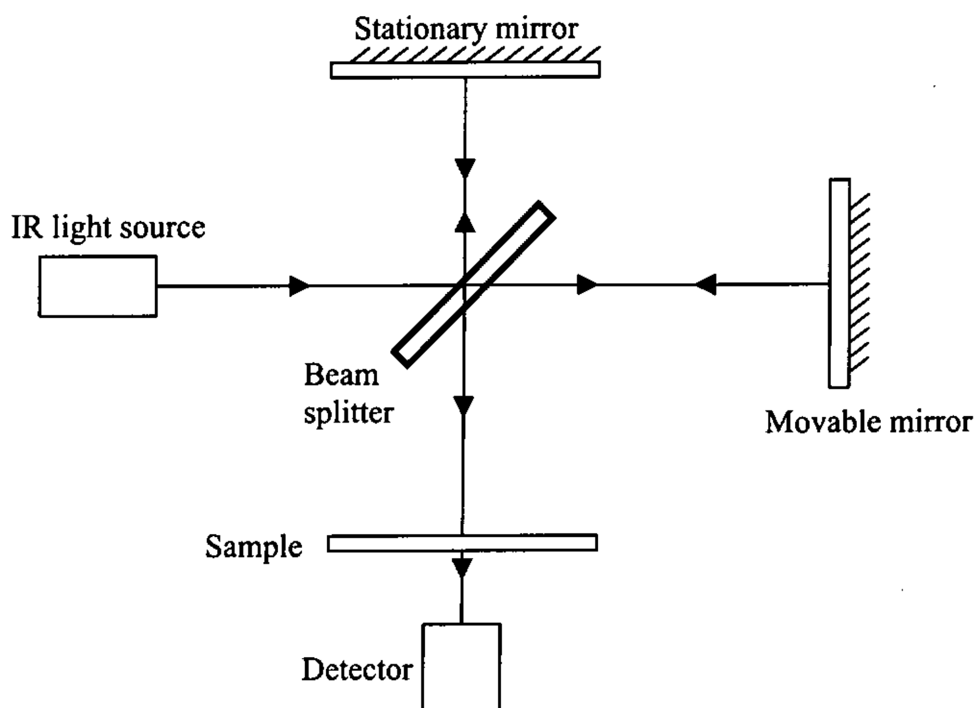

Fig. 3.2 The basic configuration of an FTIR spectrometer.

An absorption spectrum of a sample can give information on the vibrational modes of some chemical bonds [Alpert *et al.* 1970]. According to the published data, silicon nitride has an IR absorption peak at 870 cm^{-1} associated with the asymmetric stretching mode of Si-N bonds. For silicon nitride containing hydrogen, two additional IR peaks at 2150 cm^{-1} and 3330 cm^{-1} are recorded, associated with the stretching modes of Si-H and N-H bonds [Kanucki *et al.* 1998], respectively. When getting the IR absorption spectrum of a film, the absorption signal coming from the silicon substrate must be subtracted.

3.1.4 X-ray diffraction

X-ray diffraction (XRD) was performed with a Philips X'PERT X-ray diffractometer (Cu K_α radiation, wavelength λ = 0.154nm) to investigate the crystallinity of the films (Fig. 3.3). Parallel beam optics for thin film geometry was applied, and 2θ-scanning mode was used. The incident x-ray beam shined on the film surface with a small glancing angle of 7°, and the detector was driven to scan from 2θ= 15° to 65°. For a single crystal, a diffraction peak is observed when the Bragg condition is satisfied:

$$\lambda = 2d \sin \theta, \qquad (3.1.2)$$

where d is the lattice spacing. The d values of some major lattice planes of silicon and silicon nitride are listed in Table 3.1 [JCPDS 33-1160, 41-360, 40-1129].

Element	*hkl*	*d* (nm)
Si	(111)	0.226
Si	(220)	0.138
Si	(311)	0.118
α-Si_3N_4	(101)	0.431
α-Si_3N_4	(201)	0.288
α-Si_3N_4	(102)	0.259
α-Si_3N_4	(210)	0.254
β-Si_3N_4	(200)	0.329
β-Si_3N_4	(101)	0.266
β-Si_3N_4	(210)	0.249

Table 3.1. d spacings of some major lattice planes of Si and Si_3N_4 in XRD experiment.

For an amorphous sample, board halos are generally observed, but no sharp characteristic peak can be seen. The size of clusters b, in which short range order analogous to that in the corresponding crystalline phase, can be estimated from the full width at half maximum (FWHM) of the halo according to the Debye-Scherrer formula [Cullity 1956]:

$$\text{FWHM (in radian)} = \frac{0.9\lambda}{b \cdot \cos\theta} \tag{3.1.3}$$

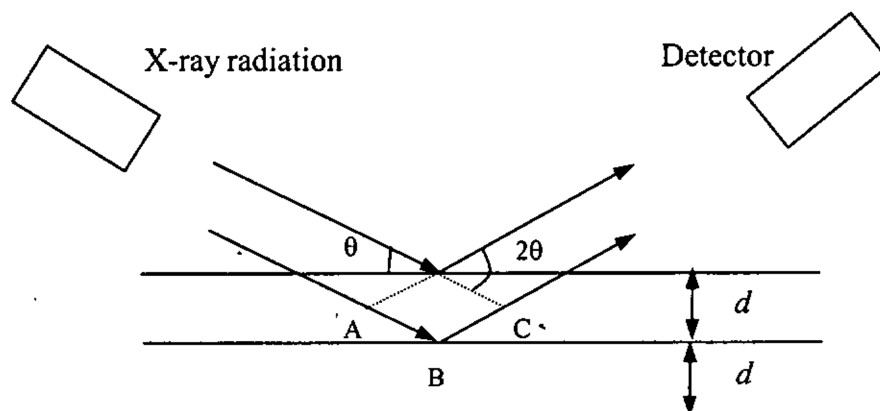

Fig. 3.3 Schematic presentation of the principle of X-ray diffraction. Path difference between the two incident rays = AB + BC.

3.2 Mechanical properties

Investigations on the mechanical properties of the SiN_x films are particularly envisaged in this study. A nanoindentor with a Berkovich diamond tip was used to evaluate the hardness (H) and elastic modulus (E_m) of the film samples. Furthermore, a wedge tip was used for getting the load-displacement relationship of the CVD silicon nitride microbridges. An optical system was established to determine the film internal stress based on the measurement of the radius of curvature of the film-on-substrate structure. In addition, a ball-on-disc tribometer was used to determine the friction coefficient of the films.

3.2.1 Hardness and elastic modulus measurements

The hardness (H) and elastic modulus (E_m) of the films were measured using a Nanoindenter® (Nano Instruments Inc., Model IIs). It is well known that the reliability of a nanoindentation test relies strongly on the accuracy of the calibration of the load frame stiffness and the area function of the diamond tip. With this concern, we carried out the calibration ourselves. The tip area function generated was believed to be accurate to contact depth of around 1 nm. Theoretically, the minimum load of this instrument is as low as 500 nN, and the resolution of the penetration depth is claimed to be as good as 0.04 nm. With such a low load range, the influence of substrate deformation in a hardness test is practically negligible.

The nanoindentor having a Berkovich 3-sided pyramidal diamond tip was used to indent the sample surface. The applied load is added by passing a current through a coil, which controls the motions of a permanent magnet mounted to the indenter shaft. The displacement of the indenter head is measured by a capacitance displacement gauge. The electrical signal generated by the displacement head is recorded by a computer.

Six different indentation experiments were designed to apply on each sample. Each experiment contained twelve segments, including three loading segments with successively increasing normal loads. The values of the maximum loads set in the six experiment are listed in Table 3.2. Each experiment was repeated five times at five different fresh points. A complete test on a specimen contains 30 indents arranged in a 6 x 5 array. Any two adjacent indents were separated by a distance of 50 μm. Data points obtained at similar maximum loads were averaged, and the deviation of the data point gave an estimate of the experimental random error. The range of maximum load was varied from 70 μN to 80 mN. In particular, the average of the data obtained at indentation depths around 20 nm was used to represent the mechanical properties of the film samples. At this depth, the results obtained were almost independent on the indentation depth and so the influence from the deformation of the substrate was assumed to be negligibly small.

Experiment	Indentation	Maximum load (μN)		
1	1 – 5	300	1400	3300
2	6 – 10	150	500	2200
3	11 – 15	120	350	960
4	16 – 20	110	250	680
5	21 – 25	70	210	430
6	26 – 30	7500	20000	80000

Table 3.2. The setting of maximum loads assigned in the six nanoindentation experiments.

Fig. 3.4 shows the typical features of the loading and unloading curves. The unloading curve is used to calculate the hardness and elastic modulus. It is first fitted to a power law function:

$$P = K(h-h_f)^m, \tag{3.2.1}$$

where P and h are the applied load and displacement of the diamond tip, K and m are constants. h_f is the depth of indent after the normal load is completely removed. The elastic deformation at maximum load $P_{\max}$ is h_e (Fig. 3.4). The stiffness S at P_{max} is equal to the slope of the unloading curve at P_{max}. h_e is therefore equal to:

$$h_e = \varepsilon \frac{P_{\max}}{S}, \tag{3.2.2}$$

where ε is set to be 0.75 for a indenter head having a parabolic revolution geometry. The plastic displacement (contact depth) h_c is determined as:

$$h_c = h_{\max} - h_e, \tag{3.2.3}$$

where $h_{\max}$ is the overall displacement of the tip at $P_{\max}$. The contact area is calculated from h_c and the area function $A(h_c)$.

The film hardness H can be found as:

$$H = \frac{P_{max}}{A(h_c)}. \quad (3.2.4)$$

The reduced elastic modulus E_r can also be determined by the formula :

$$S = \frac{2}{\sqrt{\pi}} E_r \sqrt{A(h_c)}, \quad (3.2.5)$$

where E_r is defined as:

$$E_r = \left[\frac{1-\nu_i^2}{E_i} + \frac{1-\nu_s^2}{E_m} \right] \quad (3.2.6)$$

In equation (3.2.6), $\nu_i = 0.07$ and $E_i = 1141$ GPa are the Poisson's ratio and elastic modulus of diamond, and ν_s represents the Poisson's ratio of the film and is set to be 0.24 for our samples [Oliver *et al.* 1992]. The elastic modulus E_m of the film can thus be calculated.

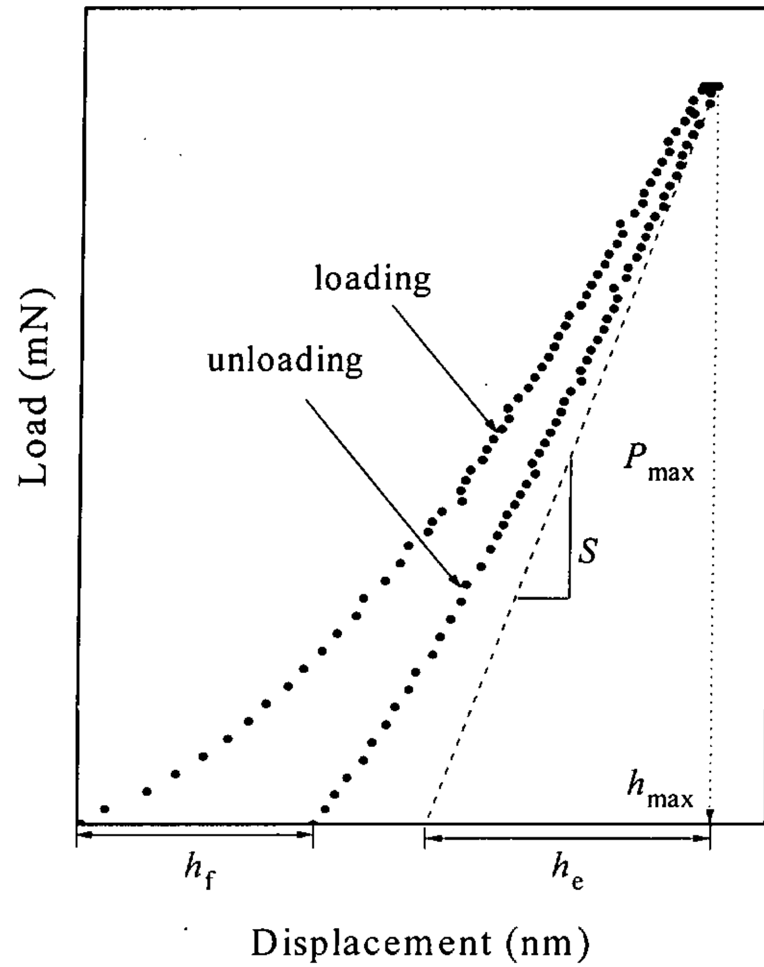

Fig. 3.4 A typical pattern of load-unload curve of a nanoindentation.

3.2.3 Tribological tests

The friction coefficient of the films was measured by using a CSEM pin-on-disk tribometer. The sample was mounted on a rotating stage. A stainless steel ball with a diameter of 6 mm was pressed on the film surface with a normal load of 2N, such that the ball scratches on the film surface on a circular track with radius of 0.2 cm. This setting is equivalent to drive the ball to scratch on the film surface with a linear speed of 3 cms^{-1}. The total number of revolutions is set to be 10000. The frictional force was recorded continuously, such that the friction coefficient can be calculated as a function of traveling distance or number of revolutions.

3.2.4 Stress analyses

The internal stress of the films was determined from the radius of curvature of the film-on-substrate configuration [Flinn *et al.* 1987] measured by using an optical system as shown in Fig. 3.6.

When a laser beam scans across the film surface by a distance Δx, the reflected spot shifts correspondingly on the surface of a position sensor by a distance ΔD. The radius of curvature R is calculated as:

$$R = \frac{2 \cdot L \cdot \Delta x}{\Delta D}, \qquad (3.2.7)$$

where L is the distance between a lens and the film surface. The internal stress of the film σ_s is calculated from the Stoney Equation [Stoney *et al.* 1909]:

$$\sigma_s = \frac{E_s}{(1-\nu_s)} \cdot \frac{t_s^2}{6 \times R \times t_f}. \tag{3.2.8}$$

where E_s and ν_s are the Young's modulus and Poisson's ratio of the substrate, respectively. t_s = 75 μ m is the thickness of the substrate, and t_f is the thickness of the film. The value of $E_s/(1-\nu_s)$ is set at 180.5 GPa for (100) Si substrate [Brantley 1973]. In addition, from the direction of bending, one can identify whether the stress is compressive or tensile. By convention, R is negative for convex curvature (compressive stress) and positive for concave curvature (tensile stress) [Hattangady *et al.* 1989].

The whole set up is placed on an optical table. A 20 mW He-Ne laser (Oriel Instruments, Model 1135) is used as the light source. To get a measurable radius curvature R, samples deposited on 75 μm thick (100) Si wafers were used for tests. The sample was placed on a movable stage, which was driven by a stepper motor (Oriel Instruments, Model 18152). When the sample stage moved horizontally, the reflected beam shifted correspondingly, such that the position of the reflected light spot on the position sensor was shifted. In addition, a lens with a focal length L of 1 m was used to focus the laser beam on sample surface. [Witvrouw and Spaepen 1990].

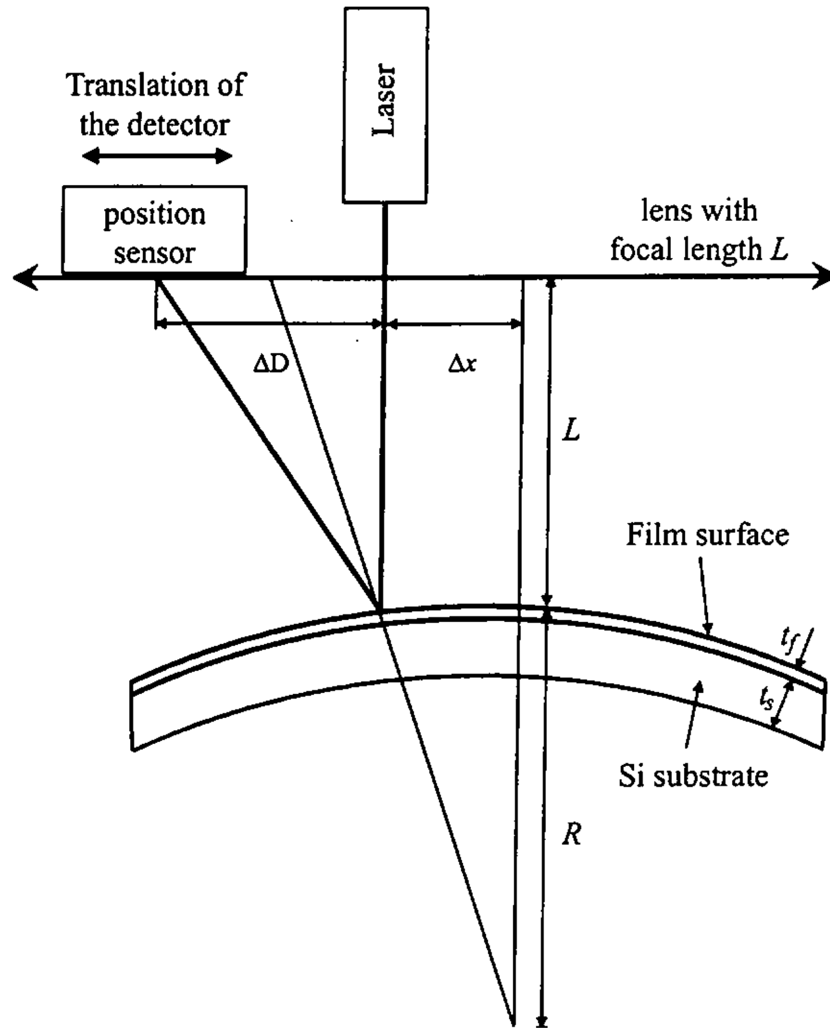

Fig. 3.6 The principle of the measurement of the radius of curvature of a film-on-substrate configuration.

3.3 Optical absorption

For the optical analysis, the transmittance spectrum was obtained by a Cary 5G UV-VIS-NIR spectrometer. The optical spectra of the films deposited on quartz in the photon energy $h\nu$ range of 0.5 – 5.5 eV were measured. This is a double beam spectrophotometer, in which there are two holders. One is used to mount a blank substrate and the other is used to mount a film-on-quartz sample. The absorption due to the substrate is thus automatically subtracted.

Basically, the absorption coefficient α at a wavelength λ is defined by the relationship: $I = I_0 \cdot \exp(-\alpha t)$ where t is the film thickness, and I_o and I are the light intensity of the incident and transmitting light at that wavelength. The optical absorption spectrum of a solid provides the information on the band gap and density of electron states (DOS) of a substance.

Tauc plot [Tauc 1972] is well know to be used for describing the relationship between α and $h\nu$ of amorphous materials:

$$(h\nu\alpha)^{1/2} \propto (h\nu - E_{opt}) \qquad (3.3.1)$$

where E_{opt} is defined as the optical band gap. Therefore, a linear relationship between $(h\nu\alpha)^{1/2}$ and $h\nu$ is produced at high $h\nu$ region. From the extrapolation of this linear part, the intercept on the $h\nu$-axis would give the value of E_{opt} [Feltz 1993].

The absorption at low $h\nu$ is relatively lower. This part of absorption contains information associated with the electron transitions involving localized states. One simple model was proposed by Urbach [Urbach 1953]:

$$\alpha(\nu) \propto e^{h\nu/E_o} \tag{3.3.2}$$

where E_0 represents the width of the exponential band tail.

3.4 Electrical conductivity measurements

A set-up was established to measure the temperature dependence of the electrical conductivity σ_c of the film samples. Samples on fused quartz were used for the measurements. Two silver paint electrodes were used on the sample surface, with a separation of l. As shown in Fig. 3.7, a d.c. power supply (Pasco Scientific, Model SF-9585) provides a voltage output V_o (maximum = 500 V). A variable resistance box (R_s = 10^4, 10^5,..., 10^{10} Ω) is connected in series with the sample. An electrometer (Keithley Instruments, Model 617) is used to measure the voltage drop V_m across R_s such that the resistance R_x of the sample between the two conducting electrodes is determined as:

$$R_x = R_s \frac{V_o - V_m}{V_m} \; (\Omega) \qquad (3.4.1)$$

and

$$\sigma_c = \frac{l}{w \cdot t_f \cdot R_x} \; (\Omega^{-1}\mathrm{cm}^{-1}), \qquad (3.4.2)$$

where w and t_f are the width and thickness of the film.

We measure the temperature dependent dc electrical conductivity of SiN_x films on quartz by keeping the output of the dc power at applying 400 V. The temperature was varied from 193 K to 573 K. Liquid nitrogen was used as the cooling medium. The sample was kept in a high vacuum condition during measurements.

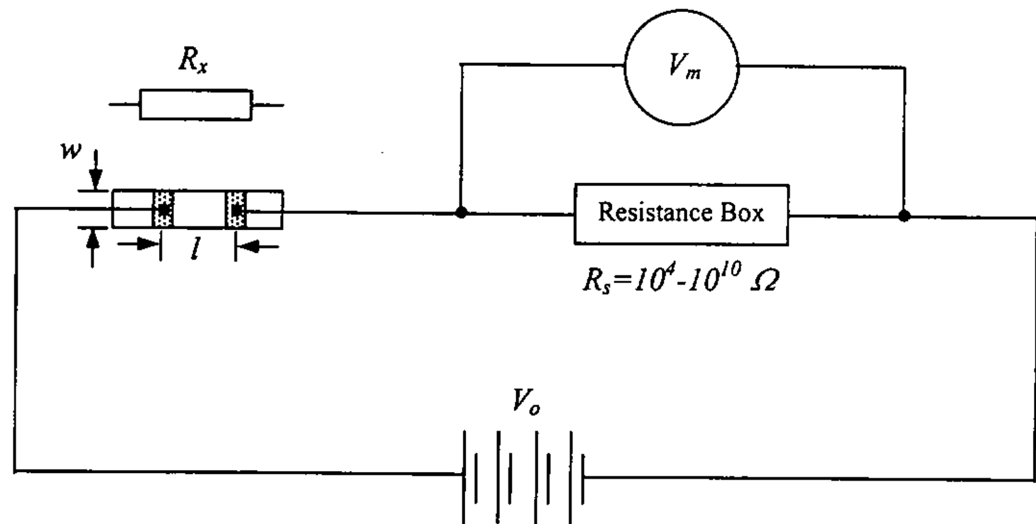

Fig. 3.7 The set up for electrical conductivity measurement.

Chapter 4
Composition and structure

In this chapter, we present the structure of the DIBD deposited SiN_x. First, in section 4.1, results of film thickness and coating rate are discussed. Second, the compositional and structural information revealed by XPS, FTIR and XRD are summarized and analyzed in section 4.2 to 4.4.

4.1 Thickness and coating rate

The thickness and coating rate of eight selected DIBD SiN_x film samples are tabulated in Table 4.1. The thickness of the films, deposited on a variety of substrates including 525 μm thick Si wafer, 75 μm thick Si wafer and 1 mm thick fused quartz, varies in a rather narrow range between 376 and 453 nm. Correspondingly, the coating rate was calculated to be in the range of 12.5 to 16.3 nm min^{-1}.

As shown in Fig. 4.1, the coating rate of DIBD SiN_x films is basically independent on the applied assist N_2^+ ion beam current in the range of 0 – 45 mA, provided that the scattering of the data points is attributed to statistical fluctuation. We suggest that the rise in the beam current of the assist ion beam enhances resputtering of the deposits on one hand, while on the other hand, more N atoms are incorporated into the films. The two effects compensate each other, leaving the film thickness to remain almost unchanged.

Sample code	Assist N_2^+ ion beam current (mA)	Thickness (nm)	Substrate	Coating rate (nm min^{-1})	Substrate temperature (°C)
T117		387	525 μm-Si	12.9	39.8
T117A	0	387	75 μm-Si	12.9	39.8
T117Q		379	Quartz	12.6	39.8
T103		412	525 μm-Si	13.7	50.3
T116	10	376	75 μm-Si	12.5	57.4
T103Q		440	Quartz	14.7	50.3
T106		399	525 μm-Si	13.3	54.2
T111	15	400	75 μm-Si	13.3	67.1
T106Q		422	Quartz	14.1	54.2
T105		425	525 μm-Si	14.2	61.1
T112	20	400	75 μm-Si	13.3	69.6
T105Q		428	Quartz	14.3	61.1
T107		412	525 μm-Si	13.7	69.9
T115	25	391	75 μm-Si	13.0	70.7
T107Q		419	Quartz	14.0	69.9
T104		489	525 μm-Si	16.3	69.7
T114	30	409	75 μm-Si	13.6	74.3
T104Q		452	Quartz	15.1	69.7
T113		386	525 μm-Si	12.9	84.3
T113A	40	386	75 μm-Si	12.9	84.3
T113Q		350	Quartz	11.7	84.3
T110	45	453	525 μm-Si	15.1	84.5
T110Q		439	Quartz	14.6	84.5

Table 4.1 Thickness, coating rate and substrate temperature of DIBD SiN_x film samples deposited on different substrates and at different assist N_2^+ ion beam currents.

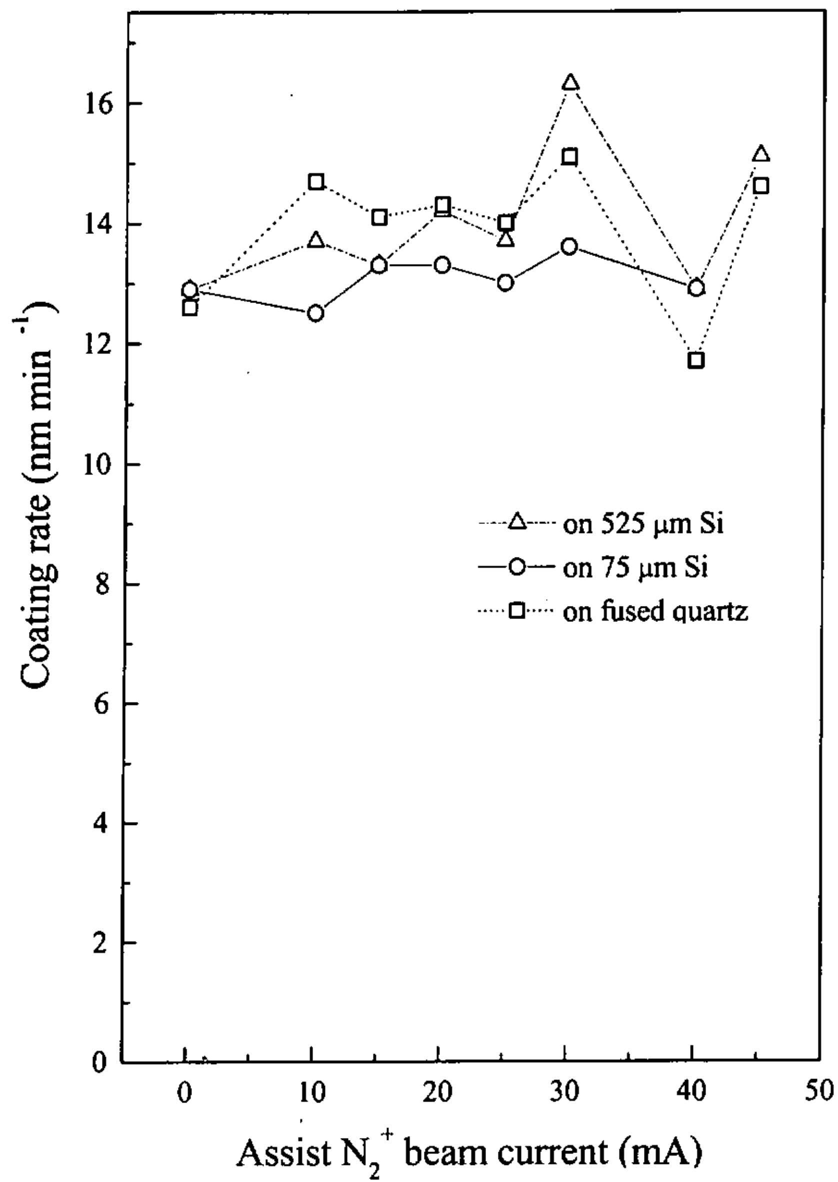

Fig. 4.1 Coating rate of DIBD SiN_x films on 525 μm thick Si, 75 μm thick Si and fused quartz substrates.

Rathi [Rathi 1987] pointed out that the coating rate can be altered from system to system and for most of the conditions used it is around 12 nm min^{-1}. For PECVD technique, the rate of silicon nitride at 300 °C and 0.3 Torr pressure is 7.6 nm min^{-1} [Kuwano 1969], which is rather lower than the result obtained for our DIBD SiN_x films. Sinha [Sinha *et al.* 1978] and Blaauw [Blaauw *et al.* 1984] reported that, the coating rate of PECVD SiN_x films could be significantly affected by deposition temperature and chamber pressure. However, all these parameters were kept unchanged in our DIBD processes. It is therefore reasonably to find that the thickness of our samples is basically not changed.

4.2 Composition determined by X-ray photoelectron spectroscopy

From the integrated areas of the Si 2p, N 1s, C 1s and O 1s photoelectron spectra, the relative contents of the elements are determined. First of all, the oxygen content recorded before surface cleaning by Ar ions is as high as 40 at.%. After surface cleaning, the oxygen content drops to 6 – 20 at.%. This shows that conspicuous amount of oxygen is trapped on the film surface, but these surface sorbed oxygen atoms can be removed by ion bombardment.

Fig. 4.2 shows the relative contents of Si, N, C and O in the DIBD SiN_x films as functions of assist N_2^+ ion beam currents after surface cleaning by Ar^+ ions. The C contaminant is introduced mainly from the inner wall of the stainless steel chamber sputtered by scattered ions. It is found that the O content remains at around 6 at.% even after further ion etching to a depth of 300 nm below the film surface, according to the calibration of the ion etching rate for standard material. This high O level shows that a considerable amount of oxygen is incorporated into the interior of the deposits.

The inclusion of the high oxygen content in the interior of films could be originated from the mechanism related to contamination in the working chamber. The mechanism is associated with the incorporation of oxygen atoms from residual oxygen and water vapor in the chamber during deposition process. It should point out that when ion beam current is increased, oxygen content in the film also decreases,

probably because the arriving oxygen atoms are more readily to be resputtered by the assist ion beam [Yoon *et al.*1992].

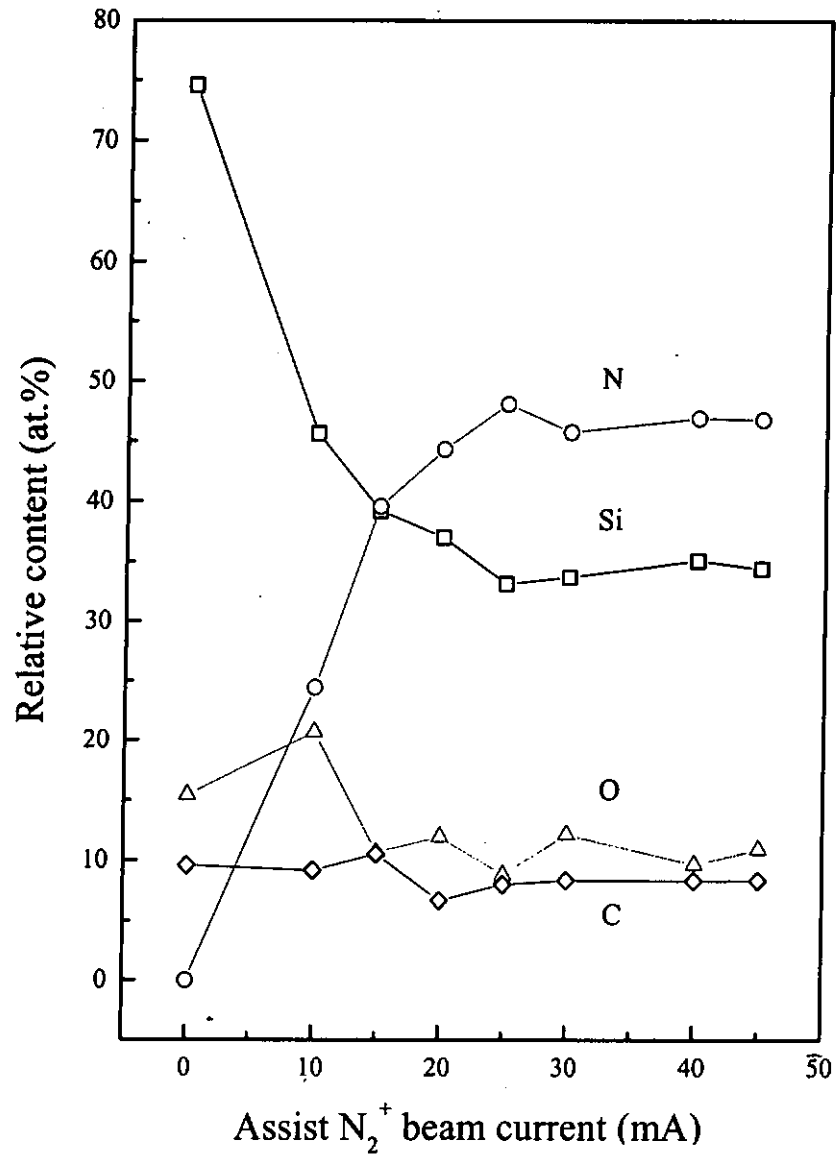

Fig. 4.2 Relative content of Si, N, O and C as a function of assist N_2^+ beam current.

When the assist N_2^+ beam increases, the relative content of Si drops accordingly. At the same time, the relative content of N content rises. The effective N-to-Si ratio is defined and calculated as follows. It is assumed that most of the Si and N atoms are combined to generate a Si-N phase, while the rest of the Si atoms combine with O atoms to give a Si-O phase which has a small volume fraction. The properties of the films are mainly determined by the Si-N phase. If the Si-to-O ratio in the Si-O phase is assumed to be in the ratio of 1:2 analogous to that of SiO_2, then the N-to-Si ratio in the Si-N, defined as x, can be calculated, and the associated Si-N phase is designated to be SiN_x phase. The value of x is assumed to be the most important parameter affecting the properties of the DIBD SiN_x films, and will be referred as the major control parameter when discussing the film properties thereafter. The calculated value of x based on this assumption is plotted in Fig. 4.3 as functions of assist ion beam currents, and is tabulated in Table 4.2.

As shown in Fig. 4.3, x rises with increasing assist beam current first and then saturates at a value of 1.36 when the assist beam current is $\geq$ 30 mA. The saturated value of x is very close to 1.33 of the stoichiometric Si_3N_4 structure. Saturation of N-to-Si ratio at stoichiometric value has also been observed in ion beam deposited silicon nitride as reported by Erler et al. 1980, leading one to suggest that at this atomic ratio the N and Si atoms tend to mix to generate a stable amorphous structure, which would possess a short range order analogous to that of crystalline Si_3N_4.

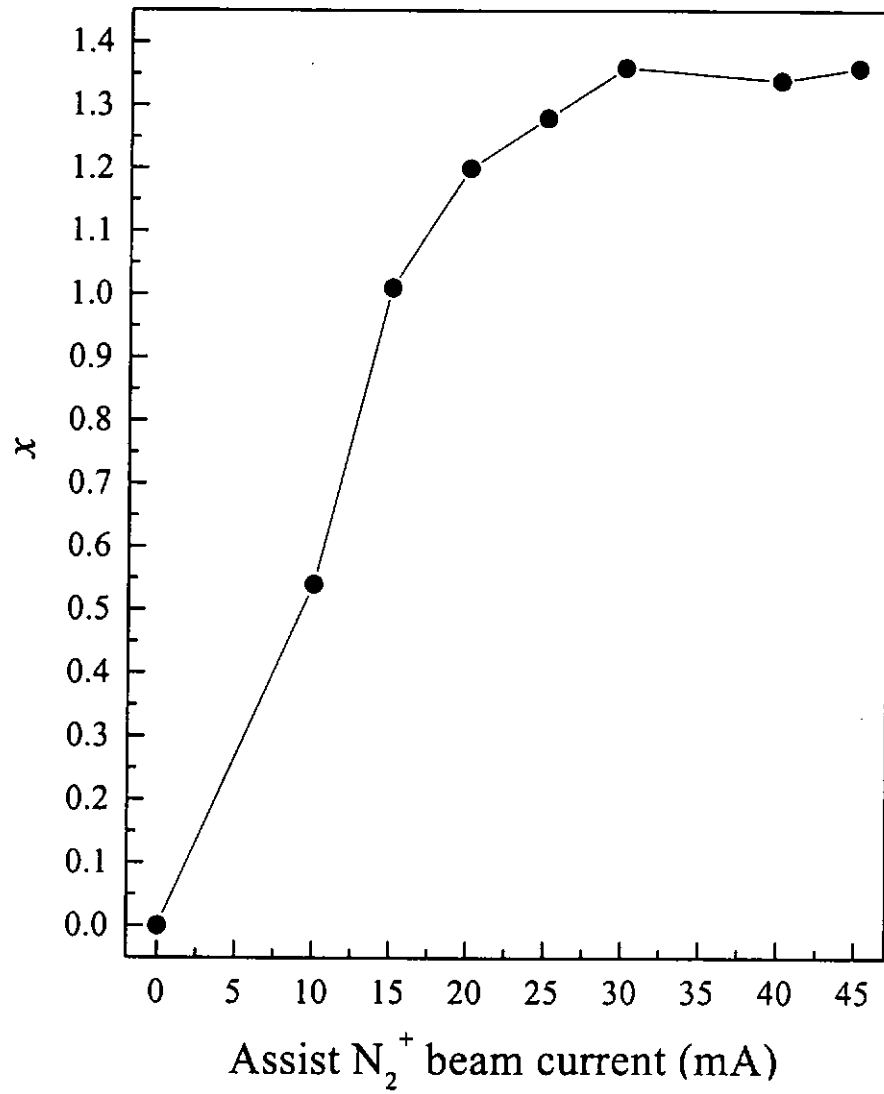

Fig.4.3 N-to-Si ratio *(x)* as a function of assist N_2^+ beam current.

Sample code	Assist N_2^+ ion beam current (mA)	N-to-Si ratio (x)
T117	0	0
T116	10	0.54
T106	15	1.01
T105	20	1.20
T107	25	1.28
T104	30	1.36
T113	40	1.34
T110	45	1.36

Table 4.2 N-to-Si ratio (x) of DIBD SiN_x films deposited at different assist N_2^+ ion beam currents.

4.3 Chemical structure analyzed by X-ray photoelectron spectroscopy

To analyze the XPS data, first we have to eliminate the error in determining the binding energy of photoelectrons due to charge up effect at the sample surface. It is observed that every spectrum contains one component only, we assumed that the O 1s peak comes from the Si-O bonds in the films, which is reported to have a peak energy at 532.5 eV. With this as a reference, the energy axis of the whole spectrum was adjusted. This adjustment leads to reasonable assignments and interpretations of the chemical structures among the atoms obtained from analyzing the peak positions of the photoelectron spectrum lines. The XPS data obtained after surface cleaning are summarized in Table 4.3 whereas the adjusted peak positions of the components obtained according to the above guideline are given also.

Element	x	Relative content (at. %)	Peak position (eV)	Charging effect (eV)	Corrected peak position (eV)
Silicon	0	74.58	100.9	- 0.6	100.3
	0.54	45.66	101.5 103.2	- 1.2	100.3 102
	1.01	39.22	102.3 103.5	- 1.5	100.8 102
	1.20	37.01	104.3	- 2.9	101.4
	1.28	33.15	104.4	- 2.5	101.9
	1.36	33.72	104.4	- 2.4	102.0
	1.34	35.09	103.7	- 1.4	102.3
	1.36	34.40	104.1	- 2.1	102.0
Nitrogen	0	0	--	--	--
	0.54	24.47	399.3	- 1.2	398.1
	1.01	39.57	399.5	- 1.5	398.0
	1.20	44.32	400.4	- 2.9	397.5
	1.28	42.43	400.4	- 2.5	397.9
	1.36	45.75	400.3	- 2.4	397.9
	1.34	46.90	399.3	- 1.4	397.9
	1.36	46.78	399.8	- 2.1	397.7
Oxygen	0	15.42	533.7	- 0.6	532.5
	0.54	20.68	534	- 1.2	532.5
	1.01	10.68	535.4	- 1.5	532.5
	1.20	11.96	535	- 2.9	532.5
	1.28	8.69	534.9	- 2.5	532.5
	1.36	12.16	533.9	- 2.4	532.5
	1.34	9.67	533.1	- 1.4	532.5
	1.36	10.92	534.6	- 2.1	532.5
Carbon	0	9.61	284.3 286.1	- 0.6	283.7 285.5
	0.54	9.19	284.5 286.2	- 1.2	283.3 285
	1.01	10.53	284.8 286.9	- 1.5	283.3 285.4
	1.20	6.70	285.5 287.3	- 2.9	282.6 284.4
	1.28	8.04	287.6	- 2.5	285.1
	1.36	8.37	287.4	- 2.4	285
	1.34	8.34	286.6	- 1.4	285.2
	1.36	8.36	286.3	- 2.1	284.2

Table 4.3 Summary of XPS data obtained after surface cleaning.

Fig. 4.4 shows the C 1s photoelectron spectra of all the samples. The spectra of the sample deposited with $x \leq 1.20$ contain two components. The component at 285 eV is assigned to C-C bonds such as those in hydrocarbon molecules, and is very close to that associated with the structure at 284.7 eV [Olefjord 1997]. The other small component at 283.3 eV is more likely related to the presence of Si-C bonds, which is reported to have a peak energy of 283.7 eV [Rusli *et al.* 2000]. The appearance of Si-C bonds is quite possibly as for these group of films, the Si content is higher, and so there is a greater chance for the Si atoms and some accidentally arriving C atoms to combine. For the films with higher values of x, the relative content of Si is smaller. As a consequence, the Si-C component does not appear and only that from hydrocarbon molecules is observed.

The Si 2p photoelectron spectra shown in Fig. 4.5 illustrate the formation of Si-N bonds. For the Si film with $x = 0$, the spectrum contains only one component having a peak position at 100.3 eV. This spectrum reflects that Si-Si bonds have been formed in the films. When N is incorporated into the films, a component at the energy of 102 eV appears. This component is ascribed to the formation of Si-N bonds [Wittberg 1978].

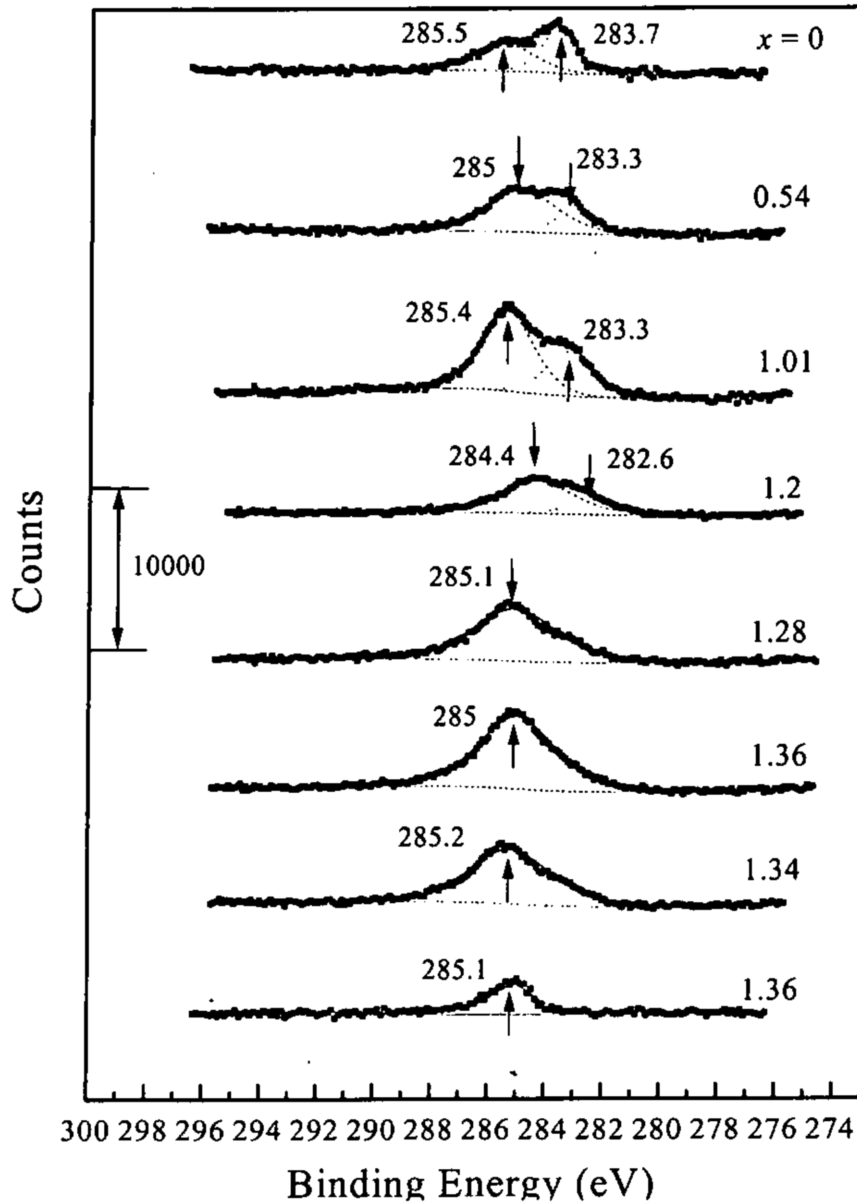

Fig. 4.4 C 1s photoelectron spectra of DIBD SiN_x films with different values of x, recorded after surface cleaning.

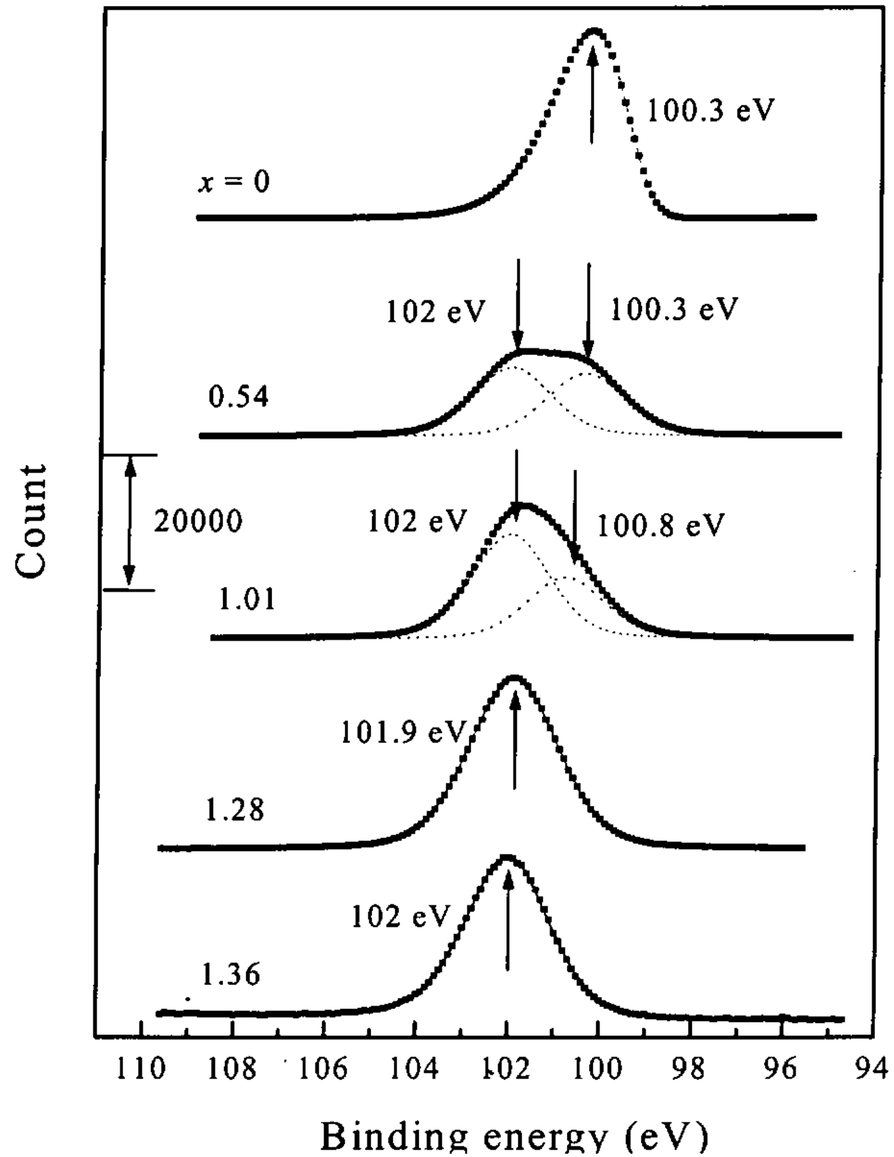

Fig. 4.5 Si 2p photoelectron spectra of DIBD SiN_x films with different values of x, recorded after surface cleaning.

For the samples with x = 0.54 and 1.01, the Si 2p spectrum contains two components. One is peaked at about 100.3 – 100.8 eV, which can be assigned to a phase constructed of Si-Si bonds. The next is peaked at 102 eV, most likely to be related to a phase constructed of Si-N bonds. This is explained considering that for these films the Si concentration is so high that part of the Si atoms could be completely surrounded by other Si atoms, while the rest could have N atoms as neighbours. These two types of Si atoms eventual lead to the formation of the above two components respectively.

When x is close to 1.28, the component associated with Si-Si bonds is not seen, but only the component at 102 eV is left. This is because when more N is added, a Si atom would have greater chance to combine with N atoms. Therefore, the Si-N bonds dominate the film structure when x approaches the stoichiometric value.

Fig. 4.6 shows the N 1s photoelectron spectra of the films deposited with different x values after surface cleaning. Each of them contains a single peak only. The N 1s spectra have peak values varying within 397.5 – 398.1 eV. Higher of x value corresponds to a larger peak area because the N content in the film becomes higher.

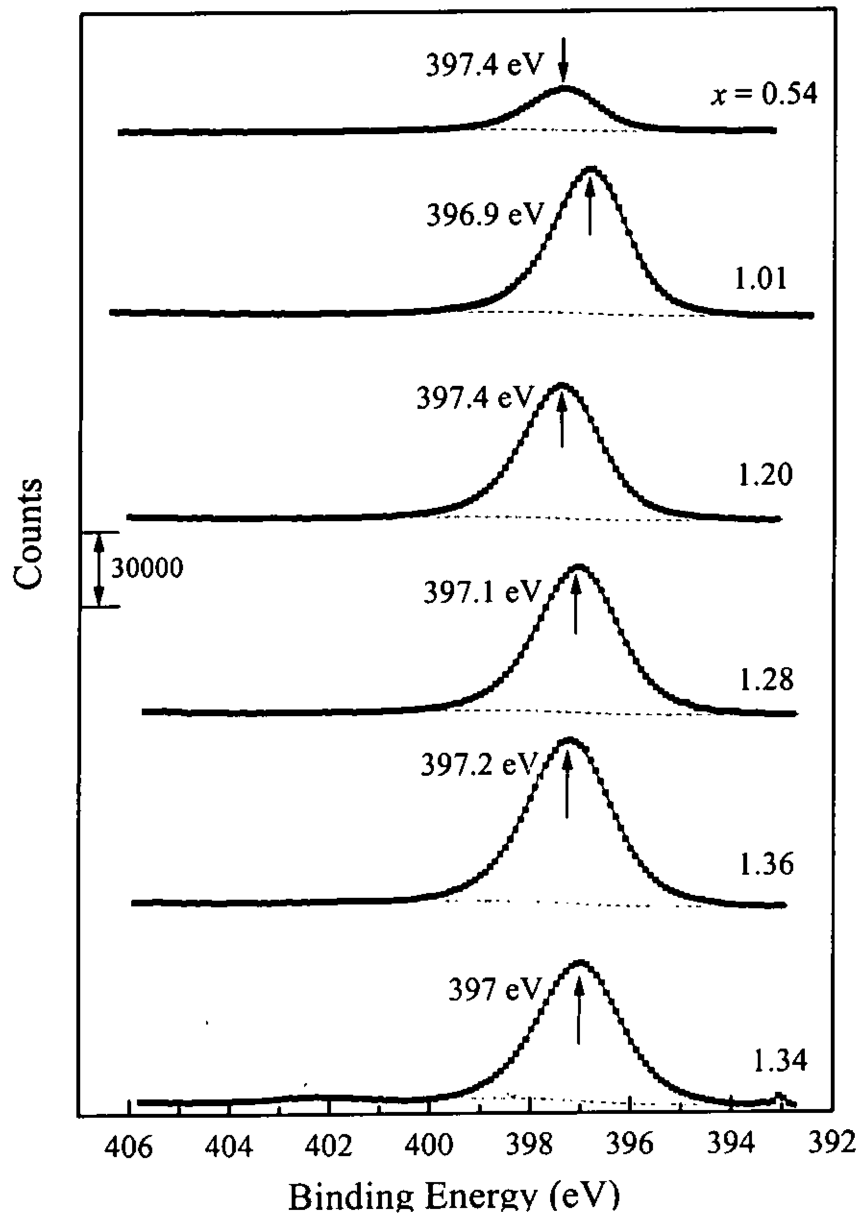

Fig. 4.6 N 1s photoelectron spectra of DIBD SiN_x films with different values of x, recorded after surface cleaning.

4.4 Fourier transform infrared absorption

FTIR was used to determine the chemical bonds in the deposits. First of all, as shown in Fig. 4.7, for the film with x = 0 (pure Si), the IR spectrum shows no characteristic absorption band. This is understood that without N atoms, the film is constructed of Si atoms only, which bond with a short range order analogous to that in crystalline Si. It is well known that silicon does not have IR peak due to the symmetric geometry of the bonds. Therefore, the IR spectrum of the Si film with x = 0 has no peak. After incorporating a certain amount of N, e.g. x = 0.54, a strong absorption band appears at 850 cm^{-1}, which is associated with the stretching mode of Si-N-Si bonds [Liao *et al.* 1994 and Yoon *et al.* 1992]. This result provides an additional evidence to show the successful formation of Si-N bonds. The peak positions and full width half maximum (FWHM) of the absorption spectra are almost the same for all the samples with different x values.

Comparing to plasma enhanced chemical vapor deposited (PECVD) silicon nitride films deposited at low temperature (e.g. 100°C), DIBD SiN_x films are more stable and do not degrade by oxidation in air. The structure of PECVD silicon nitride films deposited at low temperature is rather porous. H_2O molecules from air diffuse and penetrate through the pores readily, and lead to rapid oxidation of the films [Liao *et al.* 1994]. Oxidation process can be monitored by observing the IR band, where the band associated with the Si-N-Si stretching mode shifts toward 900 cm^{-1}, and some IR bands at 460 cm^{-1} (Si-O-Si rocking mode), 820 cm^{-1} (Si-O-Si bending) and

1070 cm^{-1} (Si-O-Si stretching) emerge. Moreover, some H_2O-related bands at 1620 3640 and 2800 – 3700 cm^{-1} appear [Liao *et al.* 1994 and Yoon *et al.* 1992].

The reasons for our room temperature deposited DIBD SiN_x to be more stable are as follows. First, the DIBD SiN_x films are intrinsically hydrogen-free. As observed in Fig. 4.8, no hydrogen related peaks are observed in the spectra, such as the Si_2N-H rocking and N_2Si-H stretching modes reported to be located at 1170 and 2150 cm^{-1}, respectively [Liao *et al.* 1994]. Second, although the DIBD SiN_x are detected to contain a certain amount of oxygen (6 at.%), but the oxygen atoms are more likely to combine with other atoms in the atomic network in a more stable manner. None of the oxygen related IR peaks observed for PECVD silicon nitride as marked in Fig. 4.7 appear in the spectra of our DIBD SiN_x films. All these characteristics of atomic bonds in the DIBD SiN_x films give rise to a much stable structure and stronger oxidation resistance of DIBD SiN_x compared to PECVD silicon nitride. Third, the use of ion assist directed during deposition is expected to have the effect of densifying the film structure, such that diffusion of water molecules from air into the deposits is more strongly hindered.

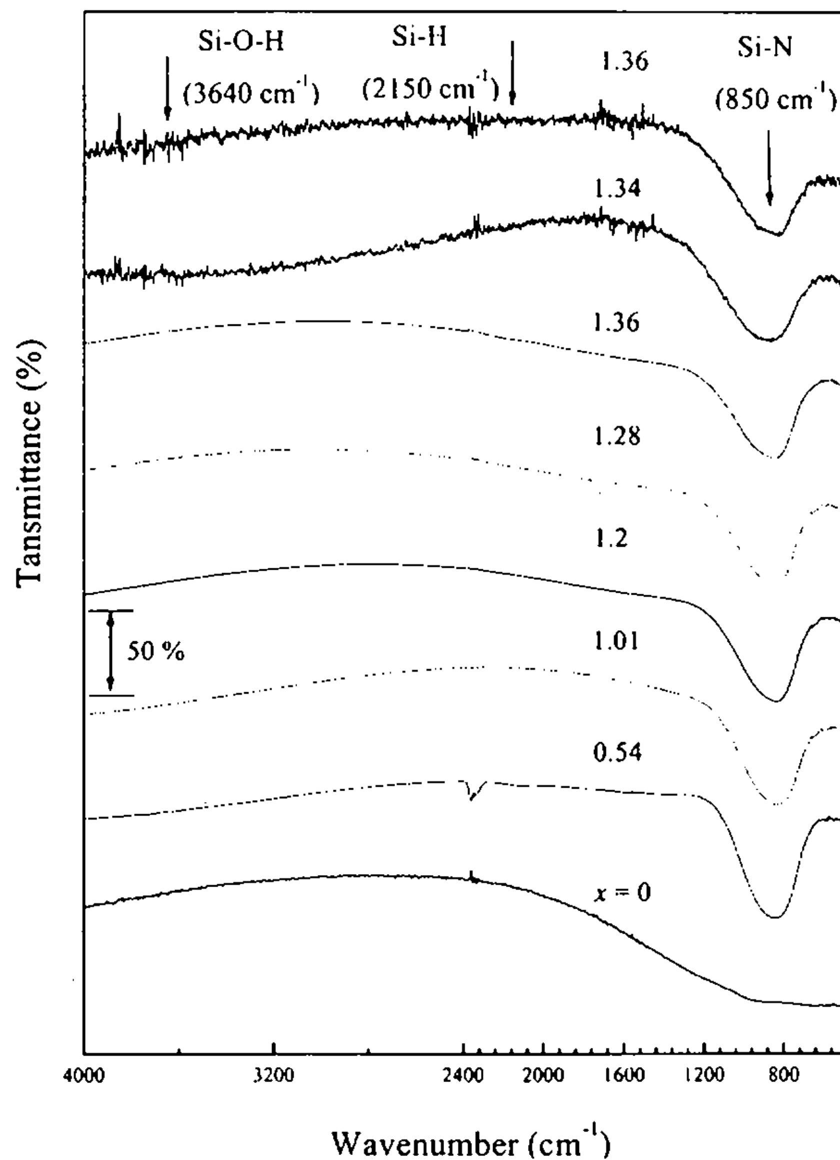

Fig. 4.7 IR absorption spectra of the DIBD SiN_x films showing the formation of Si-N bonds (850 cm^{-1}). No hydrogen and oxygen related bonds are detected.

4.5 X-ray diffraction analyses

As shown in Fig. 4.8, the XRD spectra of all the samples do not exhibit any sharp peaks, but contain broad halos. The formation of these halos is originated from the presence of tiny atomic clusters. Referring to this feature, we regard the films to be amorphous in structure, but retain the possibility that atoms can aggregate to form small clusters having short range order analogous to that in the corresponding crystalline form. The halo is so broad to cover many characteristic peaks associated with the crystalline silicon nitride phases, but the halo does not show detailed features for further deconvolution. However, the average size of the clusters can still be roughly estimated from the width of the halo.

First, for the pure Si film ($x = 0$) with no N content, two halos are observed, covering the positions of the peaks associated with the (111) planes, and (220) and (311) planes of crystalline Si, respectively [JCPDS 27-1402]. The two halos are rather broad and have an angular spread as large as 0.14 radians. These results support the conjecture that short range order of atomic arrangement is present in the films. The range retaining atomic short range order estimated from the width of the halos is in the order of 1 nm. In general, amorphous film is more suitable for the applications of electrical insulation, passivation and masking to reduce interfacial strain and give greater continuity [Hu 1966]. It should be noted that the peak at 57° was verified to come from the crystalline Si substrate. This additional peak from the Si substrate as indicated is not important in the present discussion.

Second, the XRD spectrum of the SiN_x films with x = 1.34 shows a very broad halo with 2θ ranging roughly from 15 to 48°. It covers the major x-ray diffraction peaks of crystalline α-Si_3N_4 and β-Si_3N_4 phases [JCPDS 33-1160, 41-360 and 40-1129]. The silicon nitride films are thereby regarded to be amorphous. This is understood, as the substrate temperature is too low for crystallization to occur. By substituting the wavelength λ of the x-ray beam, the width of the halo b = 0.3 radians, and the full width of half maximum θ = 27° into the Scherrer equation (3.1.3), the minimum size of atomic clusters in which short range order exists is approximately estimated to be 0.5 nm.

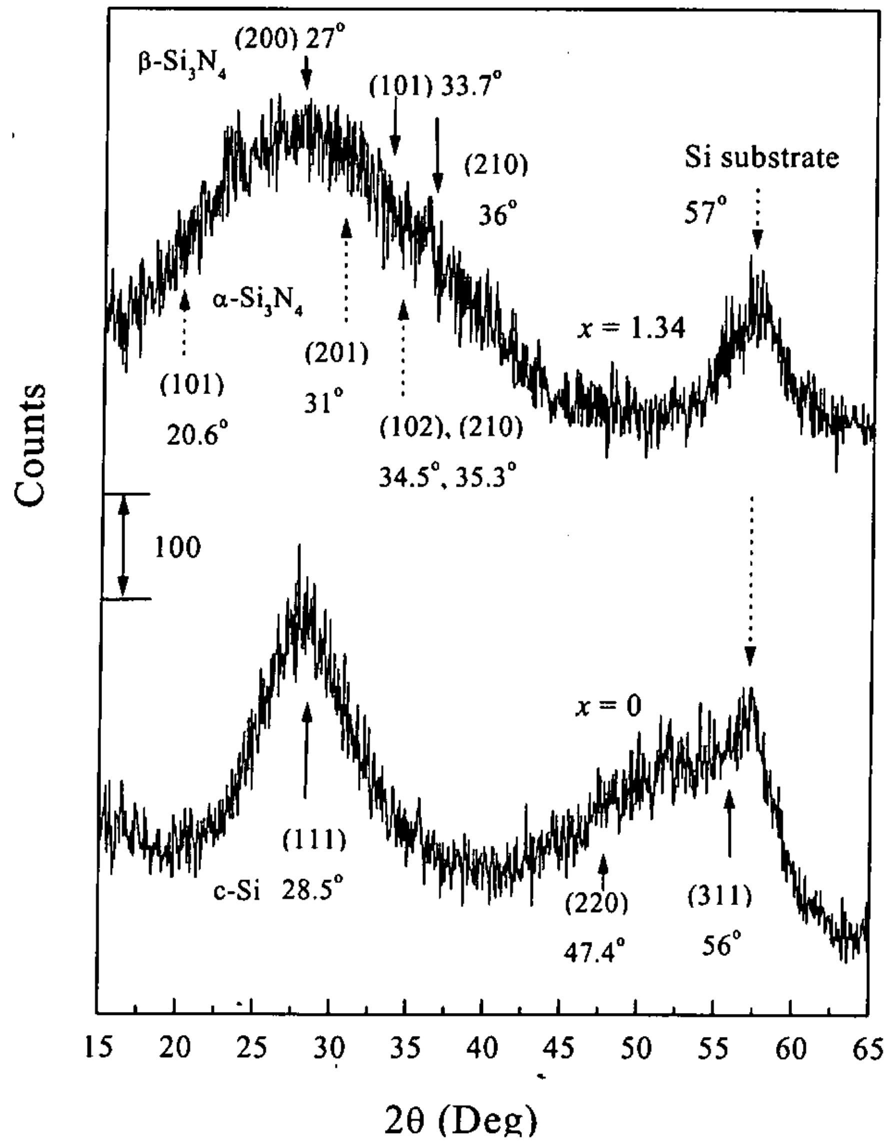

Fig. 4.8 XRD spectra of the DIBD SiN_x films with $x = 1.34$ and $x = 0$.

Chapter 5
Mechanical properties

5.1 Nanoindentation experiments

Fig. 5.1 shows the nanoindentation hardness (H) and elastic modulus (E_m) of the films as functions of x. The data is tabulated in Table 5.1. Each data point is obtained by averaging all the data acquired at similar indentation depths around 20 nm. This depth is about 1/20 of the film thickness, so that the effect from the deformation of the substrate can be neglected. The error bar shown in the figure reflects the degree of scattering of the data points and thus indicates the range of random error of the experiments. First, the values of H and E_m for the pure silicon sample of x = 0 are 12.5 and 190.5 GPa respectively. The hardness and elastic modulus rise monotonically with increasing x. When x approaches the saturated value of 1.36, H and E_m reach 20.5 and 256.0 GPa respectively, and remain almost constant.

Pao Yue-Kong Library
PolyU • Hong Kong

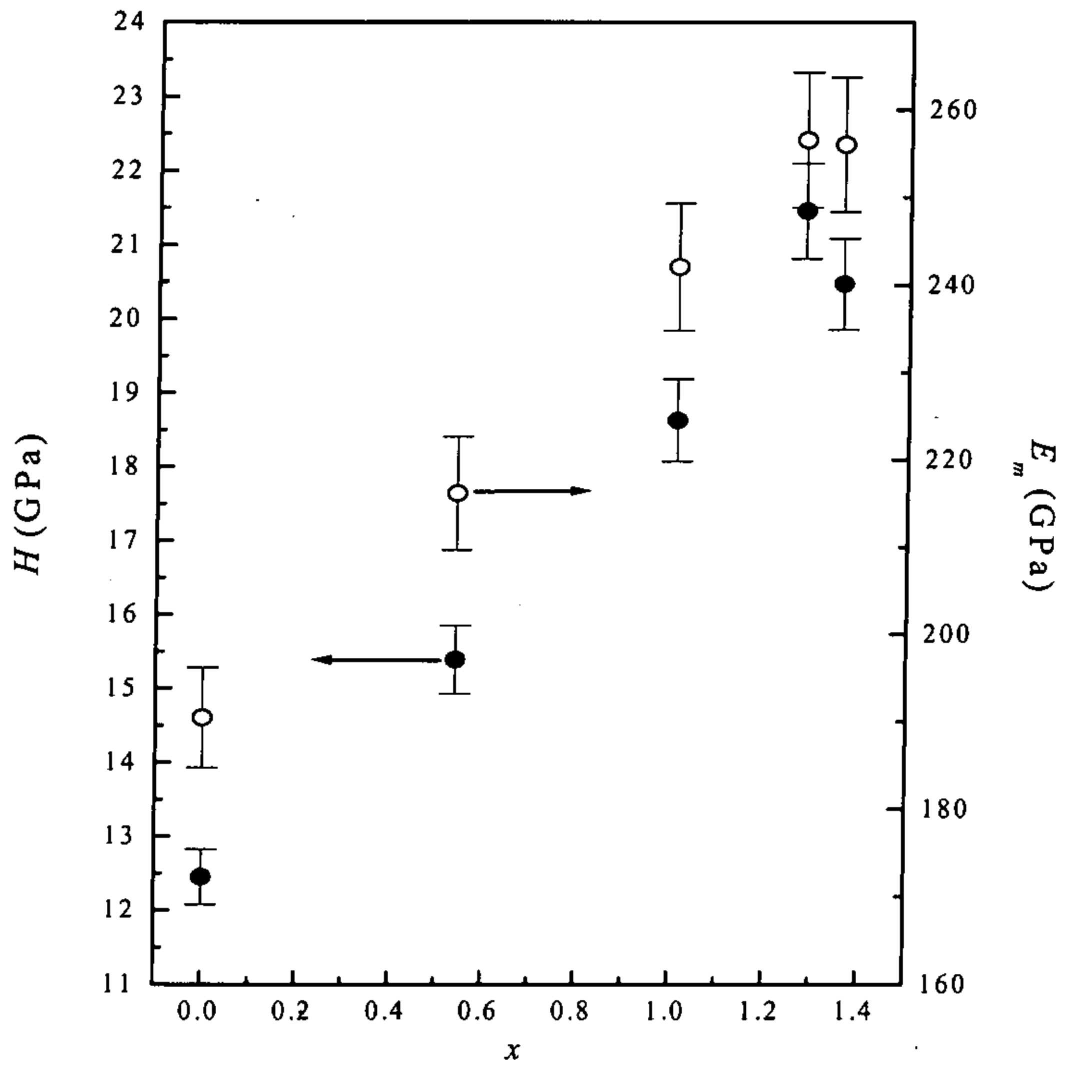

Fig. 5.1 Hardness (H) and elastic modulus (E_m) of DIBD SiN_x films as functions of x.

The hardness of these samples is approximately equal to that of stoichiometric Si_3N_4, reported to be 21 GPa [Teter 1998], and LPCVD silicon nitride films (20 GPa) deposited at high temperatures (~ 900°C) [Levy *et al.* 1996]. Furthermore, the elastic modulus at these films ($x \approx 1.36$) is very close to that of bulk Si_3N_4 (249 GPa) [Teter 1998], and is higher than those of LPCVD silicon nitride films reported by Levy (185 GPa) [Levy *et al.* 1996], Zhang (202 GPa) [Zhang *et al.* 1998], and Vlassak (222 GPa [Vlassak *et al.* 1992]). The high hardness and elastic modulus of DIBD $SiN_{1.36}$ are attributed to the ion bombardment effect. The ion bombardment imposed on the substrate by the assist ion beam causes densification of the film structure, such that the mechanical properties of DIBD SiN_x could be more superior to those of PECVD films. Moreover, the high hardness and elastic modulus of DIBD SiN_x could also be able to approach those of the crystalline Si_3N_4 phase.

Sample code	x	H (GPa)	E_m (GPa)
T117	0	12.5	109.5
T103	0.54	14.1	184.4
T106	1.01	15.4	216.3
T105	1.20	18.6	242.1
T107	1.28	21.5	256.6
T104	1.36	20.5	256.0

Table 5.1 The hardness (H) and elastic modulus (E_m) of DIBD SiN_x films with various N-to-Si ratio x values.

5.2 Friction coefficient measurement

Fig. 5.2 shows the instantaneous friction coefficient μ recorded as function of scratching distance in a ball-on-tip scratching experiment. The profile of μ rises up sharply at the beginning stage, and then shows a rather stable value within a certain range of scratching distance. Finally, the profile rises up prominently, indicating that wear of the sample becomes more severe and the corresponding influence is more pronounced. The value of μ as shown in Fig. 5.3 is actually the average results of the instantaneous values of μ recorded in the scratching range of 0.03 – 0.04 m, where the value of μ is relatively stable. The error bars show the scattering of the instantaneous values of μ. It is found that the average μ of the sample containing no N content of $x = 0$ is the highest ($\mu = 0.58$). For higher x, the average μ drops to a value of 0.38 when x is saturated at 1.36.

We also notice that the instantaneous value of μ as shown in Fig. 5.2 rises remarkably beyond a certain scratching distance, and the on-set of the rise of the profile is basically dependent on the N content in the films. For samples with high N contents, the instantaneous μ starts to rise at a shorter scratching distance. This reflects that although the N-rich films are harder and have lower average friction coefficient, but they start to be worn at a shorter scratching distance. Therefore, the wear of the N-rich samples should be particular concerned when they are used as surface protection coatings.

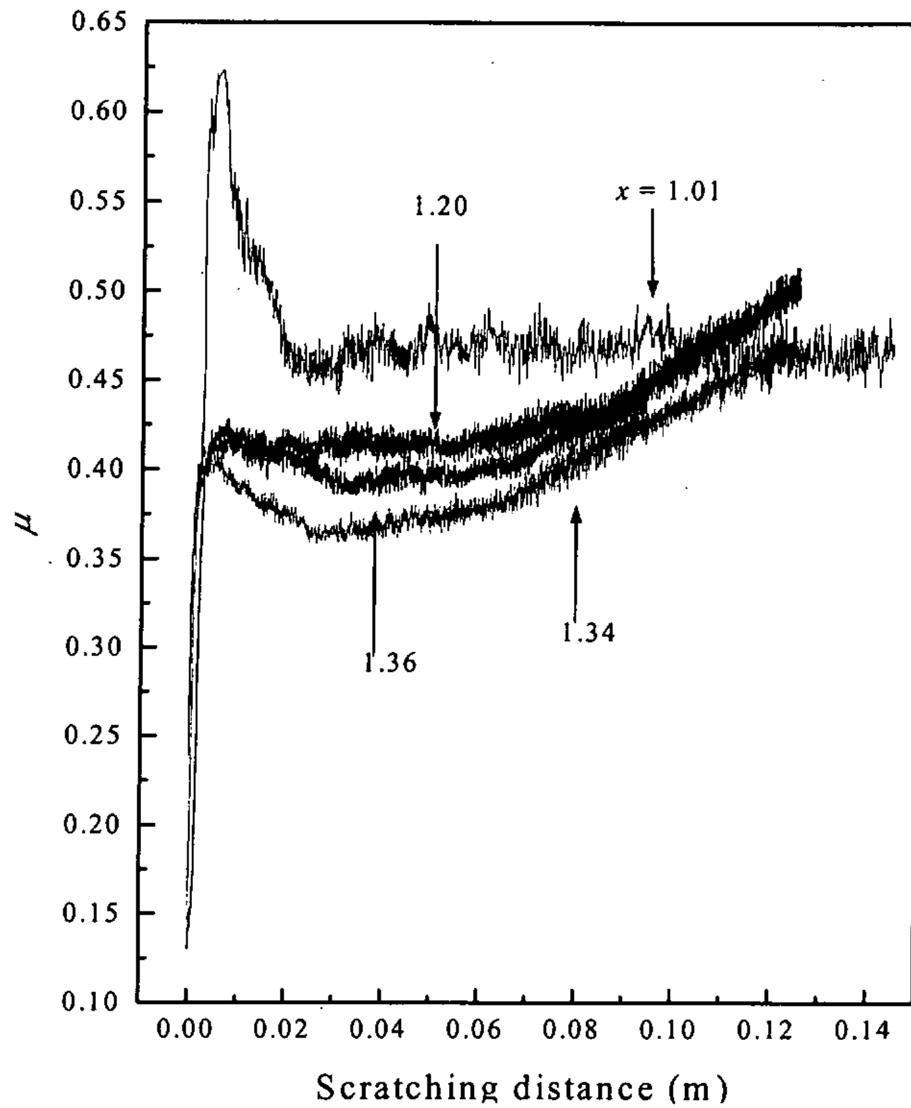

Fig. 5.2 Experimental data of friction coefficient (μ) with various x values against scratching distance.

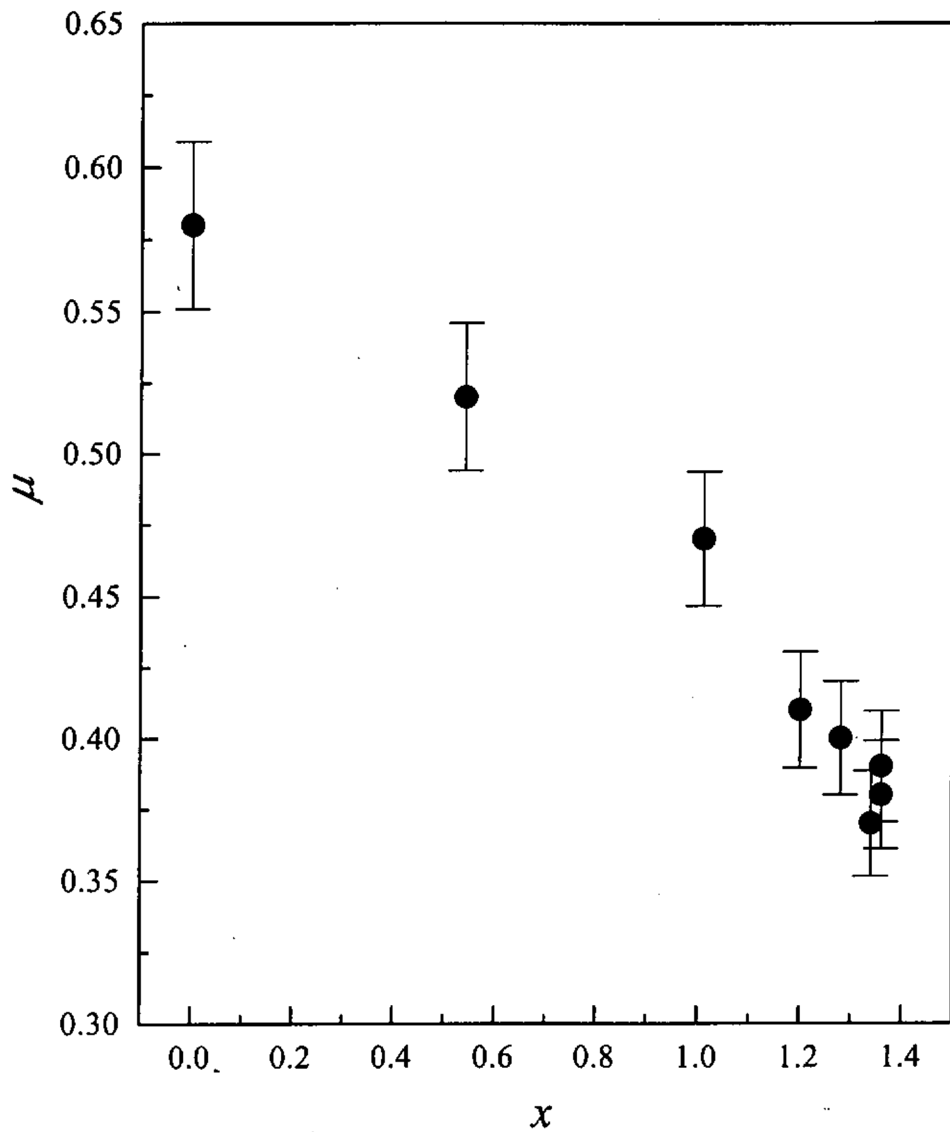

Fig. 5.3 Friction coefficient (μ) of DIBD SiN_x films as functions of x.

5.3 Stress measurement

Fig. 5.4 shows the internal stress of the films as a function of *x*. All the films are found to have compressive (negative) stress. The compressive stress σ_S in the Si film ($x = 0$) is -0.53 GPa, and σ_S rises monotonically to a high value of -1.41 GPa when *x* increases to 1.36.

The value of σ_S of the $SiN_{1.36}$ sample on Si substrate was cross-checked by using another method as proposed by Cho [Cho *et al.* 1998]. The micrograph of the cross section of the sample was taken by using a scanning electron mircoscope (SEM). The hangover of the film is clearly seen as shown in the inset of Fig. 5.4. The strain of the film is assumed to be equal to the difference between the length of the free standing hangover and that of the film when it is originally adhered to the substrate. Detailed derivation leads to an equation of:

$$\sigma_S = \frac{E_m}{(1-\nu)}\left(\frac{\pi A_o}{\lambda}\right)^2 \qquad (5.3.1)$$

where E_m is the elastic modulus (256 GPa), ν Poisson's ratio, A_o and λ are the amplitude and wavelength of the sinusoidal overhang measured from the micrograph. The value of σ_S is calculated to be 1.45 GPa, roughly consistent with 1.34 GPa determined by the optical method.

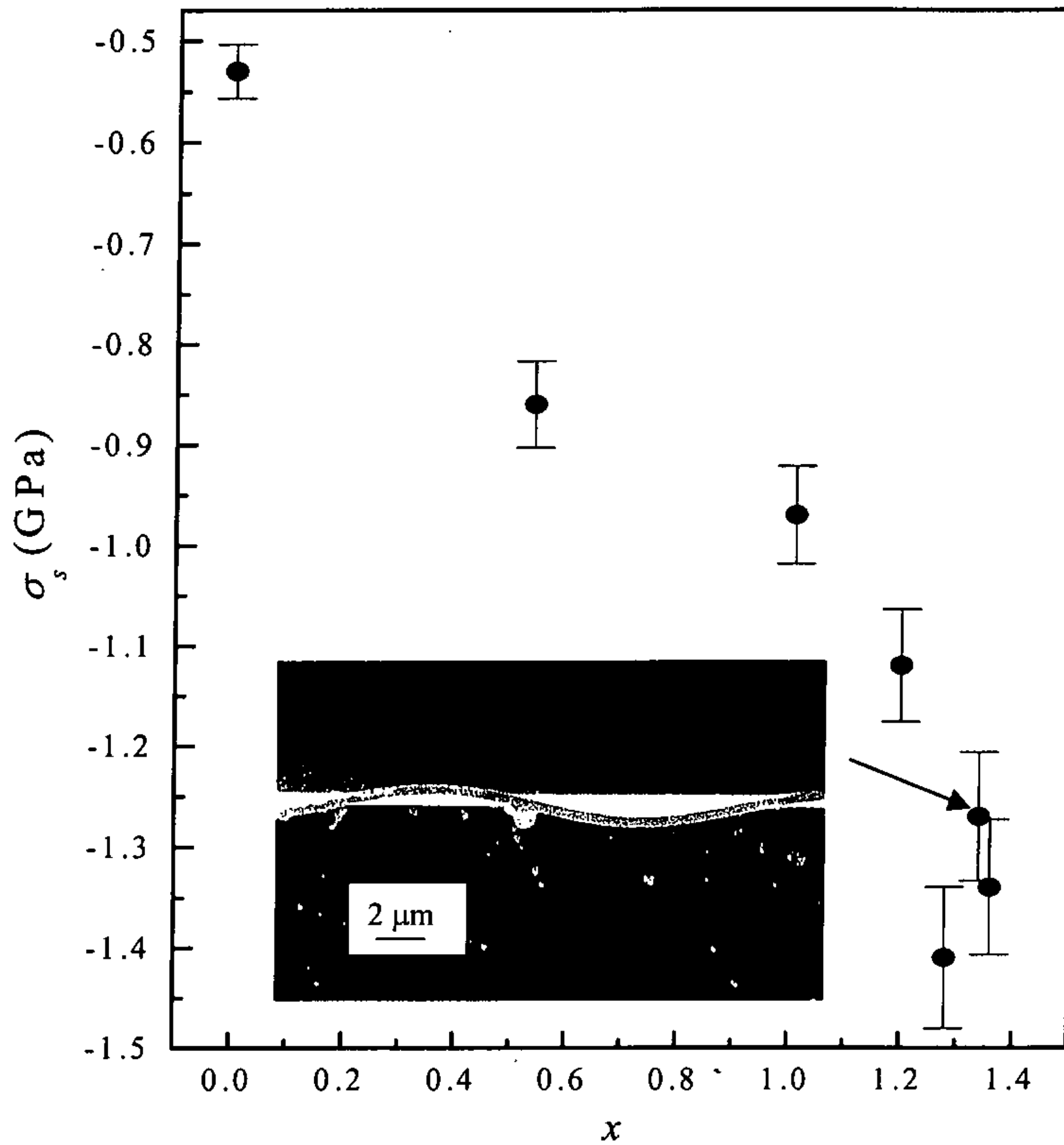

Fig.5.4 Internal stress (σ_s) of DIBD SiN_x films with various N-to-Si ratios (x).
Inset: SEM micrograph of the hangover of a $SiN_{1.34}$ sample on Si substrate.

The effects of ion assist can be revealed by comparing our data with those of silicon nitride films prepared by other techniques (Fig. 5.5). For LPCVD Si_3N_4 deposited at elevated temperatures (above 700°C), the stress in the films is usually tensile (positive). The range shown in the figure covers some typical data collected from the literature, i.e. 0.36 GPa reported by Zhang [Zhang *et al.* 1998], and 1 GPa reported by Adams [Adams[1] 1985]. LPCVD processes involve decomposition and interaction of species having thermal energies in the order of 0.1 eV. The low energy species tend to pack closely to generate dense structure with low defect density, so the internal stress is likely to be tensile.

On the other hand, the range of internal stress in plasma-enhanced chemical vapor deposited silicon nitride films covers the value of -0.4 GPa reported by Van de Ven [Van de Ven 1981], -0.2 to 0.5 GPa reported by Adams [Adams[2] 1985], -0.1 to 1.1 GPa reported by Sinha [Sinha[1,2] *et al.* 1978], extending from tensile to compressive regimes. Since the PECVD process is complicated, there are many factors, such as substrate temperature, radiation power and hydrogen content etc., which may affect the internal stress in the films. However, because of the presence of plasma, energetic particles are generated and they participate in the deposition process. For a glow discharge sustained in a plasma assisted process, we refer to the electron temperature to give a rough estimate of the energy of ions bombarding the growing film surface, which is in the order of 1 to a few tens eV [Collins 1996]. Bombarding ion cause atomic cascade collisions to displace the deposited atoms and build up tiny high pressure regions before they are completely stopped. This is well

known as the peening effect, and is the major cause for the generation of compressive stress [Sun 1986].

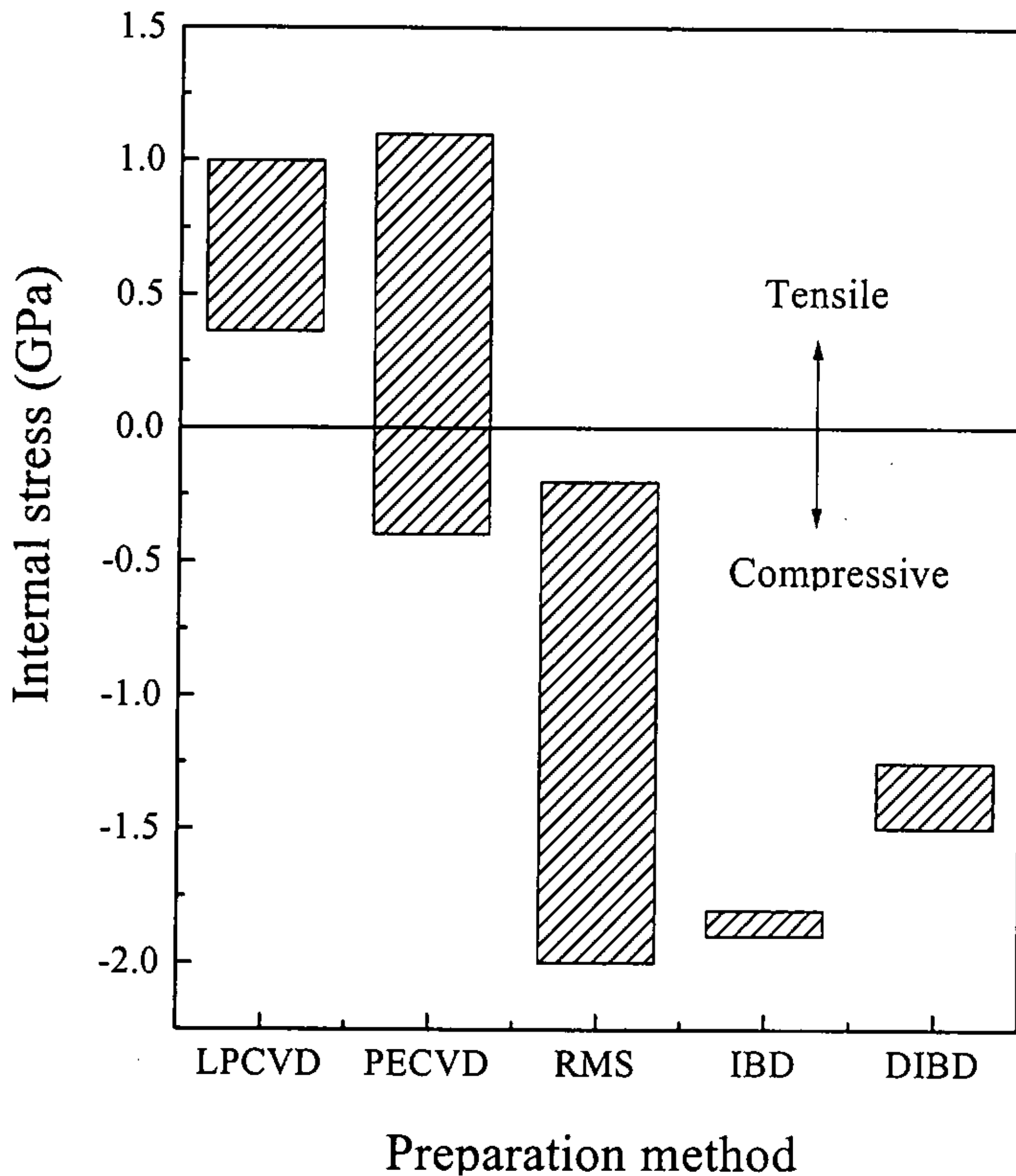

Fig. 5.5 Comparison of internal stresses measured in silicon nitride films prepared by different techniques.

LPCVD: Low pressure chemical vapor deposition

PECVD: Plasma-enhanced chemical vapor deposition

RMS: Reactive magnetron sputtering

IBD: Single ion beam deposition

DIBD: Dual ion beam deposition

For reactive magnetron sputtered (RMS) hydrogen-free silicon nitride films produced by sputtering a Si target in N_2 atmosphere, Kim and Chung [Kim and Chung 1998] reported a compressive stress of -0.2 GPa for the film deposited at no substrate bias. With increasing substrate bias to -100 V, the compressive rises consequently to reach -2.1 GPa, and remains almost unchanged for higher negative substrate bias. The sputtered species from a target have an energy of a few tens eV [Stelmack 1989], which is high enough to induce some level of peening to the growing film. Ion bombardment is enhanced when a negative substrate bias is applied. This reflects again how significant ion bombardment affects the stress in silicon nitride films.

For silicon nitride films deposited by single ion beam deposition (IBD), where the peening effect is expected to be induced by the reflected species from the target, the internal stress is -1.8 to -1.9 GPa [Huang *et al.* 1997 and Fourrier *et al.* 1991].

In DIBD, ion bombardment is directly applied by the assist ion beam. The occurrence of peening effect is expected, and compressive stress appears as observed. For our DIBD $SiN_{1.28}$ films, a maximum compressive stress of -1.41 GPa is detected, which is close to the value (-1.5 GPa) reported by Windishmann [Windishmann 1987]. Most significantly, this comparison illustrates the feasibility of controlling the magnitude and state (tensile or compressive) of the internal stress in silicon nitride by bombarding the growing film with ions of different energies.

Chapter 6
Etching properties

The chemical etching rates of the DIBD SiN_x films in buffered hydrofluoric acid (BHF) and potassium hydroxide (KOH) were measured respectively. The composition of the BHF solution was given in Appendix A.1. The wet chemical etching was carried out at ambient temperature. Photoresist and Cr/Au layers (refer to Section 2.4) severed as mask. The KOH etchant had a concentration of 43 wt% and was kept at 80 °C throughout the etching. In addition, RIE was performed to characterize the DIBD and LPCVD nitride thin films undergoing dry etching.

6.1 Wet etch

The wet chemical etch rates of DIBD SiN_x are plotted as function of N-to-Si ratio (x) in Fig. 6.1. When using BHF as an etchant, the etching rate of the DIBD amorphous silicon film ($x = 0$) is negligibly slow, as in the case of crystalline Si. With increasing the N content, the etch rate rises considerably to around 7 nm min^{-1} when $x \geq 1$. Comparing the etching rate of SiN_x thin film prepared by various techniques, low pressure chemical vapor deposited (LPCVD) Si_3N_4 has the lowest etching rate < 1 nm min^{-1} [Adams[2] 1985]. This is because LPCVD Si_3N_4 has a dense structure with a low concentration of defects. Moreover, the content of oxygen and hydrogen impurity is also low. On the contrary, DIBD SiN_x thin films intrinsically contain a certain amount of ion-induced defects and oxygen impurity (≈ 6 at.%). As a

consequence, the etching rate of DIBD SiN_x in BHF is higher than that of LPCVD Si_3N_4.

However, the etching rate of DIBD SiN_x in BHF ($\approx$ 7 nm min^{-1}) is comparable with that of plasma-enhanced chemical vapor deposited (PECVD) silicon nitride with hydrogen content below 20 at.% ($\approx$ 10 nm min^{-1}) [Gupta 1991]. On the other hand, the BHF can effectively etch away PECVD silicon nitride films with higher hydrogen contents (e.g. 40 at.%) at a rate of 100 nm min^{-1}. The etching rate of hydrogen-free silicon nitride prepared by magnetron sputtering with no substrate bias in BHF is reported very high (110 nm min^{-1}) [Kim *et al.* and Jansen *et al.*]. Introduction of substrate bias densifies the film structure considerably, resulting in a drastic drop of etching rate to 3.8 – 20 nm min^{-1}, roughly the same order of magnitude as that of our DIBD SiN_x.

When KOH (at 80 °C) is used as the etchant, the etching rate for all the samples is negligibly low at all compositions of the films. In particular, the etching rate of the silicon film is surprisingly low compared to that of (100) single crystal Si, which is known to have a fast etching rate of 1.44 μm min^{-1} in KOH [Köhler 1999]. The high etching resistance of DIBD amorphous Si film in KOH is not understood. We suppose that a passivation layer may be formed on the surface of the Si film during the etching process which stops further removal of the film material. This is the same mechanism giving rise to a very low etching rate of metal glass in acid or alkali compared to its crystalline phase.

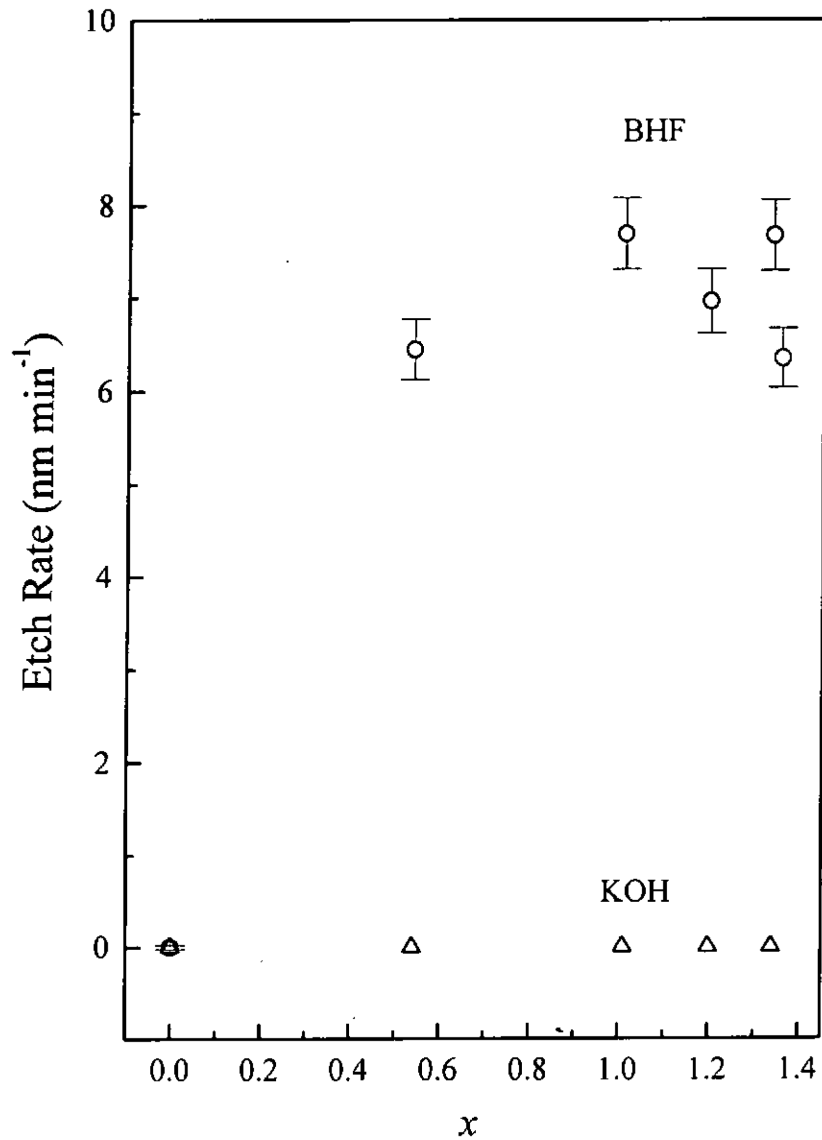

Fig. 6.1 Etching rate of the DIBD SiN_x films in BHF and KOH solutions as a function of x.

6.2 Dry etch

The etching rate of both the DIBD SiN_x and LPCVD Si_3N_4 samples by using reactive ion etching (RIE) was also measured. The etching process was conducted in an RIE chamber using plasma of CHF_3 gas. The etching rates of both types of nitride films were found to be 25 μm min^{-1}. Besides, etching rate of AZ-3100 photoresist was also determined to be 22 μm min^{-1}. Therefore, the etching selectivity of silicon nitride (DIBD or LPCVD) and photoresist is about 1:1.

All these results are very useful for evaluating the applicability of the SiN_x films in many areas of applications, such as the use of the materials in microelectromechanical devices. By using the above data, microbridges of LPCVD silicon nitride with length and width of 460 μm and 20 μm were fabricated. The result of nanoindentation on these microbridge samples will be presented separately in Appendix.

Chapter 7
Optical and electrical properties

The DIBD SiN_x contained a lot of defects due to energetic ion bombardment induced by assist beam during deposition. A high density mid-gap is expected to be formed. Starting from analyzing the optical absorption spectrum, the information on the density of electron states (DOS) can be extracted. The knowledge of DOS can then be used for interpreting the results of some electrical property measurements, such that the transport mechanism of charge carriers can be revealed. In this chapter, a new methodology for unified numerical analysis of the optical absorption and electrical conductivity for amorphous dielectrics or semiconductors having high density of mid-gap states is proposed. It was applied to our DIBD SiN_x films. Result give interesting implications on the transport mechanisms of the film material.

7.1 Analysis of optical absorption and determination of DOS

Tauc plots of the optical absorption data of SiN_x films were shown in Fig. 7.1. In principle, for an amorphous semiconductor having low defect states, $(h\nu\alpha)^{1/2}$ is $\propto (h\nu - E_{opt})$. However, the curves are not quite linearly even at high $h\nu$, leading one to infer that the defect states in DIBD SiN_x films are dense, such that in quite a large portion of $h\nu$ range under observation (particularly at low $h\nu$), electron transitions involving localized states give remarkable contribution to optical absorption. The first estimate of E_{opt} ranges from 1.5 to 3.5 eV, which increases progressively with increasing assist N_2^+ beam current. This result is expected

because the band gap of stoichiometric Si_3N_4 is known to be higher than that of crystalline silicon.

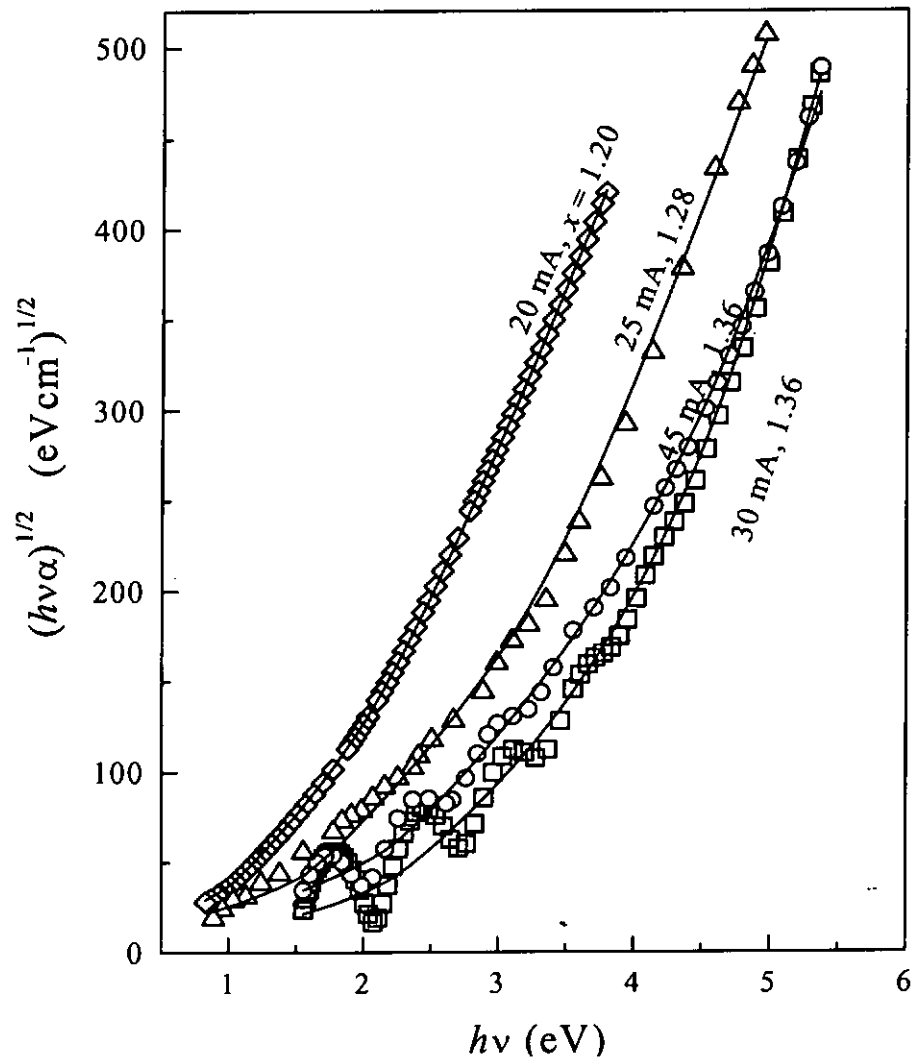

Fig. 7.1 Optical absorption spectra of DIBD SiN_x films with various x. Fitting curves derived from the theory described in the text are shown.

Next, we fitted the optical absorption data with the aid of the proposed DOS functions as follows [Ong *et al.* 2001]. The general feature of the proposed band model is demonstrated schematically in Fig. 7.2. The energy level E_v of a certain state in the valence band is set to be 0. The DOS function below E_v is represented by a parabolic curve :

$$N_v(E) = A\,(-E + \varepsilon_o)^{1/2}, \qquad \text{when } E \leq 0 \qquad (7.1.1)$$

where A and ε_o are two parameters. We refer this to be the "valence" band, but in the model the wavefunctions of electrons in this band are not necessarily to be extended. Similarly, above E_c (= E_{opt} + $2\varepsilon_o$), there is "conduction" band which is also describable with another parabolic function :

$$N_c(E) = A\,(E - E_{opt} - \varepsilon_o)^{1/2}, \qquad \text{when } E \geq E_{opt} + 2\varepsilon_o \qquad (7.1.2)$$

The presence of localized states in the mid-gap is described by two exponential tails extending from E_v and E_c towards the gap center, respectively :

$$N_{vt}(E) = A\,\varepsilon_o^{1/2}\exp(-E/E_o), \qquad \text{and} \qquad (7.1.3)$$

$$N_{ct}(E) = A\,\varepsilon_o^{1/2}\exp[(E - E_{opt} - 2\varepsilon_o)/E_o], \qquad (7.1.4)$$

where E_o indicates the width of the tails. The dashed curves shown in Fig. 7.2 represent the imaginary extensions of the valence and conduction bands. The separation between the intercepts of the two dashed curves on the E-axis defines the optical band gap E_{opt}. The function form of (7.1.1) to (7.1.4) ensures the continuity of DOS at $E = E_v = 0$, and $E_c = E_{opt} + 2\varepsilon_o$.

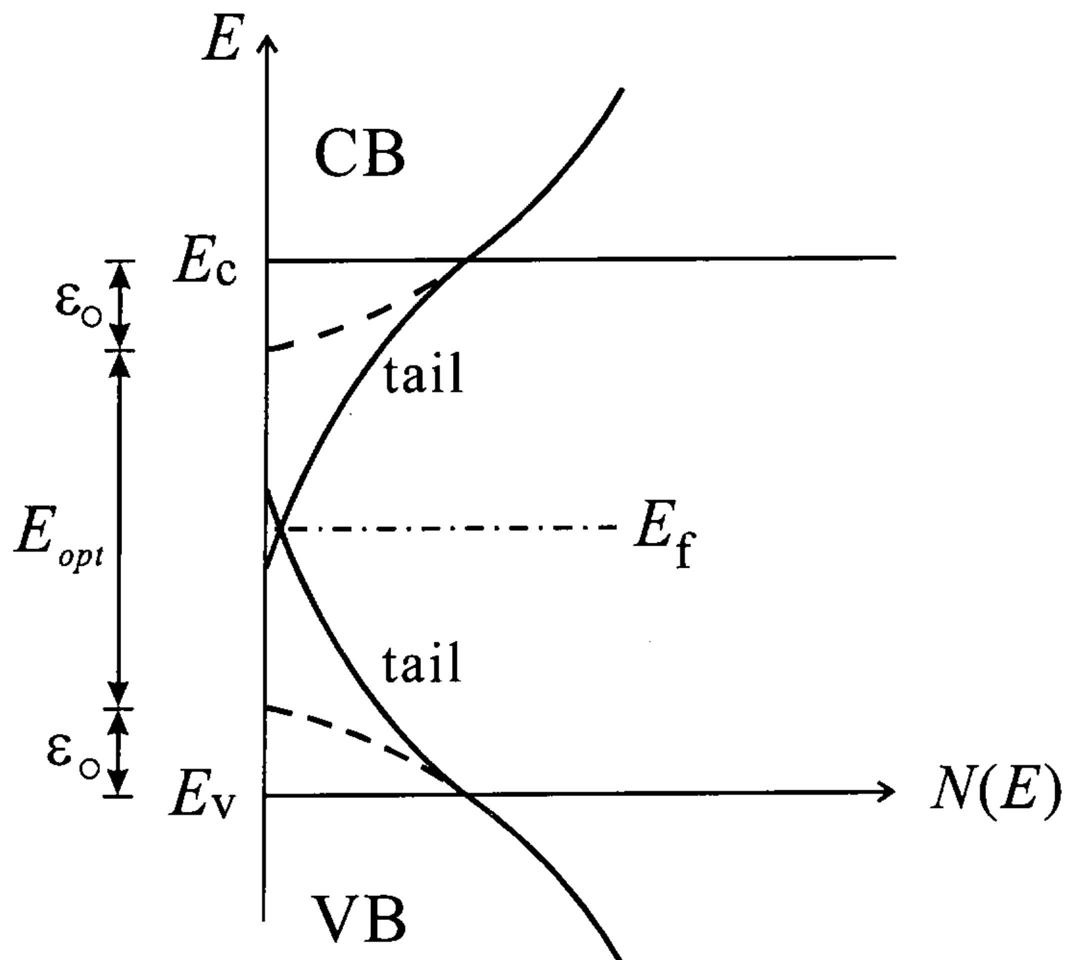

Fig. 7.2 DOS model used for analyzing the optical absorption spectra of the DIBD SiN_x films.

It is generally believed that electron transition between two localized states via absorption of a photon is difficult to happen because of the weak spatial overlapping of their wavefunctions [Curtins and Favre 1988]. However, we find from the results of fitting that this kind of transitions must be included in order to get good fits to the optical absorption spectra, or otherwise the calculated absorption spectrum would drop steeply in the region of $h\nu < E_f$. Our assumption is reasonable if we refer to the example that in tungsten oxide an electron can be excited by an incident photon to transit from one W^V atom to an adjacent W^{VI} atom which are all localized in space. This is the fundamental mechanism of the well known electrochromic effect [Monk *et al.* 1995].

With these considerations, nine types of electron transitions are allowed as listed in Table 7.1 where the symbols VB and CB denote the valence and conduction bands, respectively. Electron transitions can be divided into three classes. The first class only includes transitions from an occupied VB state to an empty CB state. The second class includes four types of transitions from an occupied VB state to an empty (VB or CB) tail state, or from an occupied (VB or CB) tail state to an empty CB state. The third class exhausts the four possible types of transitions between two localized states.

Initial (occupied)	Final (empty)	Lower limit, ($h\nu \geq E_{opt}+2\varepsilon_0$)	Upper limit ($h\nu \geq E_{opt}+2\varepsilon_0$)	Lower limit, ($h\nu < E_{opt}+2\varepsilon_0$)	Upper limit ($h\nu < E_{opt}+2\varepsilon_0$)
VB	CB	$2\varepsilon_0 + E_{opt} - h\nu$	0	-------------------	
VB VB	VB tail CB tail	$-h\nu$	$E_{opt} + 2\varepsilon_0 - h\nu$	$-h\nu$	0
VB tail CB tail	CB CB	0	$E_{opt} + 2\varepsilon_0$	$E_{opt} + 2\varepsilon_0 - h\nu$	$E_{opt} + 2\varepsilon_0$
VB tail VB tail CB tail CB tail	CB tail VB tail CB tail VB tail	-------------------		0	$E_{opt} + 2\varepsilon_0 - h\nu$

Table 7.1 Nine possible electron transitions associated with absorption of photons and the corresponding integration limits in Eq. (7.1.5).

Every type of electron transition contributes to the overall optical absorption at a certain $h\nu$ by a term α_i [Jackson *et al.* 1982, Payson *et al.* 1985 and Vanecek *et al.* 1984]:

$$\alpha_i = \frac{\beta}{h\nu} \int_{\text{Lower limit}}^{\text{Upper limit}} N_{\text{initial}}(E)\, N_{\text{final}}(E + h\nu)\, f(E)[1 - f(E + h\nu)]\, dE \,. \qquad (7.1.5)$$

N_{initial} and N_{final} are the DOS at the energy levels of the initial state and final state separated by the incident photon energy $h\nu$. The Fermi-Dirac distribution function $f(E)$ and $[1 - f(E+h\nu)]$ at a certain temperature T are introduced to ensure

that the initial and final states are occupied and empty, respectively. The overall optical absorption coefficient is the sum of all these terms :

$$\alpha = \sum_i \alpha_i , \tag{7.1.6}$$

where i goes through all types of transitions.

According to the theory of Mott and Davis, electron transitions between two extended states, and between an extended state and a localized state have the same β [Mott[1] and Davis 1971]. We further assume that β of the transitions between two localized states included in the present analysis also has the same value. Mott and Davis deduced the expression of $\beta = 8\pi^4 e^2 \hbar^3 d/(m^2 cn)$, where e and m are the charge and mass of an electron, c is the speed of light, n the refractive index, and d the average lattice spacing defined as the cubic root of the volume occupied by a single atom. n was taken to be the refractive index of Si_3N_4 (= 2.6) [Van de Ven 1981], and d is better approximated by the nearest neighbor distance in the crystalline Si_3N_4 structure (= 0.179 nm) [Pierson 1996]. With these setting, β is calculated to be 2.27×10^{-38} eV^2 cm^5.

The settings of "Lower limit" and "Upper limit" in equation (7.1.5) in the range of $h\nu \geq E_{opt}+2\varepsilon_o$ and $< E_{opt}+2\varepsilon_o$ are listed in Table 7.1. In particular, a photon of $h\nu \geq E_{opt}+2\varepsilon_o$ is able to excite transitions of type 1 to 5, while those between two mid-gap states are excluded. On the other hand, a photon of $h\nu < E_{opt}+2\varepsilon_o$ is not high enough to excite any VB-to-CB transition, while those of other types are possible.

Furthermore, in this model we assume that the Fermi level is approximately lying at the middle between E_v and E_c, or equivalently at $E = E_{opt}/2 + \varepsilon_o$.

Numerical integration described by equation (7.1.5) was carried out iteratively by using Mathcad (Version : 8 Professional, MathSoft Corp.) through continuous adjustment of the four fitting parameters, A, E_{opt}, ε_o and E_o, until a best fit of minimum error was achieved. The curves derived are plotted in Fig. 7.1 to demonstrate how satisfactory the curves match with the experimental data.

From the optimized fitting parameters summarized in Table 7.2, one can make the following conclusions. The optical band gap E_{opt} increases from 1.8 to 4.2 eV with increasing N content. This trend is reasonable, as E_{opt} is far below the band gap of crystalline silicon (1.11 eV) and moves towards that of silicon nitride of 4-5 eV (for plasma enhanced chemical vapor deposition) and 5 eV (for low pressure chemical vapor deposition) [Sze 1983]. Next, ε_o only varies mildly in the range of 0.05 to 0.07 eV. Third, the tail E_o has a generally trend to increase with increasing N content, except that of the film deposited at 30 mA (x = 1.36) is slightly lower than those deposited at higher or lower assist beam current. It is found that the density of states of this film at E_f (Table 7.2), $N(E_f) = A\ \varepsilon_o^{1/2}\ \{\exp(-E_f/E_o) + \exp[(E_f - E_{opt} - 2\varepsilon_o)/E_o]\}$, is also the lowest ($5.57 \times 10^{20}$ eV^{-1} cm^{-3}). The increase in assist beam current above 30 mA (e.g. 45 mA) does not lead to the increase in N content, but results in denser localized gap states owing to more severe in-situ ion bombardment during growth.

I_a (mA)	x	A ($eV^{-3/2}$ cm^{-3})	E_{opt} (eV)	ε_o (eV)	E_o (eV)	E_f (eV)	$N(E_f)$ (eV^{-1} cm^{-3})
20	1.20	2.04×10^{21}	1.80	0.050	0.53	0.95	1.52×10^{20}
25	1.28	2.32×10^{21}	2.94	0.045	0.75	1.52	1.31×10^{20}
30	1.36	3.40×10^{21}	4.20	0.055	0.65	2.16	5.57×10^{19}
45	1.36	2.90×10^{21}	4.10	0.070	0.82	2.12	1.16×10^{20}

Table 7.2 Summary of the values of A, E_{opt}, ε_o and E_o assigned to the DOS functions for getting good fits to the optical absorption spectra of SiN_x films with various N contents. I_a is the assist N_2^+ ion beam current used for bombarding the substrate.

7.2 Analysis of electrical conductivity and transport mechanisms

Fig. 7.3 shows the plots of logarithm of electrical conductivity (σ_c) against the reciprocal of temperature (1000/T). The first estimate of the thermal activation energy E_a roughly calculated from the slope of the curves is seven to ten times lower than E_{opt}. This could happen if the mid-gap density is so high (10^{19} - 10^{20} eV^{-1} cm^{-3} as observed for our films), such that the transport processes are mainly controlled by those carriers hopping through localized states centering around the middle of the gap. The activation energy extracted represents in a larger extent the average height of the potential barrier to be overcome for one hop, rather than the energy at the bottom of the conduction band measured from the Fermi level as in an ordinary crystalline semiconductor. We also notice that σ_c of the film deposited at 30 mA N_2^+ ion assist current (x = 1.36) is the lowest at any temperature, consistent with the lowest density of gap states, for example at E_f extracted from optical absorption. Further increase of assist beam current to 40 mA results in the rise in σ_c at all temperatures, because more defect states are introduced.

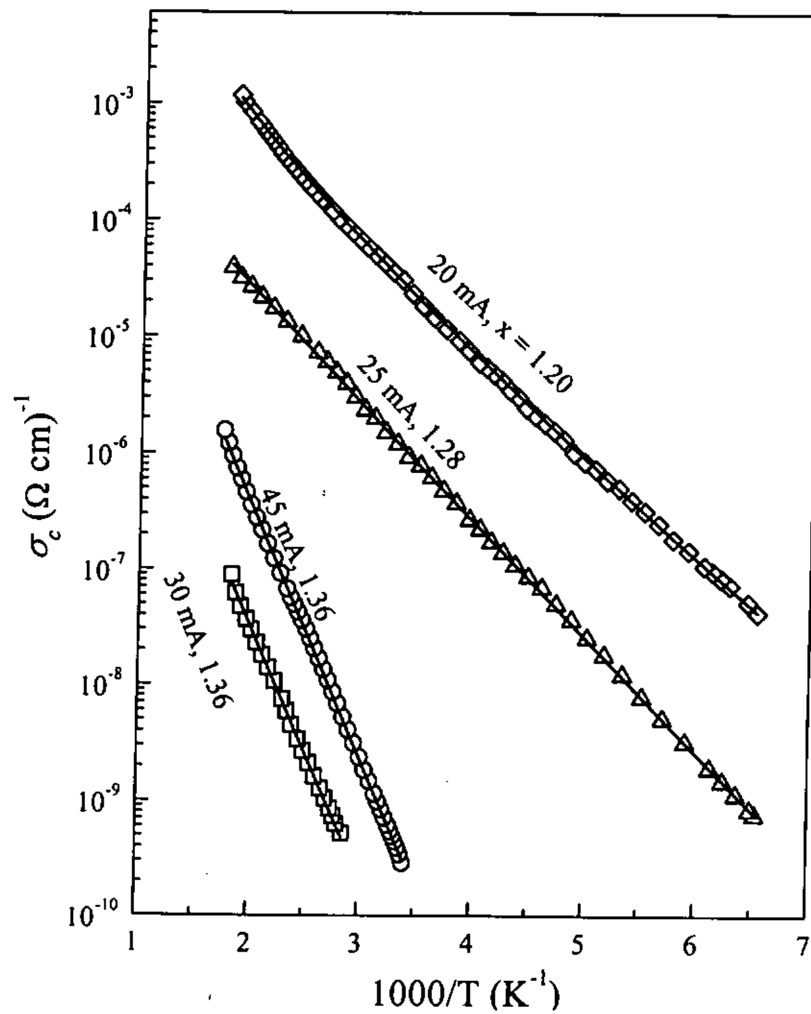

Fig. 7.3 Temperature dependence of electrical conductivity (σ_c) of DIBD SiN_x films with various x. Fitting curves derived from the theory described in the text are shown.

Two kinds of hopping processes through localized states around the Fermi level of amorphous semiconductors are proposed. For the first one, a charge carrier moves to the nearest neighboring state with the aid of lattice vibration (phonons). The second one happens more likely at lower temperatures, where a charge carrier can tunnel to a distance farther than the nearest states (variable range hopping) [Nagels 1979]. However, in these models, simplification is made by assuming that the concentration of charge carriers participating in conduction is $N(E_f)\ k_BT$, such that the detailed influence from the function form of DOS and other possible energy dependence of important transport parameters, e.g. drift mobility, would not be reflected. Theoretical plot of log σ_c v.s. 1000/T plot from the former, and the plot of log ($\sigma_c T^{1/2}$) v.s. $1/T^{1/4}$ from the latter are intrinsically straightly lines, generally not detailed enough for fitting experimental data. One example is that the plot of σ_c v.s. 1000/T of the film deposi ed at 20 mA assist is curved in the whole observed temperature range.

We therefore employ a set of more fundamental formulations for investigating the electrical conductivity data. Only hopping to nearest states is considered. For a certain group of electron having energy of E under the influence of an applied electric field $\vec{F}$, the effective hopping frequency ν at temperature T along the direction of $\vec{F}$ is :

$$\nu = \nu_{ph} \exp(-2\rho R)\ [\exp(-\frac{E_a - eRF}{k_B T}) - \exp(-\frac{E_a + eRF}{k_B T})], \quad (7.2.1)$$

where ν_{ph} is the phonon frequency assumed to be 10^{13} Hz, and k_B the Boltzman factor. 1/ρ is the spread of the localized electron wavefunction. The wavefunction

contains a factor like exp(-ρ*r*), where *r* is the radial distance from the center. In the present model, E_a, *R* and ρ are implicitly assumed to be functions of *E*. If *eRF* is sufficiently small compared with k_BT, ν is approximated by :

$$\nu = 2\nu_{ph}\,\frac{eRF}{k_BT}\,\exp(-2\rho R)\,\exp(-\frac{E_a}{k_BT}). \qquad (7.2.2)$$

The drift velocity of this group of charge carriers is $u = \nu R = \mu F$, where μ is the corresponding drift mobility and is thereby a function of *E* also :

$$\mu(E) = 2\nu_{ph}\,\frac{eR^2}{k_BT}\,\exp(-2\rho R)\,\exp(-\frac{E_a}{k_BT}). \qquad (7.2.3)$$

The electrical conductivity as a function of temperature $\sigma_c(T)$ can thus be written as:

$$\sigma_c(T)=$$

$$\int_{E_{lower}}^{E_{upper}} \frac{2\nu_{ph}e^2 R(E)^2}{k_BT}\exp[-2\rho(E)R(E)]\,\exp[-\frac{E_a(E)}{k_BT}]\,N(E)\,f(E)[1-f(E)]\,dE \qquad (7.2.4)$$

The integration limits E_{lower} and E_{upper} are 0 and $E_{opt} + 2\varepsilon_o$, respectively. According to Mott and Davis [Mott[2] and Davis 1971], E_a is a function of *E*. E_a is the highest at $E = E_f$, and then drops when *E* approaches E_v or E_c. We assigned a linear function form to $E_a(E)$ by :

$$E_a(E) = E_a(E_f)\,(1 - \frac{|E-E_f|}{E_f}). \qquad (7.2.5)$$

Due to the symmetric feature of the DOS functions defined, $E_a(0) = E_a(E_{opt} + 2\varepsilon_o)$.

In addition, the spread of the wavefunction is also assumed to increase with increasing E from E_f in a linear manner :

$$\frac{1}{\rho(E)} = \frac{1}{\rho(E_f)} + \delta(|E - E_f|) \text{ (nm)} \quad (7.2.6)$$

This assumption indicates that the electrons at E_f have highest degree of localization, and become more and more "delocalized" when approaching the conduction and valence bands. Again, because of the symmetry of the DOS functions, $1/\rho(0) = 1/\rho(E_{opt}+2\varepsilon_o)$.

We further assumed that the hopping distance of charge carrier at E close to E_v and E_c is effectively the size of the electron wavefunctions at those energy levels. At these stages, the wavefunction is large enough to cover a region containing many states. This feature is presented mathematically by assigning $R(E)$ to be:

$$R(E) = R(E_f) + \frac{|E - E_f|}{E_f}\left[\frac{1}{\rho(0)} - R(E_f)\right]. \quad (7.2.7)$$

With this function form, the hopping distance rises linearly with increasing energy separation $|E - E_f|$. Furthermore, $R(0)$ and $R(E_{opt}+2\varepsilon_o) \rightarrow 1/\rho(0) = 1/\rho(E_{opt}+2\varepsilon_o)$. $R(E_f)$ in the formula, i.e. the hopping distance at E_f, is defined by the relationship :

$$N(E_f)\, E_a(E_f)\, 4\pi R(E_f)^3/3 = 1, \quad (7.2.8)$$

stating that the electron has just found one state to hop. Equivalently :

$$R(E_f) = \left[\frac{3}{4\pi E_a(E_f) N(E_f)}\right]^{1/3}. \quad (7.2.9)$$

The integration in equation (7.2.4) was carried out iteratively with the three parameters, i.e. $E_a(E_f)$, $1/\rho(E_f)$ and δ, being adjusted until the best fits of the plot of log σ_c v.s. 1000/T curves were achieved. $N(E)$ was substituted by the DOS functions obtained from the optical absorption analysis. The values of the parameters for getting the best fits are summarized in Table 7.3. The change of $E_a(E_f)$, $1/\rho(E_f)$ and δ has the effect of varying the slope, overall level and curvature of a curve respectively, such that the data behaviour can be reproduced. Fig. 7.3 shows how good the theoretically derived curves match with the data.

I_a (mA)	x	E_a (eV)	$1/\rho(E_f)$ (nm)	δ (nm eV^{-1})	$R(E_f)$ (nm)	$R(E_v) = R(E_c) = 1/\rho(E_v) = 1/\rho(E_c)$ (nm)
20	1.20	0.15	0.45	1.57	2.188	1.947
25	1.28	0.195	0.45	0	2.109	0.45
30	1.36	0.41	0.412	0	2.158	0.412
45	1.36	0.43	0.444	0	1.687	0.444

Table 7.3 Summary of the values of E_a, $1/\rho(E_f)$ and δ in Eq. (7.2.4) for good fits to the optical absorption spectra of SiN_x films with various N contents. The calculated hopping distances R at Fermi level E_f and E_v (or E_c) are given.

The following conclusions are drawn. First, the activation energy at E_f increases with increasing N content (Table 7.3), probably because a larger x would result in a more highly random atomic network, in which the potential barrier separating two adjacent sites is higher.

Second, the spread of the electron wavefunction at E_f [$= 1/\rho(E_f)$] almost does not change with the N content, but lies in a narrow range of 0.412 – 0.45 nm. For the film deposited at an assist beam current of 20 mA, δ was set at 1.57 in order to generate the curvature of the log σ_c - 1000/T plot in Fig. 7.3. This means that the spread of the wavefunction becomes larger with increasing E. For other films containing more N, δ was set to be 0, meaning that the spread of the wavefunction does not depend on E.

Third, the hopping distance of the charge carriers around E_f is determined by the separation between two localized states around E_f. Such a distance is larger than the spread of the wavefunctions for all the film samples. However, for the charge carriers with energy near E_v or E_c, the spread of the wavefunction could be large enough to cover a volume containing more than one state, so that the hopping distance is more reasonably to be substituted by the spread of the wavefunction itself (Table 7.3).

From equation (7.2.3), the drift mobility μ at any temperature or energy E can be derived theoretically. Fig. 7.4 and Fig. 7.5 shows two curves of interest. One presents the temperature dependence of μ for the charge carriers near E_f. Results show that μ is rather strongly thermally activated. The value, even for the film deposited at 20 mA (x = 1.28) N_2^+ ion assist, is still below 10^{-4} cm^2 V^{-1} s^{-1}. Next, μ is plotted as a function of energy measured from the Fermi level ($|E - E_f|$) at a temperature of 300 K. The dependence of μ on $|E - E_f|$ is considerably strong.

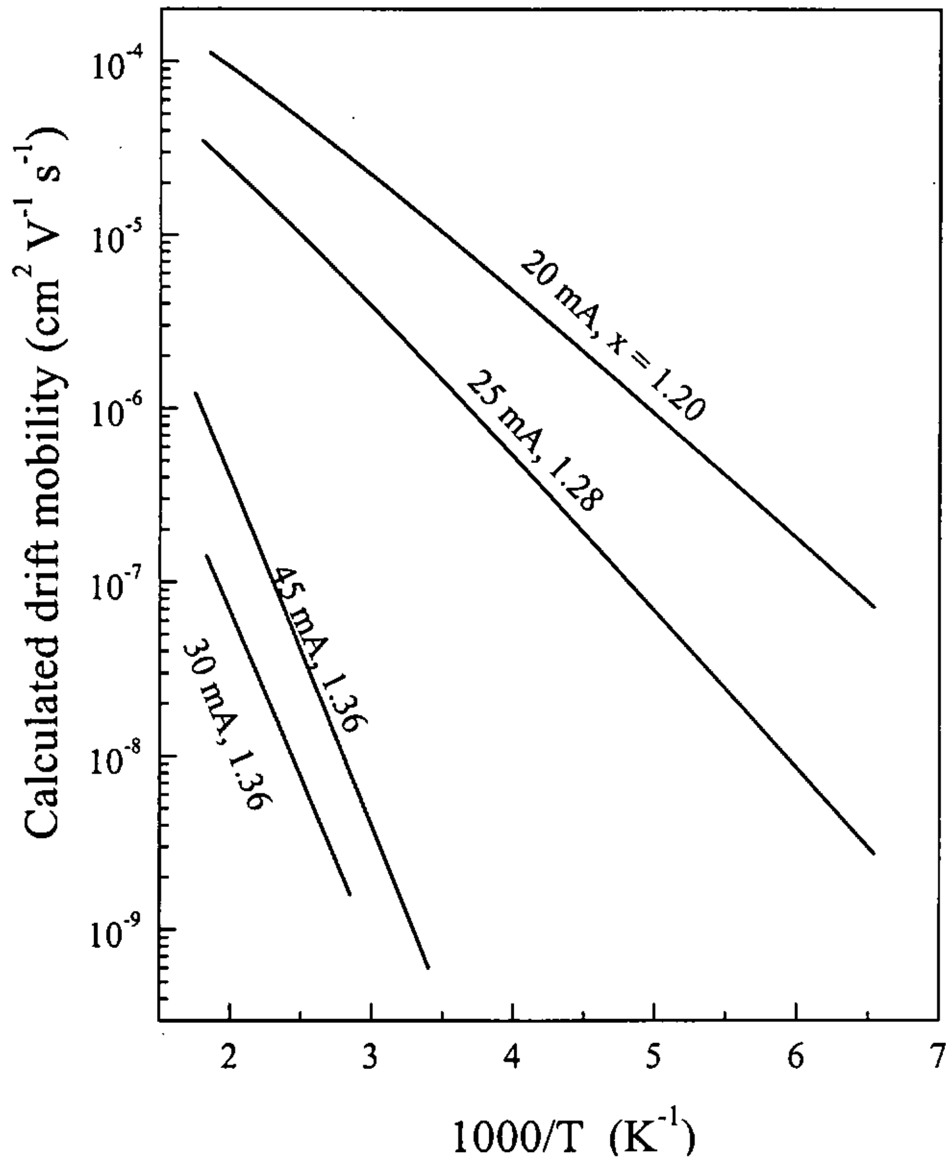

Fig. 7.4 Plots of theoretically derived drift mobility of charge carriers at E_f against the reciprocal of temperature.

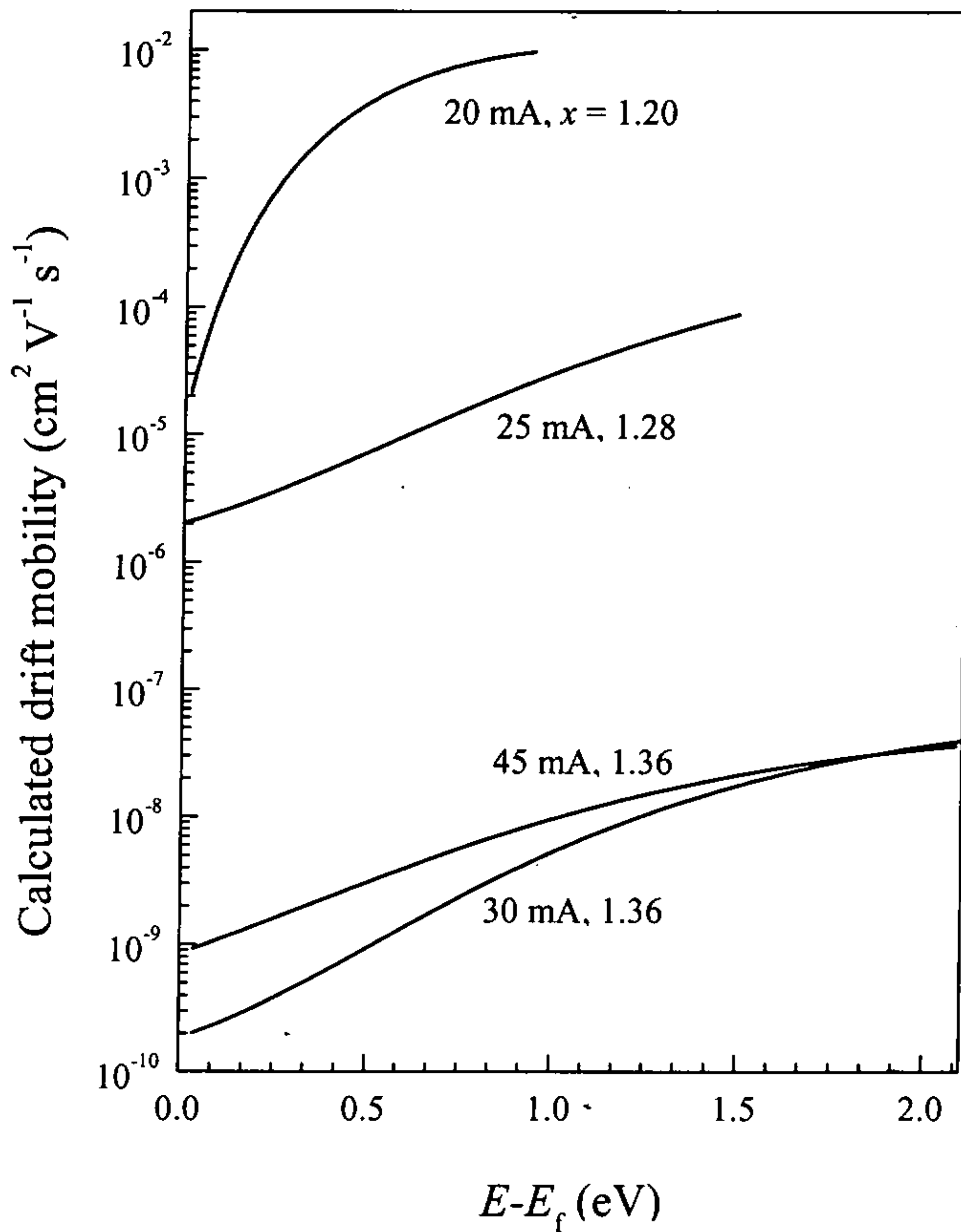

Fig. 7.5 Plots of theoretically derived drift mobility of charge carriers at 300K against energy measured from the Fermi level ($E - E_f$).

Chapter 8
Conclusions

A series of silicon nitride (SiN_x) films with various N contents were successfully deposited by DIBD. The film thickness was carefully controlled and fell within range of 387 to 489 nm. The coating rate was found to be 13 – 16 nm min^{-1}, which was almost independent of the assist beam current. At higher assist N_2^+ ion beam current, higher incorporation level of N into the films was obtained. The N-to-Si ratio, defined as x, rises approximately linearly with assist N_2^+ beam current until the beam current reaches 30 mA. At N_2^+ beam current above 30 mA, x saturates at a level of 1.36. The saturated value is close to that of stoichiometric Si_3N_4, indicating that at this atomic ratio, the structure is more energetically stable.

The formation of Si-N bonds with successive N incorporation is verified by the growth of a peak in the XPS profile at 102 eV associated with Si-N bonds, and the concomitant disappearance of a Si 2p photoelectron peak at 100.3 eV associated with Si-Si bonds. Although, the SiN_x films contain some oxygen (~ 6 at.%), the oxygen atoms bond to the atomic network in a relatively stable manner. Moreover, an IR absorption band with a peak position at 850 cm^{-1} becomes observable even when a small amount of N is added. The band is attributable to the asymmetric stretching vibrational mode of Si-N bonds. No hydrogen related bonds were detected, such that the DIBD SiN_x films were hydrogen free. It is known that the presence of hydrogen in silicon nitride would affect it chemical inertness, therefore, our SiN_x samples have rather satisfactory chemical resistance. The etching rate is as low as 7 nm min^{-1}

against BHF and is negligibly small against KOH. The RIE etching rate is around 25 nm min^{-1}.

No characteristic X-ray peaks but only broad halos were observed in the XRD spectra. Film structure with short range order analogous to that in crystalline Si_3N_4 structure is maintained. Our samples are therefore classified as amorphous. From the width of the halo, the size of atom clusters in which short range order is maintained can be estimated. This dimension is estimated to be 1.2 nm for the Si film, and 0.5 nm for the $SiN_{1.34}$ film.

For the Si films, the hardness and elastic modulus are 12.5 and 190.5 GPa, respectively, which are the lowest among all of the samples. When the N content increases, both the hardness and elastic modulus increase correspondingly, and finally reach the values of 21.5 and 256.6 GPa at x = 1.36. These values are comparable to those of crystalline Si_3N_4, reported to be 21 and 249 GPa, respectively. The friction coefficient drops from 0.58 dramatically as N content increases, and finally reaches at a level of 0.38 when x = 1.36.

All the SiN_x samples appear to have compressive stress (negative). The magnitude of the compressive stress increases from 0.53 GPa for x = 0 (Si) to a maximum value of 1.41 GPa when x reaches to 1.28. It then drops slightly as N content increases further. The compressive stress is originated from the ion bombardment by the assist ion beam on the growing film surface. When ions intrude into the deposits, they induce cascade atomic collisions, and displace the deposited

atoms. Consequently, tiny high pressure regions are formed and compressive stress is thus established. Comparing with silicon nitride prepared by other techniques, it is found that the degree of particle bombardment on the growing surface has significant influence on the stress in silicon nitride formed. LPCVD silicon nitride, on the other hand, has tensile stress as it is formed by species with low thermal energy. PECVD silicon nitride has compressive stress, as it is formed under higher degree of particle bombardment. Silicon nitride formed by sputtering or ion sputtering process has similar compressive stress, as it is formed under the influence of most energetic species.

We have also fabricated some microbridges of CVD silicon nitrides for nanoindentation tests. Since DIBD silicon nitride has compressive stress, the indentation data would not be easily interpreted. Therefore, in this experiment, we used LPCVD silicon nitride instead. Load was applied until the microbridge sample was broken. Residual stress and elastic modulus of CVD silicon nitride films were extracted by numerical fittings to the data.

The optical band gap E_{opt} of SiN_x increases from 1.8 to 4.2 when x increases from 1.2 to 1.36. Activation energy E_a (0.16 – 0.43 eV) of electrical conductivity is much lower than E_{opt}, indicating that hopping mechanism dominates the transport phenomena of the films. This is because the DIBD SiN_x films are formed under ion bombardment, therefore they contain rather high density of ion induced defects. These defects could be small in size but induce dense mid-gap states. A model has been established to give numerical fitting to the optical absorption spectra and

temperature dependence of electrical conductivity simultaneously. This model is applicable to amorphous dielectric and semiconductors having high density of mid-gap states. With this model, the functions of density of states were derived and the drift mobility as a function of temperature and electron energy was predicted.

Though there are seldom papers to report the applicability of DIBD silicon nitride films in electronic devices, from this study, DIBD silicon nitride is found to have many excellent properties. We expect that the quality of the DIBD silicon nitride film can be further improved by rising the substrate temperature. Consequently, the DIBD films become comparable to those of CVD silicon nitride. The problems of CVD silicon nitride caused by hydrogen incorporation are therefore eliminated. Further investigations should be carried out to see whether the compressive stress in DIBD SiN_x could be released by post-annealing process.

Appendix
Test on silicon nitride microbridges

Nanoindentation tests were done on CVD silicon nitride microbridges to determine the elastic modulus (E_m) and residual stress (σ_r) of the LPCVD silicon nitride films. These parameters were extracted by theoretical fitting to the experimental data of load-displacement against load applied at the center of the microbridge. Once both of elastic modulus and residual stress are determined, the bending strength (σ_{bs}) of the microbridge can also be calculated. CVD silicon nitride films were used because they were under tensile stress and the mathematical model was simpler, while DIBD silicon nitride films were under compressive stress and were therefore not suitable for demonstrating this methodology.

A.1 Fabrication of silicon nitride microbridges

Microbridges of low pressure chemical vapor deposited (LPCVD) silicon nitride were fabricated for nanoindentation experiments to obtain the load-displacement relationship of these free standing structures. A 0.4 μm thick LPCVD Si_3N_4 was deposited on both sides of (100) p-doped Si wafer (resistivity of 4 – 7 Ω-cm), which was originally grown with a 5 μm thick thermal silicon dioxide (SiO_2) layer.

Fig. A.1 illustrates the flow chart of the processes for fabricating the LPCVD Si_3N_4 microbridges. First of all, a chromium (Cr) and a gold (Au) layers were deposited on both sides of the nitride chip by magnetron sputtering. These two-layered structure serves as a metal mask to protect Si_3N_4 in bridge region from being attacked by RIE and BHF (Step 1).

Etch windows were delineated on back side of the Cr/Au layer by conventional photolithography whereas the front side was covered by a layer of thick AZ-3100 photoresist. The exposed Cr/Au windows on the back side was then removed, and subsequently followed by BHF etching which removed the exposed Si_3N_4 and SiO_2 (Step 2). The etchants used for removing different layers are shown in Table A.1.

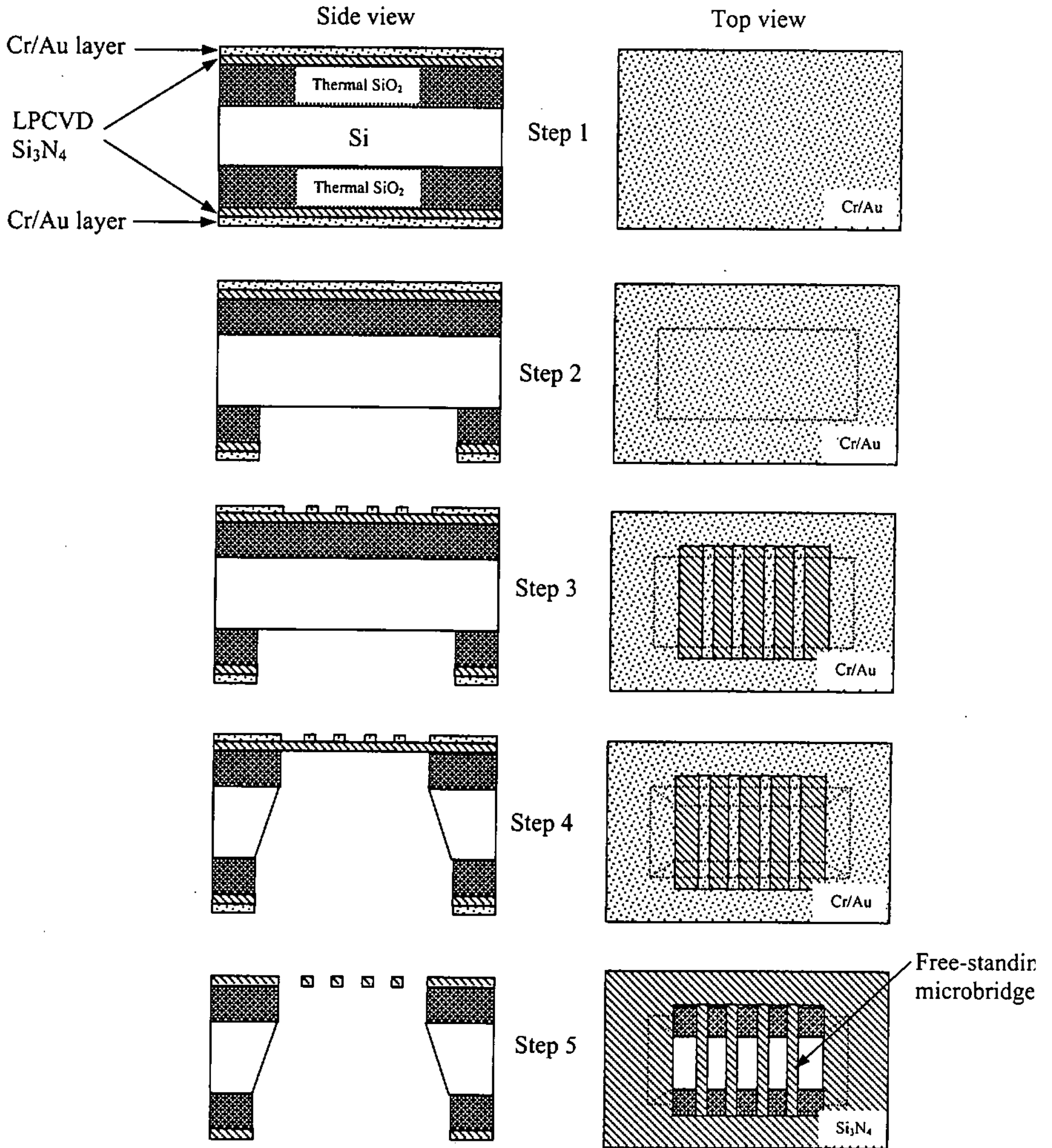

Fig. A.1 Flow chart for microbridge fabrication.
Step 1 Deposition Cr/Au protective layers. Step 2 Open back side etch window.
Step 3 Microbridges patterning on Cr/Au layer. Step 4 Back side etch of Si and SiO_2 layers. Step 5 RIE etching of Si_3N_4 and microbridge pattern is obtained after removing Cr/Au layer.

Patterns of microbridges were defined on the top Cr/Au layer by photolithography and by wet etching to remove the exposed Cr/Au layer (Step 3). Next, the bared silicon at the back side was etched away in KOH solution at 80°C to form a free standing membrane of Si_3N_4 on SiO_2. The residual SiO_2 layer was removed by BHF (Step 4). The sample now had a Si_3N_4 membrane and a Cr/Au layer patterned of microbridges on top. The exposed Si_3N_4 was then removed by RIE. Free standing nitride microbridges were obtained once the Cr/Au layer was wet etched completely (Step 5).

Etchant	Formula	Materials	Remark
43 wt.% KOH	75.4g KOH + 100ml H_2O	Si	80°C
BHF	20ml 40% NH_4F + 10ml 25 % HF + 10ml H_2O	SiO_2 Si_3N_4	Room temp
Au etch	4g KI + 1g I_2 + 80ml H_2O	Au	Room temp
Cr etch	200g $Ce(NH_4)_2(NO_3)_6$ + 35ml CH_3COOH 98% + 1000ml H_2O	Cr	Room temp

Table A.1 Etchants for removing Si wafer, Si_3N_4, SiO_2, Au and Cr layers.

A.2 Load-displacement test on LPCVD Si_3N_4 microbridges

Nanoindentation experiments were done on LPCVD silicon nitride microbridges to find out the load-displacement curves. Instead of using a Berkorich 3-sided tip, a wedge probe with an edge width of 30 μm was used to apply load at the middle of the microbridges. The process is considered to be one dimensional. The width of the wedge tip is larger than the width of the microbridges (20 μm). The load was continuously added until the microbridge was broken. Fig. A.2 is a schematic depiction of a microbrigde test, where the microbridge is made from a silicon nitride thin film by photolithography and etching processes. The (100) Si substrate material under the microbridge was removed by etching.

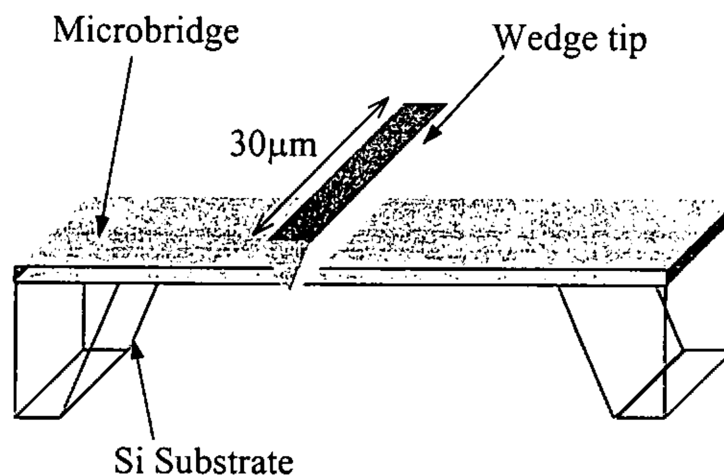

Fig. A.2 Load-displacement test on a microbridge sample.

A.3 Load-displacement tests on LPCVD Si_3N_4 microbridges

Samples for the load-displacement tests were prepared by photolithography technique. Fig. A.3 is the micrograph showing the array of microbridges sample before tests. The microbridges have a thickness t_b = 0.4 μm, width b_w and length l_b as listed in Table A.2. All these dimensions were measured before the tests.

Continuously increasing load was applied to the centre of a bridge by a wedge tip having a width of 30 μm. Fig. A.4 shows the load-displacement curve of sample S1 (b_w = 20 μm and l_b = 480 μm) before fracture. The loading and unloading curves coincided completely. To the maximum displacement of 20 μm, the deformation of the microbridge is thereby completely elastic. This shows the typical characteristic of ceramics.

Sample	t_b (μm)	b_w (μm)	l_b (μm)
S1	0.4	20	480
S2	0.4	20	460

Table A.2 Dimensions of the LPCVD silicon nitride microbridge samples.

For microbridge sample S2, load was applied until fracture occurred. The result of sample S2 is shown in Fig. A.4. The bridge is broken when the load reaches 1.5 mN and the corresponding deflection of the centre point is about 20 μm.

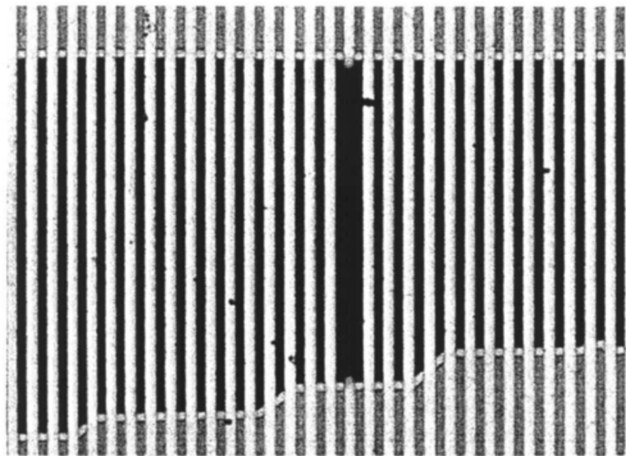

Fig. A.3 Micrograph of LPCVD silicon nitride microbridges for samples of S1 and S2 (100X).

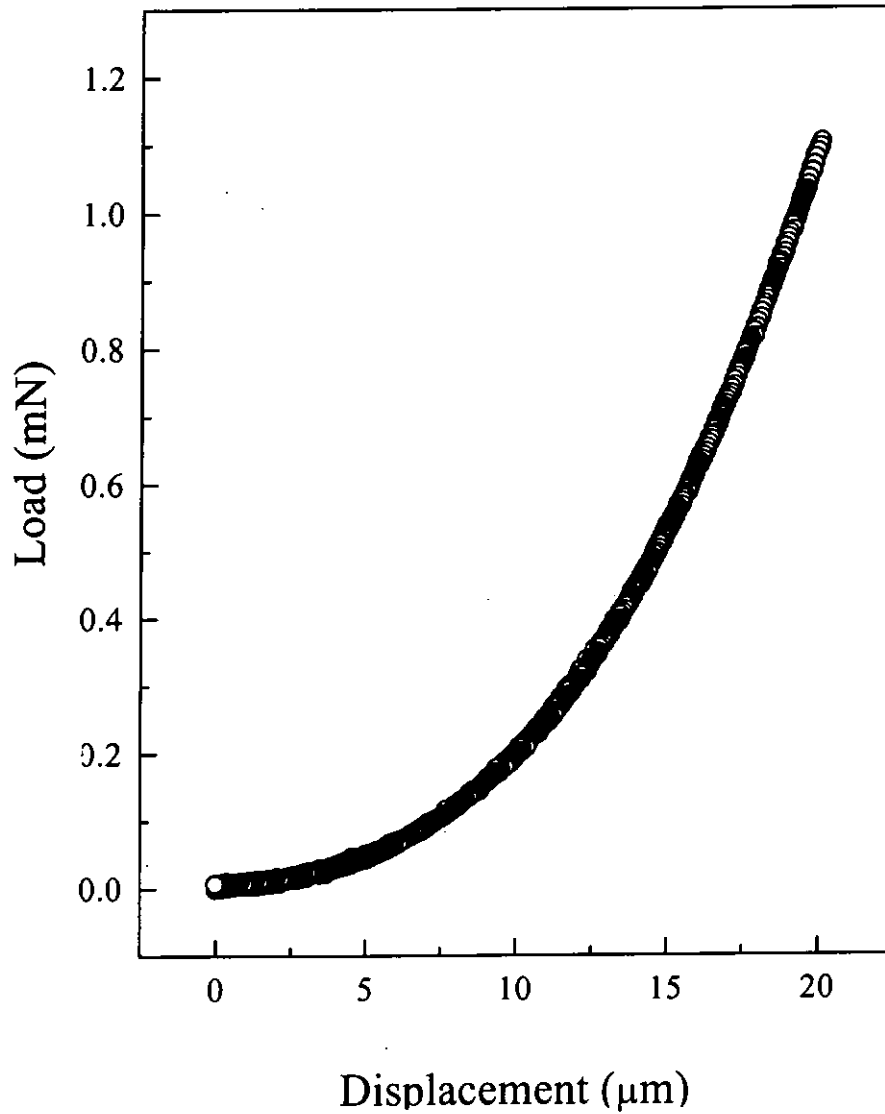

Fig. A.4 The load-unload curve of the LPCVD silicon nitride microbridge S1 before fracture occurs. Thickness t_b= 0.4 μm, width b_w = 20 μm and length l_b = 480 μm.

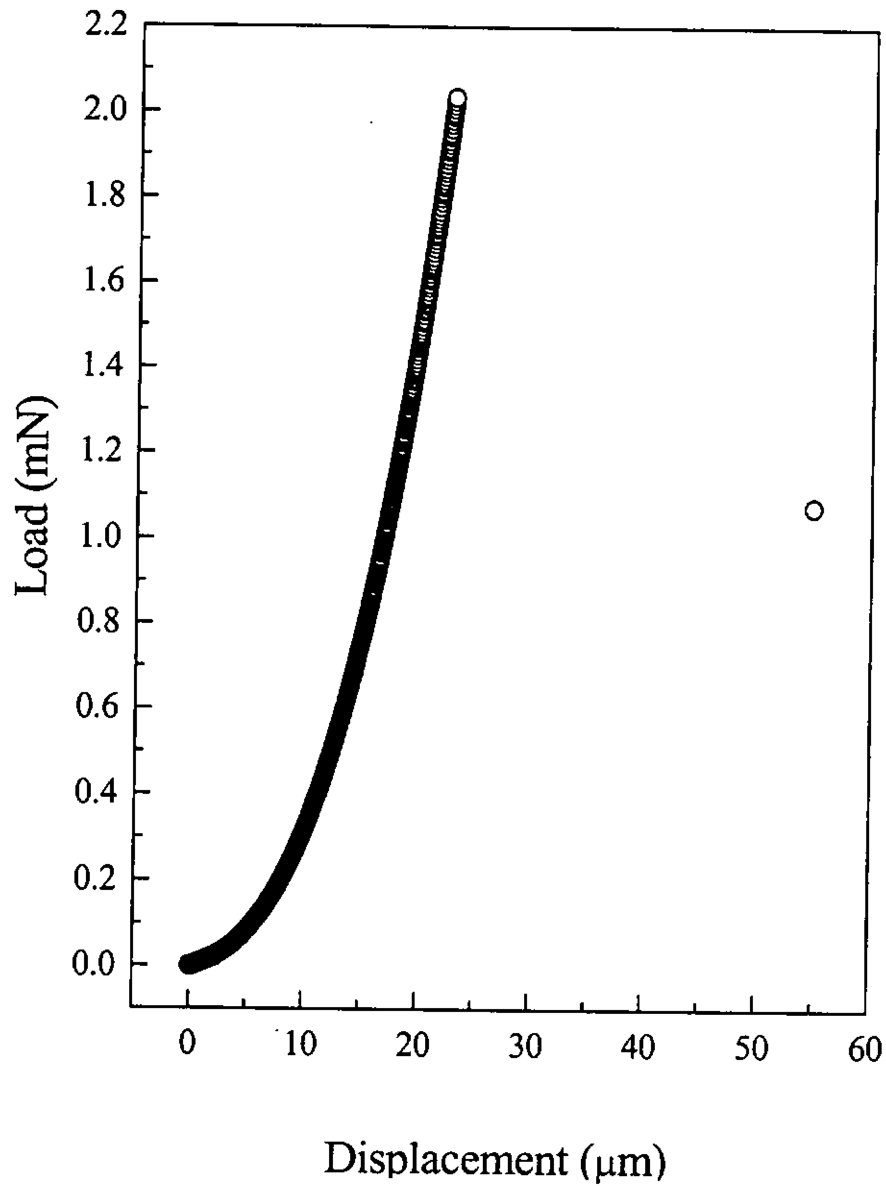

Fig. A.5 Load-displacement curve of microbridge S2 recorded until fracture occurs. Thickness t_b = 0.4 μm, width b_w = 20 μm and length l_b = 460 μm.

A.4 Theoretical analysis of load-displacement curve

To analyzes the load-displacement relationship, we applied the boundary conditions of simply supported ends as illustrated schematically in Fig. A.6 where the substrate deformation was neglected and no bending moment was generated to the microbridge by the substrate at both ends.

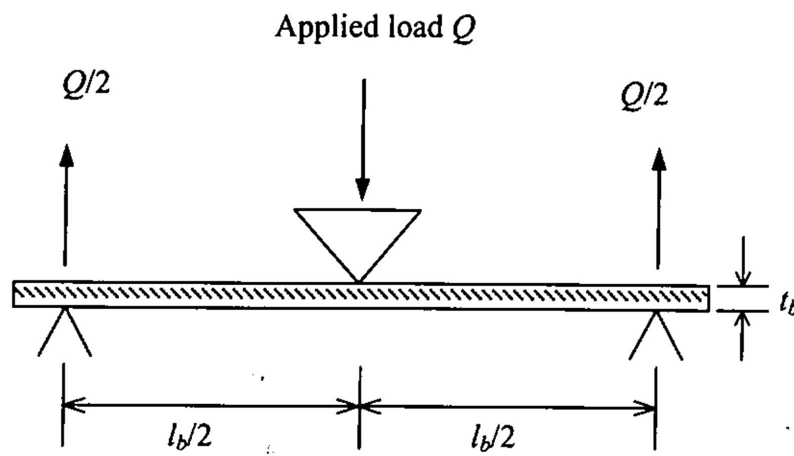

Fig. A.6 Simply supported ends boundary conditions.

The displacement w of the center point of the bridge depends on the load per unit width Q (= load/b_w) is expressed by [Zhang *et al.* 2000]:

$$w(Q,N_r,E_m)=\frac{-Q\cdot\tanh\left[\sqrt{\frac{12N_x}{E_m t_b^3}}\cdot\frac{l_b}{2}\right]}{2N_x\sqrt{\frac{12N_x}{E_m t_b^3}}}+\frac{l_b Q}{4N_x} \quad (A.4.1)$$

where N_x satisfies the equation :

$$N_x^2 N_r = N_x^3 - E_m t_b\left[\frac{1}{4}\cdot\frac{\sinh^2\left(\sqrt{\frac{12N_x}{E_m t_b^3}}\cdot\frac{l_b}{2}\right)}{\sinh^2\left(\sqrt{\frac{12N_x}{E_m t_b^3}}\cdot l_b\right)}-\frac{3}{4l_b\sqrt{\frac{12N_x}{E_m t_b^3}}}\cdot\frac{\sinh^2\left(\sqrt{\frac{12N_x}{E_m t_b^3}}\cdot\frac{l_b}{2}\right)}{\sinh\left(\sqrt{\frac{12N_x}{E_m t_b^3}}\cdot l_b\right)}+\frac{1}{8}\right]Q^2 \quad (A.4.2)$$

N_x is the force per unit width at the central line of the cross section along the length of the microbridge and N_r is the residual force per unit width in the film along the length direction.

Fig. A.7 shows the comparison between the experimental data and theoretical fitting curve. The optimum values of E_m and N_r for getting minimum fitting error are 214 GPa and 100 MPa, respectively. The curve fits the experimental data quite well, illustrating the effectiveness of the method for evaluating the mechanical properties of thin films.

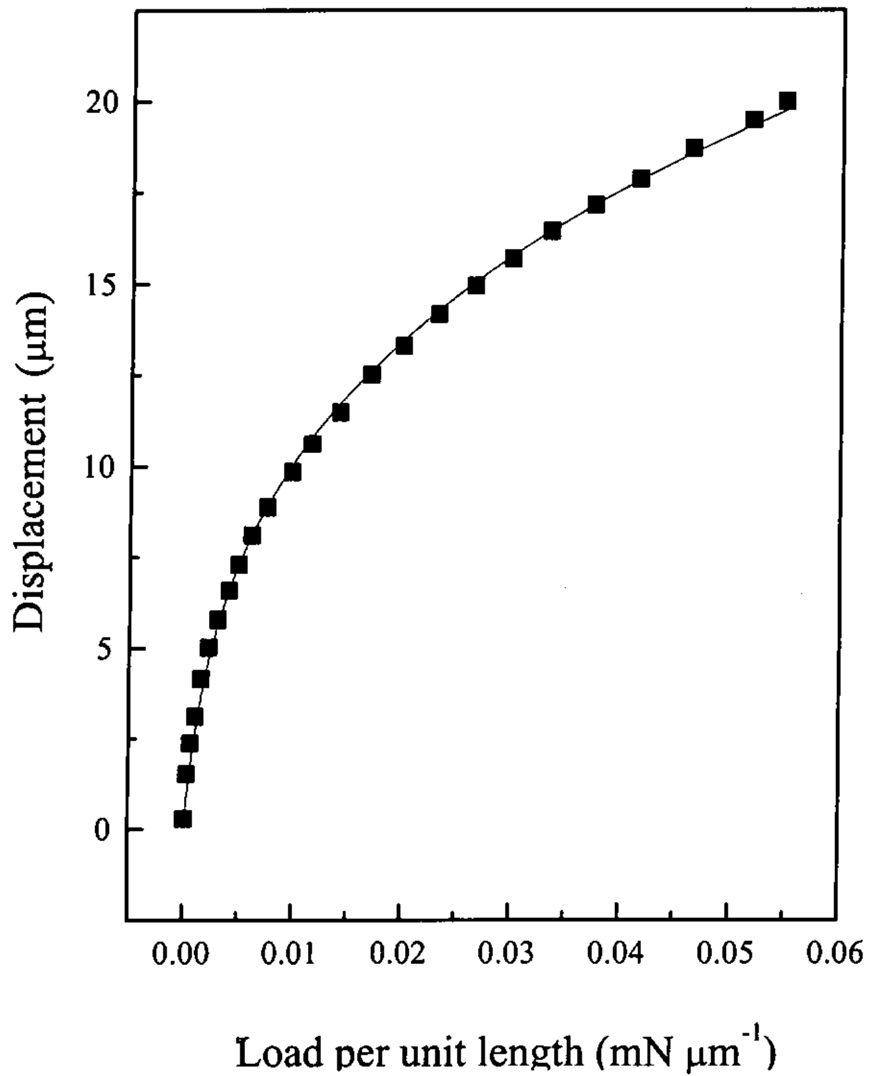

Fig. A.7 Comparison of experimental and theoretical load-displacement curves of microbridge. Square points: experimental data, solid line: theoretical solution.

The optimum elastic modulus and residual stress ($\sigma_r = N_r/t_b$) were obtained determined by minimizing the deviation of experimental data and theoretical data:

$$Error = \sum_{i=1}^{n}\left[w_i^e(Q_i) - w_i^t(Q_i, N_r, E_m)\right]^2 \tag{A.4.3}$$

where n is the number of data, w_i^e is the experimental displacement, and $w_i^t(Q_i, N_r, E_m)$ is the theoretical displacement obtained by equations (A.3.1) and (A.3.2).

When the elastic modulus and residual stress of a film are extracted, the stresses in the film under given loads can be determined. The total stress in the microbridge beam is contributed by two components, one due to the middle plane tension and the other due to bending. Thus, the bending strength σ_{bs} of the film is given by:

$$\sigma_{bs} = \frac{N_x}{t_b} + \frac{E_m t_b Q}{2N_x} \cdot \sqrt{\frac{12N_x}{E_m t_b^3}} \cdot \frac{\sinh^2\left(\sqrt{\frac{12N_x}{E_m t_b^3}} \cdot \frac{l_b}{2}\right)}{\sinh\left(\sqrt{\frac{12N_x}{E_m t_b^3}} \cdot l_b\right)} \tag{A.4.4}$$

the first term on the right-hand side is the tensile stress in the middle plane of the bridge and the second term is the tensile stress due to bending.

Fig. A.8 shows the experimental and theoretical curves of sample S2. The analytic solution gives a good fit to the experimental curve. The determined elastic modulus and residual stress of the LPCVD silicon nitride film are 267 GPa and 200 MPa, respectively. In turn, the calculated bending strength is 4.44 GPa.

There are different techniques to find out the elastic modulus and residual stress of a LPCVD silicon nitride thin film. For comparison, Vlassak and Nix [Vlassak and Nix 1992] developed a bugle test technique, by changing the membrane aspect ratio, the test yielded a mean elastic modulus of 222 GPa and residual stress in between of 120 – 150 MPa. Also using bulge testing on rectangular membranes, Tabata *et al.* [Tabata *et al.* 1989] reported the elastic modulus and residual stress of LPCVD silicon nitride films to be 290 GPa and 1.0 GPa.

Among the techniques described above, the value of elastic modulus varies in the range of 200 to 290 GPa and the value of residual stress varies in a relative large range region from 120 MPa to 1.0 GPa. Reported by Taylor [Taylor 1991] the elastic modulus is varied by the film density. Levy *et al.* [Levy *et al.* 1996] also suggested the variation was caused by the gradual densification that occurred at higher deposition temperatures. The residual stress in silicon nitride films depends very much on the fabrication process.

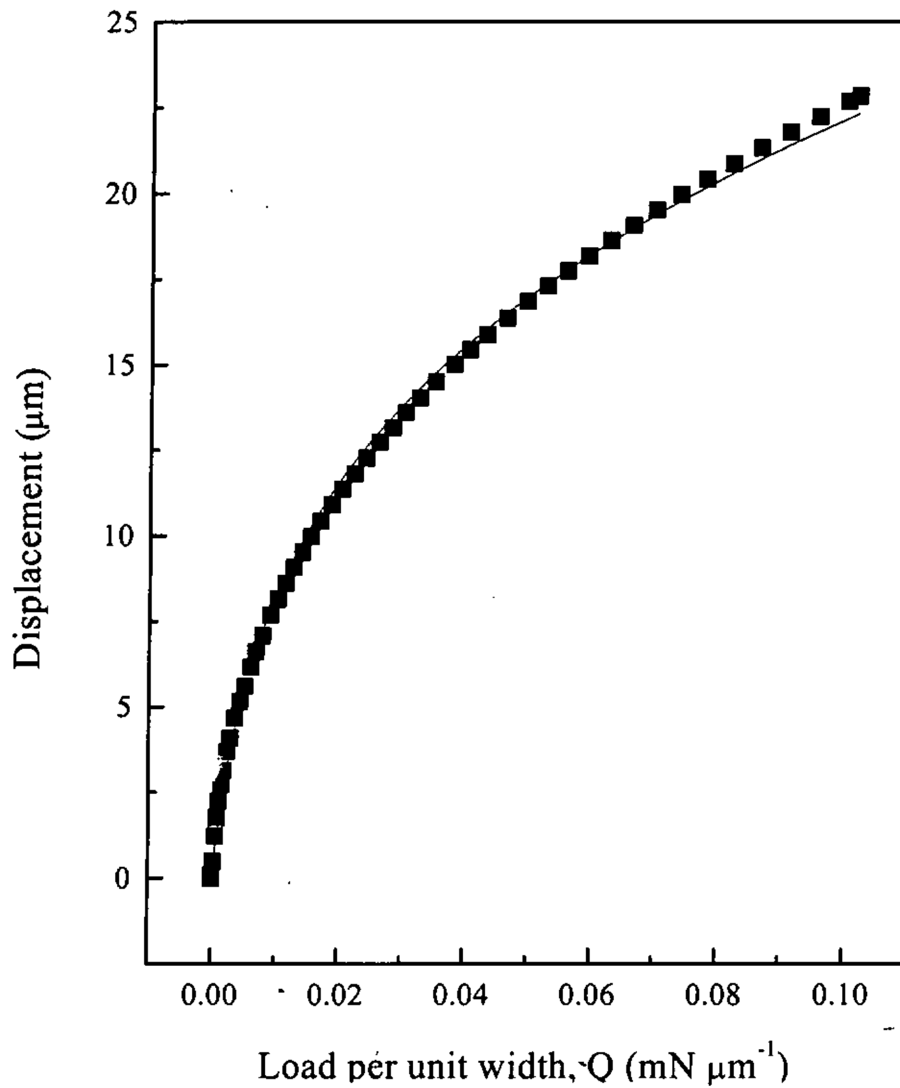

Fig. A.8 Theoretical analysis of load-displacement curve of sample S2.
Square points: experimental data, solid line: theoretical solution.

References

Adams[1], A. C. "VLSI Technology", Sze, S.M., ed., McGraw-Hill, Singapore, pp.120 (1985).

Adams[2], A. C. "VLSI Technology", Sze, S.M., ed., McGraw-Hill, Singapore, pp.121 (1985).

Alpert, N. L., Keiser, W.E. and Szymanski, H.A. "Introduction to Infrared Spectroscopy", In IR: Theory and practice of infrared spectroscopy, Plemum Press, N.Y., pp.1-8 (1970).

Arnoldbik, W.M., Maree, C.H.M., Maas, A.J., Boogaard, M. J. van der, Habraken, F.H. and Kuiper, A.E. "Dynamic behavior of hydrogen in silicon nitride and oxynitride films made by low pressure chemical vapor deposition". Phys. Rev. B, 48 (8), pp.5444 (1993).

Balland, B., Bureau, J.C., Plossu, C. and Botton, R., Mater. Res. Soc. Symp. Proc., 284, pp.39 (1993).

Blaauw, C. "Preparation and characterization of plasma-deposited silicon nitride". J. Electrochem. Soc., 131 (5), pp.1114 (1984).

Blaauw, C. "Stress in chemical-vapor-deposited SiO_2 and plasma-SiN_x films on GaAs and Si". J. Appl. Phys., 54 (9), pp.5064 (1983).

Cho, S. J., Lee, K. R., Eun, K. Y., Han, J. H., Han, D. H. and Ko, D. H., Mat. Res. Soc. Symp. Proc., 505, pp.33 (1998).

Claassen, W. A. P., Valkenburg, W. G. J. N., Habraken, F. H. P. M. and Tamminga, Y., J. "Characterization of plasma silicon nitride layers". Electrochem. Soc., 130 (12), pp.2419 (1983).

Collins, G. and Rej, D. J., MRS Bulletin, 21, pp.26 (1996).

Cullity, B.D. "The structure of Polycrystalline Aggregates", In Elements of X-ray Diffraction, Addison-Wesley Publishing, Co., Inc., USA, pp.259 (1965).

Curtins, H. and Favre, M. in Amorphous Silicon and Related Materials, Fritzsche H., ed., World Scientific Publishing Company, Singapore, pp.329 (1988).

Curtins, H., Favre, M., Amorphous Silicon and Related Materials, Fritzsche, H., ed.,World Scientific Publishing Company, Singapore, pp.329 (1988).

Elshabini-Riad, A. and Barlow, F.D., "Thin Film Technology Handbook", McGraw-Hill, New York, pp.3 (1997).

Erler, H. J., Reisse, G. and Weissmantel C. "Nitride film deposition by reactive ion beam sputtering". Thin Solid Films, 65, pp.233 (1980).

Feltz, A. "Electrical Conductivity and Optical Properties of Glasses and Amorphous Solids". In Amorphous inorganic materials and glasses, VCH, New York, pp.379 (1993).

Flinn, P. A., Gardner, D. S. and Nix, W. D. "Measurements and interpretation of stress in aluminium-based metallization as a function of thermal history", IEEE Trans. Electron Devices, ED-34 (3), pp.689 (1987).

Fourrier, A., Bosseboeuf, A., Bouchier, D. and Gautherin, G. "Annealing effect on mechanical stress in reactive ion-beam sputter-deposited silicon nitride films". Jpn. J. Appl. Phys., 30, pp.1469 (1991).

Fujita, S., Zhou, N. and Sasaki, A. "Composition and chemical bonds in silicon nitride by SiH/sub 4/-N/sub 2/ gas mixture plasma CVD". Jpn. J. Appl. Phys., 22(2), pp.L100 (1983).

Gupta, M., Rathi, V.K., Singh, S.P., Agnihotri, O.P. and Chari, K.S. "Plasma enhanced chemical vapour deposition silicon nitride for microelectronic applications". Thin Solid Films, 164, pp.309 (1988).

Gupta, M., Rathi, V.K., Thangaraj, R., Agnihotri, O.P. and Chari K.S. "The preparation properties and applications of silicon nitride thin films deposited by plasma-enhanced chemical vapour deposition". Thin Solid Films 204, pp.77 (1991).

Hattangady , S. V., Fountain, G.G., Rubber, R.A. and Markunas, R.J. "Low hydrogen content silicon nitride deposited at low temperature by novel remote plasma technique". J. Vac. Sci. Technol. A, 7 (3), pp.570 (1989).

Hu, S. M., J. Electrochem. Soc., 113 (7), pp.693 (1966).

Huang, L., Hipps, K.W., Dickinson, J.T., Mazur, U. and Wang, X.D. "Structure and composition studies for silicon nitride thin films deposited by single ion beam sputter deposition". Thin Solid Films, 299, pp.104 (1997).

Jackson, W.B. and Amer, N. M. "Direct measurement of gap-state absorption in hydrogenated amorphous silicon by photothermal deflection spectroscopy". Phys. Rev. B, 25, pp.5559 (1982).

Jansen, F., Day, A. and Wamboldt, L.. "On the chemical and mechanical properties of sputtered silicon nitride films". Thin Solid Films, 219, pp.139 (1992).

JCPDS, X-ray powder diffraction files (Joint Committee for Powder Diffraction Standards, Swarthmore, PA, 1975), card number 33-1160.

JCPDS, X-ray powder diffraction files (Joint Committee for Powder Diffraction Standards, Swarthmore, PA, 1975), card number 41-360.

JCPDS, X-ray powder diffraction files (Joint Committee for Powder Diffraction Standards, Swarthmore, PA, 1975), card number 40-1129.

JCPDS, X-ray powder diffraction files (Joint Committee for Powder Diffraction Standards, Swarthmore, PA, 1975), card number 27-1402.

Kanicki, J., Mater. Res. Soc. Symp. Proc., 118, pp.671 (1998).

Kim, J. H. and Chung, K.W. "Microstructure and properties of silicon nitride thin films deposited by reactive bias magnetron sputtering". J. Appl. Phys., 83, pp.5831 (1998).

Köhler, J. M. "Etching in Microsystem Technology",Wiley-VCH, Weinheim, pp.298 (1999).

Kuwano, Y. "Some properties of silicon nitride films produced by radio frequency glow discharge reaction of silane and nitrogen" Jpn. J. Appl. Phys., 8(7), pp.876 (1969).

Levy, R. A., Lin, X. and Grow, J. M., Boeglin, H. J. and Shalvoy, R. "Low pressure chemical vapour deposition of silicon nitride using the environmental friendly tris(dimethylamino) silane precursor". J. Mater. Res., 11, pp.1483 (1996).

Liao, W. S., Lin, C. H. and Lee, S. C. "Oxidation of silicon nitride prepared by plasma-enhanced chemical vapour deposition at low temperature". Appl. Phys. Lett., 65, pp.2229 (1994).

Monk, P.M.S., Mortimer, R.J., Rosseinsky, D.R. "Electrochromism: Fundamentals and Applications". VCH, Weinheim, pp.59 (1995).

Mott. N.F. and Davis, E.A., in Electronic Processes in Non-Crystalline Materials, Clarendon Press, Oxford, pp.249 (1971).

Mott. N.F. and Davis, E.A., in Electronic Processes in Non-Crystalline Materials, Clarendon Press, Oxford, pp.24 (1971).

Nagels, P., in Amorphous Semiconductors, Brodsky M.H., ed., Springer-Verlag, Berlin, pp.125 (1979).

Olefjord, I. "Surface characterization: a user's sourcebook". Brune, D., Hellborg, R., Whitlow, H. J. and Hunderi O., eds., Wiley-VCH, Germany, pp.316 (1997).

Oliver, W. C. and Pharr, G. M. "An improved technique for determining hardness an elastic modulus using load and displacement sensing indentation experiments". J. Mater. Res., 7, pp.1564 (1992).

Ong, C. W., Chan, K.F. and Choy, C.L. "Optical absorption and transport mechanisms of dual ion beam deposited boron-rich boron nitride films". Thin Solid Films, 388, pp.217 (2001).

Parsons, G.N., Souk, J.H. and Batey, J. "Low hydrogen content stoichiometric silicon nitride films deposited by plasma-enhanced Chemical Vapour Deposition". J. Appl. Phys., 70, pp.1553.(1991).

Payson, J.S. and Guha, G. "Determination of the gap-state distribution of hydrogenated amorphous silicon alloys from sub-band gap absorption measurements". Phys. Rev. B, 32, pp.1326 (1985).

Pierson, H.O. "Handbook of Refractory Carbides and Nitrides", Noyes Publications, Westwood N.J., pp.219 (1996).

Rathi, V. K., Gupta, M., Singh, S. P., Chari, K. S. and Agnihotri, O. P., Proc. Int. Symp. on Electron Devices, Circuits and Systems, pp.303 December (1987).

Ray, S.K., Das, S., Maiti, C.K., Lahiri, S.K. and Chakraborti, N.B. "Effect of reactive-ion bombardment on the properties of silicon nitride and oxynitride films deposited by ion-beam sputtering". J. Appl. Phys., 75, pp.8145 (1994).

Ron, Y., Ravch, V.K., Carmi, U., Inspektor, A. and Avni, R. "Deposition of silicon nitride from $SiCl_4$ and NH_3 in a low pressure RF plasma". Thin Solid Films, 107, pp.181 (1983).

Savall, C. and Bruyere, J.C. "Hydrogen and denterium migration in annealed plasma-deposited silicon nitride films". Thin Solid Films 258, pp.1 (1995).

Shirley, D.A. "High-resolution x-ray photoemission spectrum of the valence bands of gold". Phys. Rev. B, 5, pp.4709 (1972).

Sinha[1], A. K., Levinstein, H. J., Smith, T. E., Quintana, G. and Haszko, S. E. "Reactive plasma deposited Si-N films for MOS-LS1 passivation". J. Electrochem. Soc., 125, pp.601 (1978).

Sinha[2], A. K., Levinstein, H. J. and Smith, T. E. "Thermal stresses and cracking resistance of dielectric films (SiN, Si_3N_4 and SiO_2) on Si substrates". J. Appl. Phys., 49, pp.2423 (1978).

Steiner, P. and Lang, W. "Micromachining applications of porous silicon". Thin Solid Films, 255, pp.52 (1995).

Stelmack, L. A., Thurman, C. T. and Thompson, G. R., Nucl. Instr. and Meth., B37/38, pp.787 (1989).

Stoney, G. G. "The tension of metallic films deposited by electrolysis". Proc. R. Soc. London, Ser. A, 8, pp.172 (1909).

Sun, S. S. "Internal stress on ion beam sputtered molybdenum films". J. Vac. Sci. Technol., A 4, pp.572 (1986).

Sze, S. M. "VLSI Technology". Sze, S.M. ed., 2nd edition, McGraw-Hill Book Co., Singapore, pp.184 (1988).

Sze, S.M. " VLSI Technology". Sze, S.M., ed., McGraw-Hill Book Co., Singapore, pp.121 (1983).

Tabata, O., Kawahata, K., Sugiyama, S. and Igarashi, I. "Mechanical property measurement of thin films using load-deflection of composite rectangular membranes". Sensors and Actuators, 20, pp.135 (1989).

Tauc, J. "Optical Properties of Non-crystalline Solid". Abeles F. ed., in Optical properties of solids, North-Holland, London, pp.277 (1972).

Tayor, J.A. "The mechanical properties and microstructure of plasma enhanced chemical vapor deposited silicon nitride thin films". J. Vac. Sci. Technology. A, 9, pp.2464 (1991).

Teter, D. M. "Computational alchemy: the search for new superhard materials". Mat. Res. Soc. Bull., 23, pp.22 (1998).

Tsukamoto, Y., Yamaguchi, H. and Yanagisawa, M. "Mechanical properties of thin film: measurements of ultramicroindentation hardness, young's modulus and internal stresses". Thin Solid Films, 154, pp.171 (1987).

Urbach, F. "The Long-Wavelength Edge of Photographic Sensitivity and of the Electronic Absorption of Solids". Phys. Rev., 92, pp.1324 (1953).

Van de Ven, E. "Plasma deposition of silicon dioxide and silicon nitride films". Solid State Technol., April, pp.167 (1981).

Vanecek, M., Abraham, A., Stika, O., Stuchlik, J. and Kocka J. "Gap states density in a-Si:H deduced from subgap optical absorption measurement on Schottky solar cells", Phys. Stat. Sol. A, 83, pp.617 (1984).

Vlassak, J. J. and Nix, W.D. "A new bulge test technique for the determination of young's modulus and Poisson's ratio of thin films". J. Mater. Res., 7, pp.3242 (1992).

Weissmantel, C. "Reactive film preparation". Thin Solid Films, 32, pp.11 (1976).

Windischmann, H. "An intrinsic stress scaling law for polycrystalline thin films prepared by ion beam sputtering", J. Appl. Phys., 62, 1800 (1987).

Wittberg, T. N., Hoenigman, J. R., Moddeman, W. E., Cothern, C. R. and Gulett, M. R. "AES and XPS of silicon nitride films of varying refractive indices". J. Vac. Sci. Technol., 15, pp.348 (1978).

Witvrouw, A and Spaepen, F. "Determination of elastic constants and viscosity of amorphous thin films from substrate curvature". Mat. Res. Soc. Symp. Proc., 188, pp.147 (1990).

Yoon, J. S., Deshpandey, C. V. and Bunshah, R. F. "Effect of substrate bias on properties of silicon nitride films prepared by activated reactive evaporation". Thin Solid Films, 220, pp.80 (1992).

Zhang, T.-Y., Su, Y.-J., Qian, C.-F., Zhao, M.-H. and Chen, L.-Q. "Microbridge testing of silicon nitride thin films deposited on silicon wafers". Acta Mater., 48, pp.2843 (2000).

Zhang, X., Zhang, T. -Y. and Zohar, Y. "Measurements of residual stresses in thin films using micro-rotating-structures". Thin Solid Films 335, pp.97 (1998).

List of publications

Journal Papers

[1] M. P. Tsang, C. W. Ong, N. Chong and C. L. Choy, "Mechanical and etching properties of dual ion beam deposited hydrogen-free silicon nitride films". *Journal of Vacuum Science and Technology A*, Vol. 9, No. 5, pp.2542 – 2543 (2001).

[2] M. P. Tsang, C. W. Ong and C. L. Choy, "Correlation between the composition, structure and properties of dual ion beam deposited SiN_x films". *Thin Solid Films,* (to be submitted)

[3] C. W. Ong and M. P. Tsang, "A semi-empirical unified interpretation of optical absorption and electrical conductivity of amorphous solids having high density of mid-gap states". *Journal of Applied Physics*, (to be submitted)